This is to certify that the
dissertation entitled

STUDIES OF CRACK PROPAGATION AND MICROCRACK INITIATION IN A NEAR-GAMMA TIAL ALLOY

presented by

BOON-CHAI NG

has been accepted towards fulfillment
of the requirements for the

Ph.D. degree in Materials Science

Thomas R Bieler
Major Professor's Signature

5th May 2005
Date

STUDIES OF CRACK PROPAGATION AND MICROCRACK INITIATION IN A NEAR-GAMMA TIAL ALLOY

By

Boon-Chai Ng

A DISSERTATION

Submitted to
Michigan State University
in partial fulfillment for the requirements
for the degree of

DOCTOR OF PHILOSOPHY

Department of Chemical Engineering and Materials Science

2005

ABSTRACT

STUDIES OF CRACK PROPAGATION AND MICROCRACK INITIATION
IN A NEAR-GAMMA TIAL ALLOY

By

Boon-Chai Ng

Fracture in a duplex γ -TiAl alloy with equiaxed grains has been studied. The crack path in a notched Mode I crack growth specimen was analyzed using a combination of orientation imaging microscopy and selected angle channeling patterns as well as electron channeling contrast imaging techniques.

A fracture propagation parameter, incorporating the contributions from deformation twinning and ordinary dislocation systems, has been developed. This parameter, $F_{A\rightarrow B}$, is capable of identifying boundaries that are likely to nucleate microcracks. It was observed that microcracking is less likely when $F_{A\rightarrow B} < 1.0$ but is more likely when $F_{A\rightarrow B} > 1.0$.

The primary crack has a tendency to propagate towards clusters of weak boundaries (identified by the fracture propagation parameter). Where it is not possible to follow a boundary directly, the crack will cleave through a grain, via the shortest distance, towards the next cluster of weak boundaries.

TO GOD
BE THE GLORY

ACKNOWLEDGEMENTS

This dissertation would never have been made possible if not for the many individuals who were there to help and guide me in one way or another. Among the many individuals, I would like to single out a few to express my sincere thanks.

I would like to thank members of my Ph.D. committee, Drs. Thomas Bieler, Martin Crimp, David Grummon and Dr. Duncan Sibley for their time, guidance and their patience. Special mention goes to both my co-advisors Drs Martin Crimp and Thomas Bieler. My skill as an electron microscopist is credited to Dr. Crimp. His dedication, easy going and helpful suggestions on microscopy techniques have made me a better microscopist. Dr. Bieler was instrumental in helping me obtain the texture analysis for the material and had contributed many valuable suggestions during the drafting of this dissertation. The painstaking review of this dissertation was undoubtedly credited to Dr. Bieler.

I would also like to thank Dr. Darren Mason for providing the computational programs needed to speed up the grain orientation analysis. Drs. Jimmy Kijai and Sammy Chuah, both from Andrews University, for their helpful discussion on the use of statistical tools for analysis and Dr. Benjamin Simkin, who has been a good friend and help in developing the technique of electron channeling contrast imaging as well as lengthy discussion on the TiAl alloys.

The financial supported by the Air Force Office of Scientific Research under grant # AFRL no. F49620-01-1-0116, monitored by Dr. Craig Hartley is gratefully acknowledged.

Last but not least, I would like to thank my wife, Belle, and daughter, Dominique for their help, support and patience throughout this long journey to complete this dissertation.

TABLES OF CONTENTS

LIST OF TABLES

LIST OF FIGURES

Images in this thesis/dissertation are presented in color

Chapter 1: Introduction

1.1 General Overview

There continues to be a growing demand for lightweight, high strength, and good corrosion-resistant materials to be used in aerospace and automotive applications. Gamma titanium aluminides are emerging as potential engineering materials for these (aerospace and automotive) industries because of their low densities, high melting temperatures, good elevated-temperature strengths and modulus retention, high resistance to oxidation and hydrogen absorption, and excellent creep properties [1-5]. These alloys have been aggressively pursued as an airfoil material, for the compressor and the low-pressure turbine sections of gas turbine engines [6].

The gamma alloys developed so far consist of titanium, 46-52 at. % aluminum and 1-10% at. % M, with M being at least one element from V, Cr, Mn, W, Mo, Nb and Ta. [4]. These gamma TiAl alloys can be divided into either single-phase (gamma) alloys or two phase (γ and $\alpha 2$) alloys [4]. The two-phase alloys with very small amounts of Ti_3Al have been found to exhibit higher yield and ultimate tensile strengths than single-phase TiAl [7]. They were also more ductile and tougher than single phase TiAl [8]. However, these gamma alloys have yet to achieve their full potential as an engineering material due to their low ductility and toughness at ambient temperatures, which, along with poor formability, continue to plague their utilization [4]. Design engineers detest such properties (low ductility and toughness) because of the perceived risk of catastrophic failure [6].

The low toughness of these gamma alloys has been the primary focus in this work. The toughness of a material is related to its ability to resist or arrest cracks.

Understanding why and how cracks propagate and arrest in these gamma alloys will provide an important basis for the improvement of toughness in these alloys. A study of the micro-structural conditions that enhance or suppress the initiation of microcracks in the vicinity of the crack tips and along crack edges would thus provide valuable information for improving the toughness of these alloys.

In order to characterize the micro-mechanisms associated with microcrack initiation or enhanced deformation transfer, this study will focus on the propagation and subsequent arrest of cracks in an equiaxed near-gamma TiAl alloy. Four-point bend specimens were loaded *in-situ* in the scanning electron microscope (SEM) until a crack propagated from a notch. Although the nature of the crack path and deformation defect structures near crack tips have traditionally been examined via Transmission Electron Microscopy (TEM) using thin foils made from the sample specimen, this study uses electron channeling contrast imaging (ECCI) to observe these deformation defect structures. This ECCI technique allows imaging of near surface dislocations and twins in bulk specimens [9-13].

In many microscale or mesosacle deformation studies, it is important to know the grain orientation. Active slip systems, grain boundary characteristics and elastic moduli depend on grain orientation. The electron backscattered diffraction (EBSD) technique, performed using a scanning electron microscope, is commonly employed to determine the grain orientation in bulk specimens. Alam and co-workers first developed this technique in 1954 [14], calling them "high-angle Kikuchi patterns", in recognition of related diffraction phenomena reported by Kikuchi [15] in the 1920s. This technique, although easy and quick, is not capable of distinguishing the ***c*** and ***a*** direction in

tetragonal structures with c/a ratio that differs from 1 by 5%. In such a tetragonal structure, the EBSD analysis would result in three possible grain orientations. On the other hand, selected area channeling patterns (SACP), a technique also performed using a scanning electron microscope, can detect the superlattice bands from an ordered tetragonal structure and provide the correct grain orientation. This superlattice information is rarely resolved with the EBSD technique. But the process of collecting SACPs over various tilt positions, identifying the bands and zones in order to correctly locate the grain normal, is very tedious and time consuming.

A new approach, incorporating the ease and quickness of EBSD analysis with the unique capability of the SACP to differentiate the c and a direction had been used to speed up the process of determining the grain orientation of tetragonal structures by a factor of 10.

With correct grain orientations and the ability to observe microcracks at twin-grain boundary intersections, it was possible to develop a fracture propagation parameter that is able to identify how efficient slip can be transferred across the boundary. This parameter incorporates the Schmid factor, the interaction of the leading twin vector with the tensile direction, the ordinary dislocations, and the twinning vectors from the adjacent grains.

The principle focus of this dissertation has been on a primary active crack as it propagates through the γ–γ grain boundaries. This work has been built on the initial work done by Ben Simkin [16] who developed a fracture initial parameter using a limited number of data. By incorporating the analysis of more than 39 boundaries in grains surrounding the primary fracture crack in the crack growth specimen complimentary

fracture propagation parameter has been developed. This fracture propagation parameter only needs the primary tensile stress axis and spatially resolved grain orientations to predict the path of the crack. The use of this parameter will provide the information much needed by the design engineer as to where the crack would/might advance so that designs can be modified to strengthen the product and to arrest any propagating crack.

Chapter 2: Literature Review

2.1. Overview

TiAl, an ordered intermetallic compound, has been viewed as a potential candidate for high temperature structural material. This chapter reviews some of the recent important developments of TiAl in the area of physical and mechanical properties of TiAl. The microscopy techniques used by Simkin [16] on a similar research effort are also reviewed at the end of this section.

2.2. Microstructures And Phase Relationships

A portion of the binary phase diagram [7] of the Ti-Al system is shown in figure 2.1. Depending on the composition, when the TiAl alloy is cooled from the melt, the following reactions take place:

1. Liquid (L)→ (L + alpha (α)) → α phase.

2. Gamma (γ) precipitates on basal planes within the (α + γ) phase field.

3. As the material cools further, the α phase orders to α2 ($D0_{19}$ structure).

At room temperature in the as-cast condition (processes such as casting, ingot metallurgy or powder metallurgy), the two-phase (TiAl + Ti_3Al) TiAl alloys exhibit a lamellar microstructure [7,17]. The γ lamellae are formed in such a way that their closed packed planes and directions are:

{111}TiAl // (0001) Ti_3Al

<110> TiAl // <11-20> Ti_3Al [6]

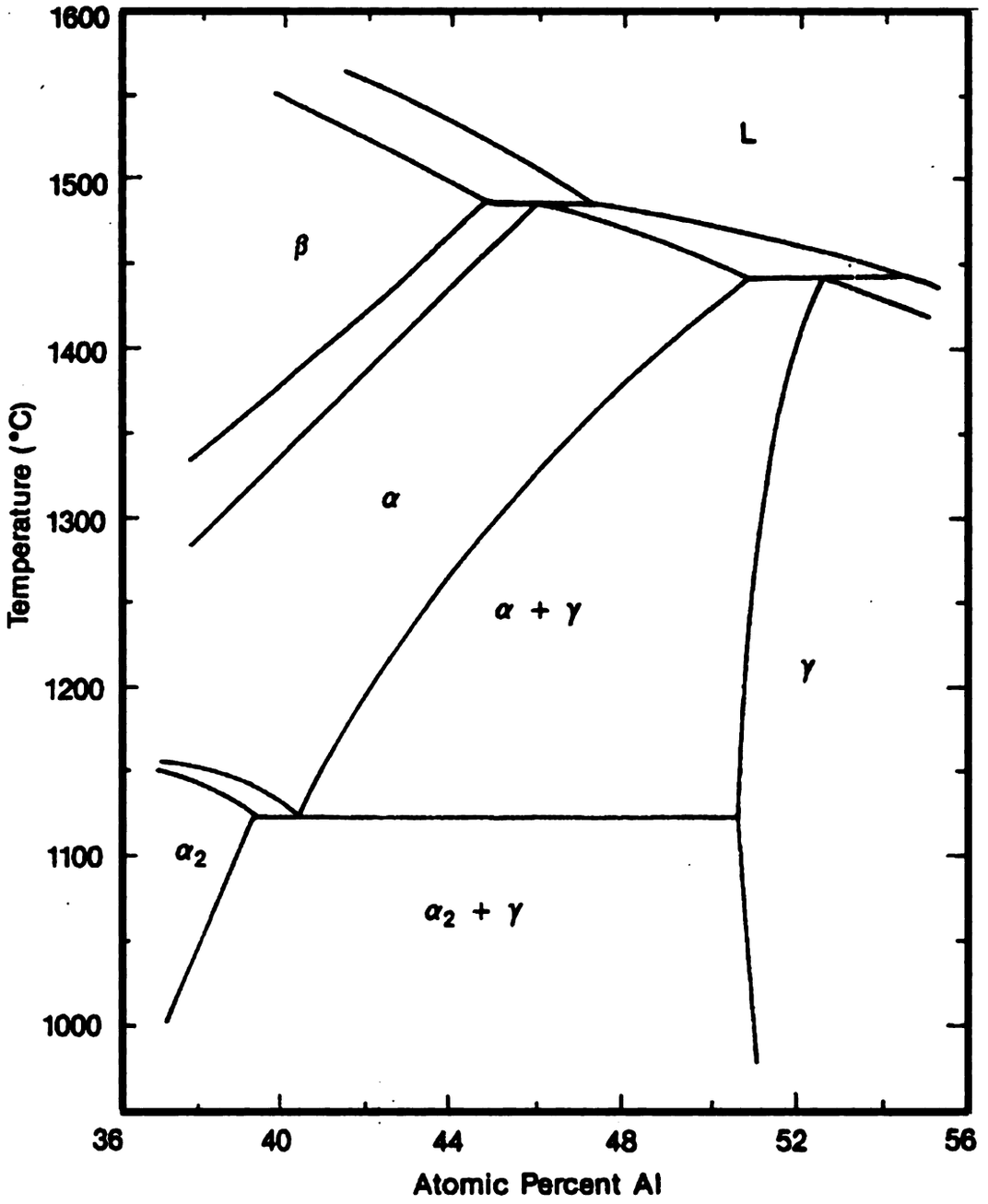

Figure 2.1. Phase diagram of a binary TiAl Alloy [8]

While the three <11-20> directions on the (0001) basal plane are all equivalent in the α2 phase (Ti_3Al), the [110] direction is not equivalent to the two other <011] directions on the (111) plane of the γ phase (TiAl). Consequently, the γ–phase can display in six possible orientation relationships corresponding to the six possible

orientations of [110] on (111) on an (0001) plane in the $\alpha 2$ phase, consistent with the ordering relationships given above [7,18,19].

Although these lamellar structures may be beneficial for toughness and high-temperature strength, they cause relatively poor room-temperature ductility [1,7,20]. Therefore, these alloys are usually further thermomechanically processed to achieve desirable microstructures. The most desirable microstructures are the near-γ microstructures, generally characterized by coarse γ grains and banded regions consisting of fine ($\gamma + \alpha 2$) grains [7]. Near-γ TiAl is obtained (after themomechanical processing) by further annealing heat treatment at temperatures just above the eutectoid temperature [7,20].

Near-γ TiAl alloys, which are rich in titanium, are composed of two phases: γ phase (nearly stoichiometric TiAl) has the $L1_0$ face centered tetragonal (FCT) crystal structure, and the α_2 phase (Al-rich Ti_3Al) has the $D0_{19}$ crystal structure (ordered hexagonal) [21] as shown in figures 2.2 and 2.3 respectively. The face centered tetragonal structure (similar to a face centered cubic (FCC) structure) consists of alternating titanium and aluminum (002) planes stacked normal to the c-axis. At the stoichiometric composition, the c/a ratio is 1.02 [4,5] (a=0.400nm and c=0.407nm) and the tetragonality increases up to 1.03 as the aluminum concentration increases [4]. The $D0_{19}$ structure has a=0.5775nm and c=0.4655nm. The two structures have regular stackings of closed-packed planes. The (111) planes in the FCT and the (0002) basal planes in the $D0_{19}$ structure are the closest-packed in their crystal structure.

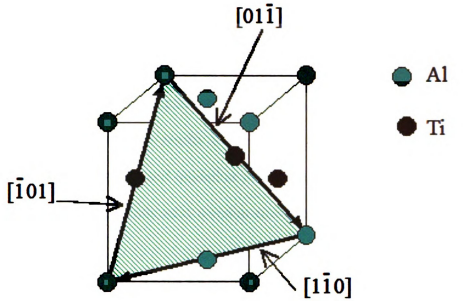

Figure 2.2. Unit cell of L10 ordered TiAl with slip directions of the (111) slip plane.

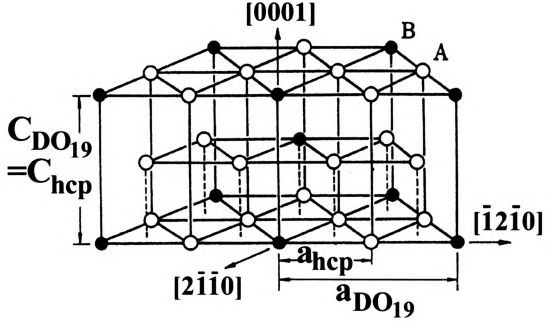

Figure 2.3. Unit cell of the DO_{19} structure [21].

2.3. Effects of Alloying Elements

The microstructure and mechanical properties of TiAl alloys are influenced by their chemical compositions. There are two groups of alloying elements. The first group of alloying elements provides precipitation strengthening or particle strengthening. These alloys include boron, which results in the refinement of microstructures, and silicon, which improves the creep and oxidation resistance [22]. The second group of alloying elements is associated with solid solution strengthening elements and includes Cr, Mn, V, Nb, and Fe. [22].

Alloying additions of Cr, V, and Mn were reported to enhance the plasticity of TiAl alloys [23,24]. It is believed that these additions enhance plasticity by stabilizing thermal twins, which provide nucleation sites for twinning dislocations [22,25]. Fe, Cr, V, and Nb had been reported to enhance the tensile strength at room temperature as well as the retention of creep rupture life of TiAl [22]. Nb also improves the oxidation resistance, elevated temperature strengths [22], and the yield strength of the alloy [26]. A review of these alloying consideration can be found in [8].

In this study, 2 at. %Nb and 2 at %. Cr were added to binary TiAl. The addition of Cr and Nb at this level does not change the essential two-phase character of the alloys [27]. The solubility of Nb in γ-TiAl is 6.86 at %. whereas only 3.07 at %. Cr can be dissolved in γ–TiAl. [22]. The alloying element Cr seems to be more likely to reside on the Al sites in the gamma-TiAl and whereas the preferential site of the Nb is the Ti sites [28-30].

2.4. Deformation Systems.

Deformation slip in ordered TiAl occurs exclusively on {111} planes [21] (Figure 2.2), either by dislocation slip or by twinning. However, unlike in FCC, the various slip directions are strongly affected by the ordering [31]. Four physically different modes have been distinguished, namely slip of ½ <110][1] ordinary dislocations, of <011] superdislocations, ½ <112] super-partial dislocations, and 1/6 <112] Shockley partial dislocations leading to ordered twins. Slip along <110] directions does not affect the ordering [31], so slip occurs by ordinary dislocations with 1/2 <110] Burgers vectors moving on {111} planes. In contrast, ½ <011] slip moves atoms to antisites positions (see Figure 2.2) and thus two consecutive slip steps are necessary to preserve the order. These dislocations exist as pairs and are called super-partial dislocations. Although these super-partial dislocations typically glide on the closed packed planes {111}, Morris [32] observed partial 1/2 [101] dislocations with edge character contained on (010) planes. Superdislocations with 1/2<112] Burger vectors have been rarely observed, as might be expected due to their larger Burgers vector [18,21].

Deformation twining is commonly observed in γ-TiAl [1,4]. Unlike dislocation motion, twin slip is polar, i.e. twins can only move in a single well-defined direction on a given slip plane. There are only four 1/6 <11-2] type twin directions, one per {111) plane that can be operated without destroying the order. Its slip vectors are of type 1/6<11-2][21]. Other 1/2 <112] dislocations would result in psuedotwins with ordering violations.

---

1. The mixed bracket <] is used to recognize the symmetry in the first two indices whereas the third index must be specified.

Ti_3Al deforms predominantly by the motion of 2/3<11-20> superlattice dislocations on the basal, prism and pyramidal planes [21].

2.5. Deformation at interfaces

25.1. γ–γ Interfaces

The orientation relationship between two neighboring γ lamellae can be described by 180°, 60 ° and 120° rotations of the [110] direction in the interface plane [18] and result in relationships called twin, pseudotwin and ordered-domain respectively [33]. The transfer mechanisms of the deformation at the interface (ordered domain and 180° rotation) have been studied by [33,34] respectively and are summarized below.

2.5.2. Ordered domain interface

The deformation transfer mechanisms at γ–γ ordered domain interfaces were observed to occur by two modes.

1. When deformation twins impinge on a grain boundary, 1/6<11-2] Shockley partial dislocations entering the interface will result in the emission of ½<110] ordinary and sometimes <101] superlattice dislocations across the interface. Because the superlattice dislocations have low mobility, it was speculated that these superlattice dislocations accumulated in the interface [33].
2. When ordinary dislocations impinge on a grain boundary, they dissociate to form Shockley dislocations and these dislocations are left in the interface [33].

2.5.3. Twin interface

For an 180° rotational twin interface, the crystal lattices on either side of the interface share a common <110] crystal orientation. As such, it is possible for <110] dislocations to be transferred through the interface without pinning and re-nucleation.

Pure screw dislocations had been observed to cross slip a twin-related interface since both their Burgers vector and line direction lie in the interface plane.

The incident shearing can also be largely transferred through the twin interface by the production twinning and ordinary dislocations. Non-screw dislocations will be locked at the interface and no emission of dislocations will be observed in the neighboring lamella.

2.5.4. Large angle γ–γ Grain Boundaries

Gibson and Forwood [35] demonstrated that, at a large-angle γ–γ grain boundary, the strain created by the deformation twin can be accommodated by the generation of glide in both grains by the movement of ½ (110]-type dislocations, with a residue Burger vector left at the common line of intersection. They did not observe any grain boundary accommodation via the emission of <101] dislocations in their experiments.

Zghal et.al [33,34], on the other hand, reported both ordinary and superdislocations were emitted in the second lamella when a twin crossed an ordered domain interface. But these superdislocations were only observed at the grain boundary interface due to their low mobility. Simkin [16] attributed these superdislocations near the interface to the residual strain accommodation mentioned by Gibson and Forwood.

2.6. Geometric Compatibility Factor

Luster and Morris [36] proposed a geometrical slip compatibility factor to describe the active deformation systems involved in strain transfer at a boundary in TiAl. This factor is defined as $\mathbf{m'}=\cos\theta*\cos\kappa$, where θ and κ are the angles between the slip plane normal and slip directions of a pair of deformation systems on either side of the grain boundary. For slip systems in adjacent grains, the m' may vary between 0 and 1. For m'=1, there is complete compatibility exist between the slip systems whereas for m'=0, the slip systems are completely incompatible. Positive values of m' denotes the most probable activation of the deformation system. Although this parameter is effective at describing activation of slip systems at or near boundaries, it does not correlate well with the nucleation of microcracks at the grain boundaries [37,38].

2.7. Parameter for the nucleation of grain boundary microcracks

Simkin [16] proposed a parameter that tried to relate γ–γ grain boundary microcrack nucleation to the global stress state and the individual grain orientation. By incorporating the observations of Gibson and Forwood, [35] into his work, Simkin's parameter $\boldsymbol{F}$ was:

$$\mathbf{F} = m_{\mathrm{tw}} \left| \hat{\mathbf{b}}_{\mathrm{tw}} \cdot \hat{\mathbf{t}} \right| \sum_{\mathrm{ord}} \left| \hat{\mathbf{b}}_{\mathrm{tw}} \cdot \hat{\mathbf{b}}_{\mathrm{ord}} \right|$$

where m_{tw} is the Schmid factor for a specific deformation twinning system under the global stress state and $\hat{\mathbf{b}}_i$ are unit vectors in the sample coordinate system that describe the Burgers' vector directions for the single twin system (*tw*) and all 8 of the ordinary dislocation systems in each grain (*ord*). **F** is determined for each of the 8 twin systems in

the pair of grains. The component $\left|\hat{\mathbf{b}}_{tw} \cdot \hat{\mathbf{t}}\right|$ relates the twin shear direction to the tensile direction, and the final summation measures the ability of the grain boundary to conform to the twin displacement by emission of a/2<110] ordinary dislocations into both bounding grains.

2.8. Microscopy techniques

Transmission electron microscopy, (TEM), is traditionally used to examine micro mechanisms of plastic deformation in materials. But specimen preparation and the possible artifacts associated with the thin foils preparation can limit this technique.

Electron channeling contrast imaging (ECCI), a scanning electron microscope (SEM) technique has recently been used to examine deformation structures in the bulk sample. This technique has been used to image near-surface crystal defects [for reviews, see ref. 9-13]. The ECCI technique is best understood by examining the source of the contrast, namely electron channeling, and electron channeling patterns. This description represents a combination of prior work of others and illustrative examples provided by the author.

2.9. Electron Channeling

When an energetic electron beam strikes a specimen, at a particular angle where these electrons will be parallel to the crystal lattice planes, they will penetrate deeper into the crystal, passing between the rows of atoms along "channels'. The chances of these electrons escaping from the specimen will decrease with increasing depth below the surface [39-40]. On the other hand, in crystals oriented slightly

differently, electrons will interact strongly with the surface and will escape from the specimen (figure 2.4).

2.10. Electron Channeling Patterns

In an SEM with a 2-Dimensional raster at low magnification, the normal action of the scanning results in an angular beam deflection of approximately 8 degrees from the microscope axis [40]. Consequently other lattice planes also contribute to the contrast and the resultant signal plot, the electron channeling pattern (ECP), shows bands of contrast from all sets of planes normal, or close to normal, to the surface [39-40]. The width of the band is twice the appropriate Bragg angle for the set of lattice planes and is inversely proportional to the lattice plane spacing (d) and the accelerating voltage. This ECP has the symmetry of the crystal lattice in the area examined. [39-40]. But this technique requires the whole scanned area have the same crystal orientation. So a single crystal is effectively analyzed with this technique.

When a polycrystalline material is imaged at low magnification, there are discontinuities in the electron channeling patterns because each individual grain will produce different signal level. The use of selected area channeling patterns (SACP) overcomes this problem.

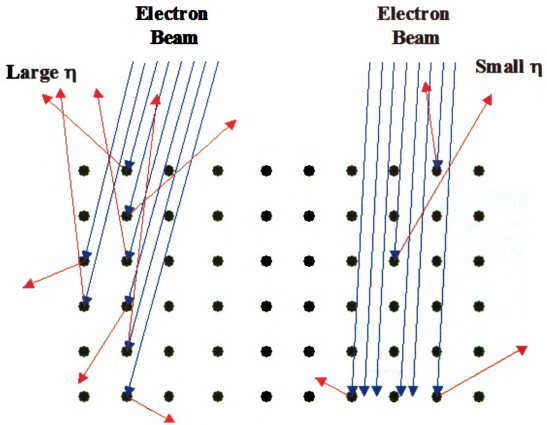

Figure 2.4. Electron channeling is an effect of the different interactions of the electrons with the crystalline material and depends on crystal orientation.

2.11. Selected Area Channeling Patterns (SACP)

In selected area channeling patterns, a channeling pattern from a small area is formed by rocking the electron beam about two perpendicular axes on the area of interest, with the resultant BSE signal as a function of tilt angles captured and displayed as shown in figure 2.5 [10]. This technique of rocking the electron beam can be accomplished by using a dedicated set of scan coils to rock the beam through the desired range of angles while it is confined to a very small area on the specimen. Because the set of scan coils mimic the action of a lens, it is important to readjust the focal point (cross-over) on the

are varied and finally dynamically corrected for the effects of spherical aberration. Joy et al. used images of copper grids to show the effect of strengthening the scan coils and correcting the spherical aberration effects [40].

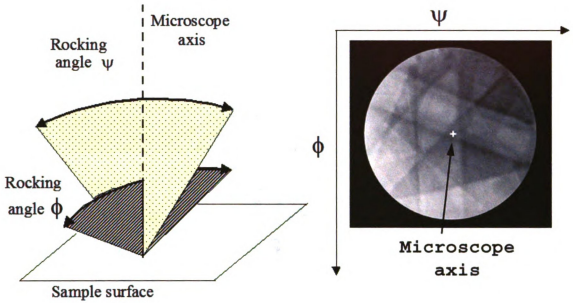

Figure 2.5. Formation of a selected area channeling pattern (SACP).

Selected area channeling patterns, like ECPs, also show bands of contrast from all planes normal to the surface [40] and are thus be able to reveal the crystal orientation of the grain in question. By tilting a specimen through many orientations relative to the beam (limited by the angle of tilt mechanism) a collection of SACPs can be assembled to form a SACP composite map as shown in figure 2.7. The determination of crystal orientation becomes one of pattern recognition, comparing angles between bands and angular bandwidths before confirming a solution. This technique is also capable of detecting 'superlattice' (incomplete destructive interference) information as shown in figure 2.7. However, the process of obtaining the SACPs through various tilts,

assembling into a SACP composite map, identifying major zones, measuring band widths and identifying bands to confirm a grain orientation, is tedious and laborious.

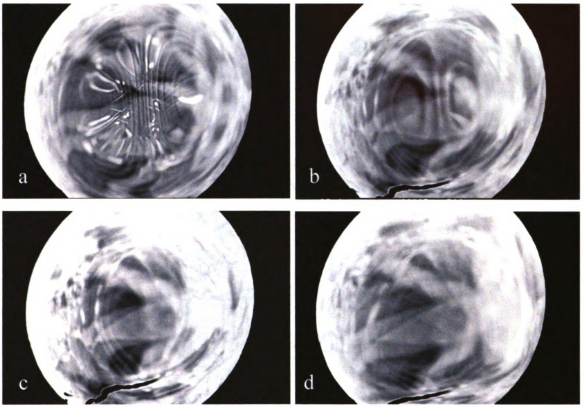

Figure 2.6. SACPs with variation in the focal point (crossover) of the scan relative to the specimen surface (a-c) and SACP image corrected dynamically (d).

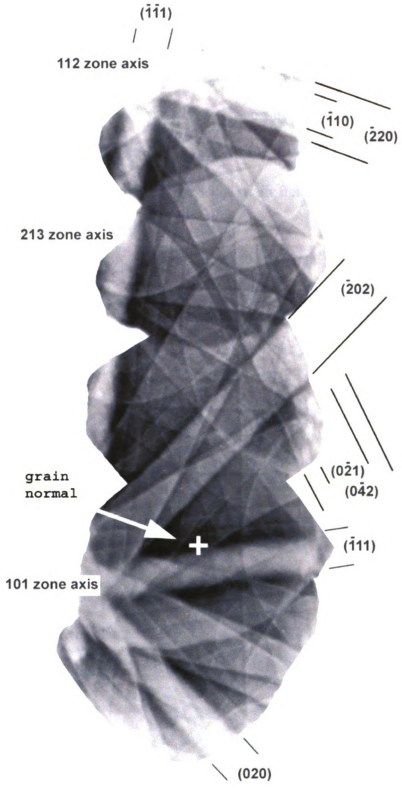

Figure 2.7. SACP composite reveals superlattice bands thereby making it easy to correctly identify the grain as having a grain normal: (2,17,-14).

2.12. Electron Channeling Contrast Imaging (ECCI)

In the ECCI technique, the electron channeling contrast is produced when some small near-surface volume of the crystal is on one side of some Bragg condition (e.g. $\theta > \theta_B$), while the bulk of the crystal is at or opposite side of the Bragg condition (e.g. $\theta < \theta_B$): the backscattered electron (BSE) yield tilted volume will be different from the rest of the crystal, thus highlighting the local strain field (for instance) of a dislocation (see Figure 2.8) [41-43].

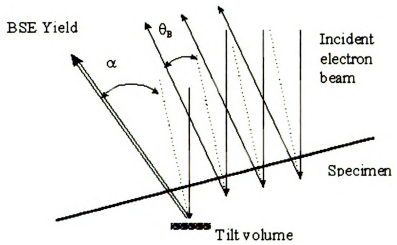

Figure 2.8. Near surface defects will cause a change in the BSE yield due to local lattice variations from the Bragg condition. θ_b is the Bragg angle and α is less or greater than the Bragg angle.

To image defects using ECCI, it is necessary to set up the channeling conditions, much like a selected area diffraction pattern (SAD) is used to set up a two beam diffracting condition for TEM imaging. An SACP (SAD mode) of the grain of interest is first obtained and tilted until one of the bands in aligned to the microscope axis as shown in figure 2.9. Switching back to the imaging mode, and refocusing at high magnification, any defects can subsequently be imaged-captured and integrated over multiple frames by the frame-store integral to the CamScan 44 FE SEM. Figure

2.10 shows an example of a secondary electron (SE) and ECCI images of a crack edge of a single crystal NiAl alloy [44]. Microcracks can be observed in the SE image but the ECCI image reveals dislocations lying parallel to the surface as well as end-on along the side of these microcracks. These dislocations are observed to be in bright/dark contrast. For end-on dislocations, with one end of each dislocation exiting the crystal and the other end into the crystal, the imaging contrast decreases as the dislocation penetrates deeper into the crystal. The reason for the near surface sensitivity is that the electrons from the incident beam loose coherency in penetrating the crystal, provide less contrast as they travel further into the crystal, and thus limiting the depth of detection [45-46]. Channeling contrast is highly dependent on the angular relationship between the beam and the crystal and as such, sharp changes in contrast may occur over angular changes less than 0.5 degrees [39]. This also means that any angular changes greater than 0.5 degrees will result in a loss of defect contrast in the crystal. Because 0.5 degrees is a very small angle, it is usual to iterate between tweaking the tilt control to align the band edge to the microscope axis in the SAD mode, and then try imaging the dislocations in the imaging mode.

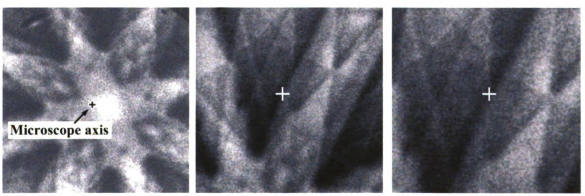

Figure 2.9. Alignment of a band to the microscope axis by tilting the specimen.

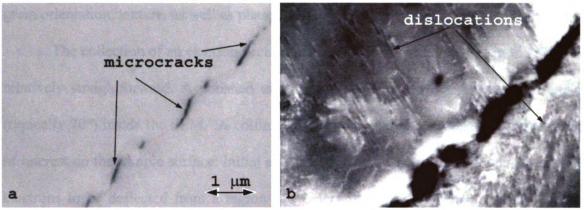

Figure 2.10. Example of dislocation imaging using ECCI technique. a) Secondary Electron image of microcracks. b) ECCI image reveals dislocations lying almost parallel to the surface as well as end-on. Sample is a single crystal NiAl alloy [44].

2.13. Electron backscattered Diffraction

The electron backscattered diffraction pattern, (EBSD), (also known as Backscattered Kikuchi Diffraction, BKD), was first developed by Alam and co-workers in 1954 [14], who called them "high-angle Kikuchi patterns ", in recognition of related diffraction phenomena reported by Kikuchi [15] in the 1920s while studying diffraction of electrons by thin films of mica. However, it was not until the 1970's that Venables and co-workers applied EBSD to metallurgical microcrystallography, [47] paving the way for a more widespread application of EBSD to the materials sciences. This technique was further developed by Dingley and co-workers [48] to measure crystal orientation in the SEM and subsequently refined for on-line pattern indexing with the aid of a computer [49].

In the past 10 years, rapid developments in both hardware and software have made EBSD an easy tool for the rapid analysis of microstructures in a range of crystalline

materials. It is a quantitative technique that reveals grain size, grain boundary character, grain orientation, texture, as well as phase identity [50].

The collection of an electron backscatter diffraction pattern (EBSP) in the SEM is relatively straightforward. A polished sample must be tilted to a relatively high angle (typically 70°) inside the SEM. A collimated electron beam is then directed at the point of interest on the sample surface: initial elastic scattering of the incident beam causes the electrons to be deflected from a region just below the sample surface and to impinge upon crystal planes in all directions. The atomic planes of the specimen are thus showered with electron arriving from all direction and with a wide range of wavelengths. For each set of planes in a crystalline specimen, there will always be some electrons that will satisfy the Bragg equation for diffraction.

$$\lambda = 2\, d \sin \theta$$

where λ is the dominant electron wavelength, d is the spacing between the planes and θ is the incidence angle of the electrons with the planes.

The backscattered electrons collide with a phosphor screen mounted in the SEM and create a diffraction pattern or "Kikuchi bands". These patterns consist of parallel lines, one pair of each set of atomic planes, separated by a bright band as shown in figure 2.11. Intersections of these bands correspond to zone axes or poles. [51].

The resulting electron backscattered diffraction pattern (EBSP) is captured via the phosphor screen interfaced to a low-light television or CCD (charged coupled device) camera and digitized into the computer.

In order to interpret the diffraction pattern correctly, the position of the pattern center, the distance between the specimen and the phosphor screen and the angle of tilt

must be determined or calibrated [52]. Figure 2.12 shows a schematic diagram of the relationship between the diffracted pattern and the tilted specimen. The most convenient method of determining the pattern center is by using a calibration specimen of known orientation, such a piece of silicon (surface normal is [001]) with cleaved edge lying along the [110] plane. [49,52]. The distance between the specimen and the screen can be obtained using the relationship:

$$L = N/tan\ \phi$$

where N and ϕ are shown in figure 2.12 and the angle of tilt is read off the tilt mechanism located on the SEM.

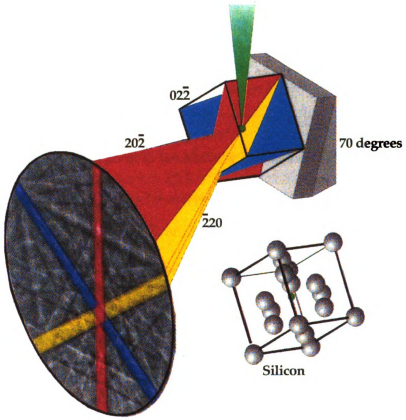

Figure 2.11. Schematic of electron diffraction in silicon with crystal planes and associated diffraction bands shown [50].

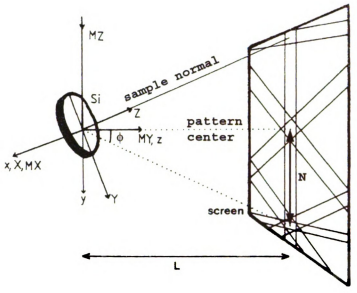

Figure 2.12. Schematic diagram illustrating the relationship between the diffracted pattern and the tilted specimen.

Individual orientation measurements are made at discrete points on the specimen defined by the beam controls. The locations of the points are defined by a grid area prescribed by the user (both the length and breadth of the grid area as well as the step size between the points). At each point in the grid, the backscatter Kikuchi diffraction pattern is captured. By selecting the expected crystal phases from a phase database, all possible orientations of the crystal under the beam are automatically indexed. The orientation of the area of interest is determined by considering the number, width and angle of the bands at the intersection [53]. An example of the EBSD pattern and the corresponding result of the computerized indexing are shown in figure 2.13. Euler angles that describe the orientation are recorded along with the coordinates describing the position on the sample surface. Thus it is possible to map the crystal orientation onto a color or grayscale and shading each point on the grid according to some aspect of the crystal orientation.

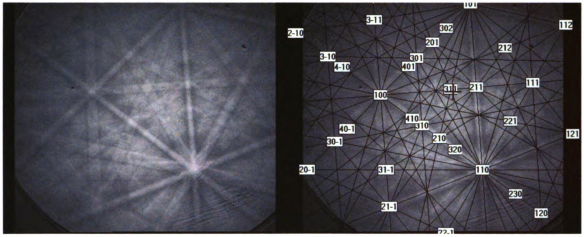

Figure 2.13. An EBSD pattern of TiAl at 25 kV and the corresponding result of the computerized indexing showing the poles/zones. There is one chance in three that it is correctly indexed.

The use of a highly collimated, stationary electron probe to focus on the specimen permits precise placement of the electron probe and the diffraction pattern so formed covers an angular range of more than 90 degrees [54]. As such several major crystallographic zone axes are usually included in the pattern. With advances in hardware and software, the computer can now control the stage or the beam travel such that the orientation at each point in a predetermined array can be automatically measured and stored providing a means of making large number of individual lattice orientation measurements.[14]. The resulting data set can be presented as maps containing diffraction information (figure 2.14) or an orientation imaging micrograph (OIM) [51,55]. This technique is known as Orientation Imaging Microscopy (OIM) and it has the ability to image all boundaries exhibiting absolute misorientation exceeding 1 degree [56].

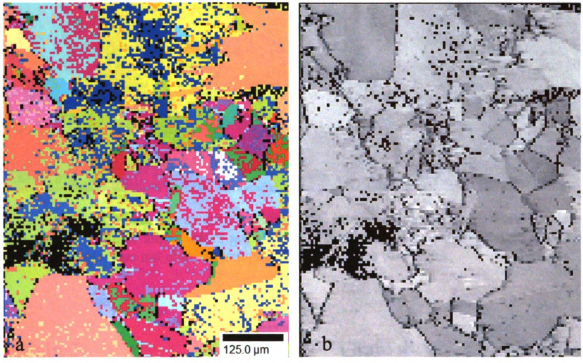

Figure 2.14. Inverse Pole Figure Maps (a) color (b) grayscale.

Although this technique can measure approximately 1800 lattice orientation within an hour [55] to determine grain orientations in cubic crystal, this technique does have a drawback. It is not able to successfully distinguish the small c/a ratio in ordered lattices, specifically γ-TiAl. The c/a ratio is 1.02 resulting in inter-band angles within 0.5 degrees of those for the cubic lattice [57]. Given that the EBSP pattern indexing has an intrinsic uncertainity of ~ 1 degree, it is not possible to reliably distinguish features with smaller angular variance. Thus the EBSP software will generate three orientations for any given grain, represented by the three colors in maps. Figure 2.15 shows a portion of the OIM and its corresponding BSE images containing grain 4 and 7. Note that the EBSP was not able to resolve the differences between grain 4 and 7 (shown with the same Euler angle colors). SACP composite maps, however, reveal differences between the two grains as shown in figure 2.16 by the location of superlattice bands.

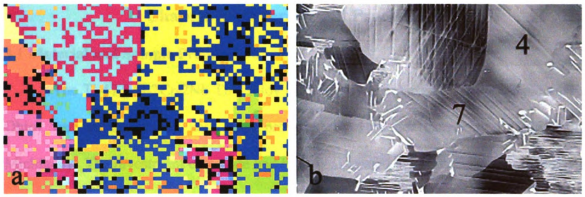

Figure 2.15. OIM map and its corresponding BSE image containing grains 4 and 7. Note that the set of Euler angle colors are similar in both grain 4 and 7, indicating that the EBSP technique was not able to distinguish between these two grains.

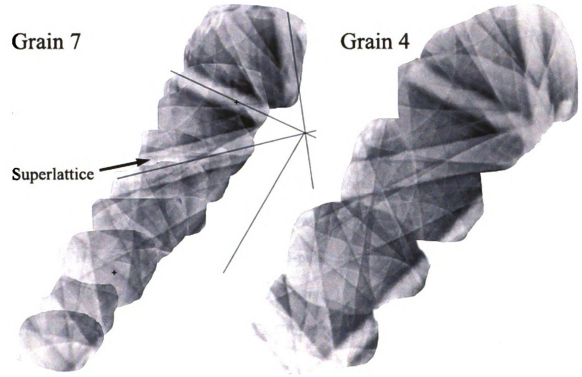

Figure 2.16. Two similar sets of SACP composites. Careful examination revealed superlattice [110> bands (marked) in Grain 7 whereas Grain 4 has one of the other [011> bands.

Chapter 3: Experimental Procedures

3.1 Material and Sample Preparation

The Ti-47.9Al-2Cr-2Nb TiAl alloy provided by GE Aircraft Engines (Cincinnati, Ohio) was an investment cast plate produced by Howmet Corporation (Whitehall, Michigan). The investment cast plate had been heat treated at 1093° C for 5 hr, followed by a hot isostatic pressing (HIPing) process at 1205° C for 4 hr and further heat-treated at 1205° C for 2 additional hours before rapid cooling. Samples measuring 21 x 3.5 x 2.0 mm were cut from this investment cast plate (figure 3.1). The specimens were then epoxy bonded to an aluminum backing material with similar dimensions to facilitate controlled crack extension (this was necessary due to the low toughness of TiAl) as shown in figure 3.2. The bonded specimens were pressed together with approximately 1 lb weight and cured in a vacuum oven maintaining a pressure of 250 psi and 80°C for 24 hours. A 1 mm notch was cut using a 0.3mm thick diamond saw and the surface was then ground using a series of SiC grinding papers ranging from 240 to 600 grit size followed by fine polishing using alumina powders ranging from 5 microns through 0.3 microns. The specimens were then electro-polished using a solution of 5% perchloric acid, 30% butanol in methanol at ~ -60°C using 15 Volts for 20 minutes to achieve a surface suitable for SACP, EBSP, and ECCI imaging.

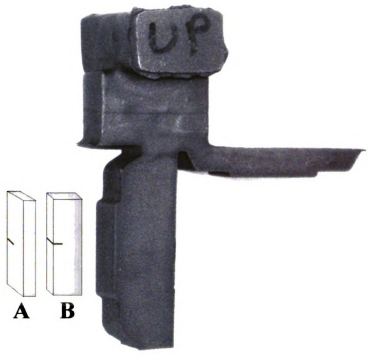

Figure 3.1. A portion of the investment cast plate used in this study. Schematic diagram showing orientation of sample A and sample B with respect to the investment cast plate is shown.

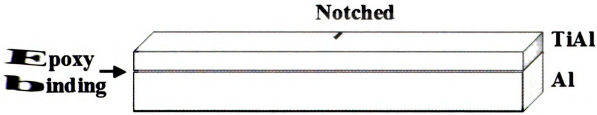

TiAl : 3.5 x 2.0 x 2.1mm
Al : 3.5 x 3.0 x 2.1mm

Figure 3.2. TiAl alloy was bonded to an aluminum backing to facilitate the controlled crack extension.

3.2. Microscopy

All microscopy (SACP, ECCI, and EBSP) was carried out on a CamScan 44FE SEM. The machine is fitted with a selected area channeling module for obtaining selected area channeling patterns. Secondary electron signals were captured using an Everheart-Thornley (ET) detector mounted on the side of the chamber and the backscattered (BSE) signals were captured via a four quadrant polepiece-mounted silicon diode type BSE detector. A CCD camera collected EBSP patterns via the phosphor screen in a unit that projected into the chamber from the side of the microscope chamber. All microscopy was carried out using an acceleration voltage of 25kV, a probe current approximately 20-40nA, and a beam convergence angle (2α) of approximately 8mrad. A working distance of 10 mm was maintained for all microscopy work except for EBSP analysis, where the working distance was set at 31 mm. The HKL **CHANNEL+** software package was used collected and interpret the diffraction patterns after it was calibrated with a cleaved {001} surface of a silicon wafer. The EBSP data thus obtained was then converted to an **.ang** file to be read using **TSL-OIM™3** software. This software provided better tools for analyzing orientation and related aspects of crystalline microstructures than the features in hkl version 4.2 software package. This software presents crystal orientation data in either euler angles or the (hkl)-[uvw] nomenclature (e.g. grain normal and grain tensile loading direction or tilt axis).

All images (BSE, SE, SACP and ECCI) were captured and averaged, typically using 8 frames, by the framestore feature that is integral to the CamScan 44FE SEM. These images were stored as 640X480 pixel digital images using an external personal computer (PC) equipped with a frame grabber card.

3.3. Initial condition of near-γ TiAl alloy

The microstructure of the near-γ TiAl specimen consists primarily of γ phase TiAl and some partially decomposed (α_2+γ) colonies as shown in figure 3.3. An OIM scan reveals approximately 92% TiAl and 8% Ti_3Al. Close examination of the undeformed alloy (figure 3.4 and 3.5) showed that while some grains showed little or no deformation twins, high densities of deformation twins were observed in others. This variation in the density of the deformation twins in the surrounding grains suggests that activation of deformation twins during processing may have been sensitive to crystal orientation. In general, these pre-existing twins (either little or high density) were uniformly distributed within the grain. A comparison of the preexisting twins before and after deformation due to the 4-point bending will be discussed further in section 3.8.2.

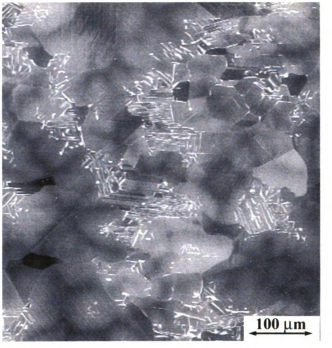

Figure 3.3. Microstructure of the near-γ-TiAl showing the equiaxed γ grains and small clusters of α_2 colonies.

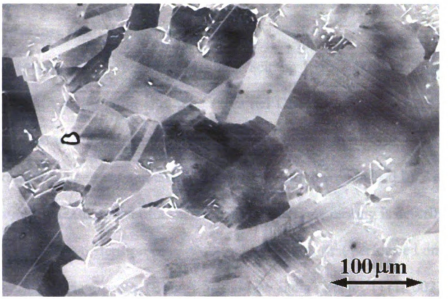

Figure 3.4. Undeformed near-γ TiAl alloy showing pre-existing deformation twins. In some regions, a higher density of the pre-existing twins was observed (bottom right edge of the image). The densities of the pre-existing deformation twins vary from grain to grain.

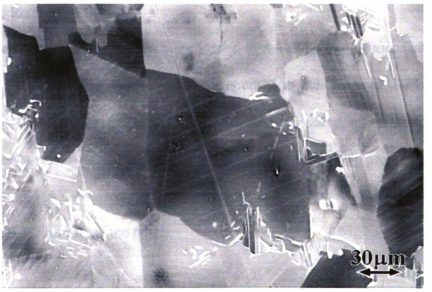

Figure 3.5. Undeformed near-γ TiAl alloy showing pre-existing deformation twins. The densities of the pre-existing twins vary from grain to grain. But overall, the pre-existing twins were uniformly distributed throughout the grain.

3.4. X-ray –texture analysis

Texture analysis was performed using a Scintag XDS 2000 x-ray diffractometer using 35kV, 40mA and a 2mm slit. The Preferred Orientation Package – Los Alamos (popLA) software was used to obtain the necessary information. The process used to obtain a texture measurement and analysis was similar to that described by Kallend et al. [58] and a similar measurement of a specimen from the same casting is described in [59]. Basically this was a two steps process. A 2-theta scan was first performed on sample B to obtain the appropriate peaks (Bragg) of the low indice planes (111, 002, 200, 022, 220). The peaks and suitable background 2-theta values were subsequently input into the software for the subsequent pole figure scan.

3.5. Sample loading in the SEM

The electropolished samples were loaded in a 4-point bend fixture attached to an E. Fullam deformation stage (see figure 3.6) mounted in the Camscan 44FE FEG-SEM. Bending was performed at the minimum attainable crosshead rate (0.006 mm/s) and stopped when a crack nucleated and propagated from the notch root. In one of the samples, (sample A), the load was recorded at 123 lbs when the crack propagated approximately 1.2 mm from the notch.

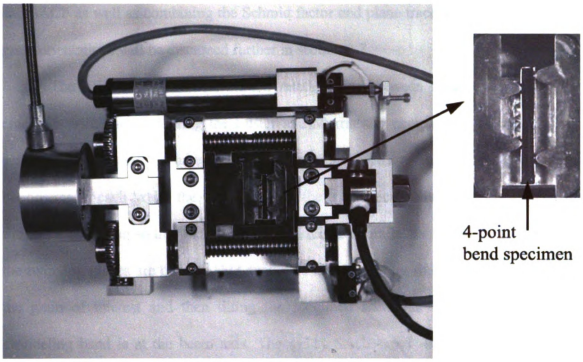

Figure 3.6. Fullam Deformation stage fixed with a 4-point bend fixture (shown at higher magnification on the right side) and notched specimen in place.

3.6. Grain Examination

The cracked specimens were removed from the stage in air, and immediately mounted on a specimen holder to permit easy tilting and subsequent analysis. The samples were immediately returned to the SEM where they remained in vacuum during all of subsequent analysis (though they was exposed to air when the chamber was opened by other users several times per week). Following the bending and arrested fracture, the entire crack path of sample (A) was characterized and grains that were close to the crack tip were examined in detail. Using a combination of EBSD/SACP, as well as Schmid factor/plane trace analysis, the orientations of the grains and slip systems were determined. The Schmid factor calculations were based on the assumption that the notched 4-point bend configuration results in large tensile stresses normal to the notch at the notch tip and subsequently at the primary crack tip. The technique of using EBSP

and SACP as well as combining the Schmid factor and plane trace analysis to determine grain orientations will be discussed further in section 3.7.

The orientation and deformation relationships between adjacent grains at the crack tip were analyzed using the Luster and Morris slip compatibility factor [36] for active slip systems. To assess the local strain field due to twinning near the grain boundaries in each grain, the true widths of the mechanical twins were determined by tilting the specimen so that the beam axis was aligned parallel to the twinning plane. As the twinning planes are of the {111} type, this is achieved by first obtaining a SACP of the grain of interest and then tilting the specimen such that the appropriate {111} channeling band is at the beam axis. The {111} SACP-band will be parallel with the corresponding {111} plane trace. Although in the typical ECCI technique the beam axis is aligned to one of the edges of the band (Bragg condition), to obtain good contrast of the deformation defects (dislocations), as shown in figure 3.7a, this was not done in this study. Instead it was found that the sharpest images of the twins were obtained when the beam axis was centered in the {111} channeling band (figure 3.7b), which results in the twins being imaged directly edge-on.

The relationship between the width of the twins and the observed microcracks along the grain boundaries were analyzed. A sampling of the grain boundaries that were intact or cracked near to/or in the path of the propagating crack was statistically analyzed to allow the development of a crack growth parameter.

After preliminary characterization, the specimen was reloaded to determine if the modeling approaches described later could predict the crack path resulting from further deformation. This modeling approach was then used to analyze the crack path on a

similar specimen, sample B and finally the Fracture Propagation Parameter and its modeling approach were then compared with the Fracture Initiation Parameter using Simkin's existing sample data.

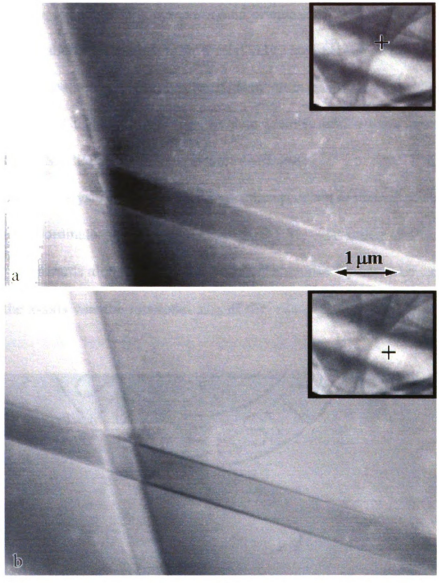

Figure 3.7. ECCI images of two different twinning systems, each displaying 2 fine micro-twins separated by approximately 1 micron. a) Aligning the beam axis (+) to one edge of the {111} band. (note contrast from dislocations). b) Aligning the beam axis (+) to the center of the band. The {111} twins corresponding to the {111} channeling band are in sharp contrast when the beam is aligned to the center of the band.

3.7. Grain Orientation

3.7.1. Use of EBSP and SACP to determine grain orientation

Determination of the grain orientations was accomplished by using an approach that combined the speed of Orientation Imaging Microscopy (OIM) and the unique ability of SACP analysis to identify the correct crystal orientations. OIM will provide a large number of orientation measurements in a relatively short period of time. Since three orientations were commonly observed in a given grain based upon the EBSP pattern indexing, the SACP technique was then used to identify which grain orientation was correct, since the SACP can identify superlattice reflections.

All EBSP analysis was carried out with the specimens oriented according to the sample space coordinate system shown in figure 3.8. The notch and crack growth direction is downwards along the negative y-axis. When the 4-point bend specimen was tilted 70°, the x-axis was the rotational axis of the specimen and its orientation did not change.

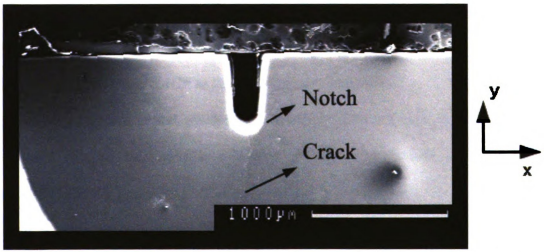

Figure 3.8. A portion of the 4-point bend specimen aligned in relation to the microscope screen.

3.7.2. Computations of Stereographic Projection

Given any set of grain normals and their tensile loading direction, it is easy to compute and plot a stereographic projection with the principle poles and plane traces projected in relation to the normal plane of the grain of interest. This is shown in figure 3.9. Each trace can be easily identified by a color code as shown. This program (stereograph.nb) was written by Dr. Mason, Adjunct Professor, Mechanical Engineering department, MSU and was carried out using Mathematica 4.2.

3.7.3. Plane Trace Computations

In order to identify the plane traces in this material, Dr. Mason also wrote a program that plots plane traces with respect to any given grain normal and tensile loading direction. The mathematical details can be found in [15]. Plotting the plane trace (using 111_Trace_Projection.nb) was also carried out using Mathematica 4.2 and an example of the plane trace with respect to the grain normal (3,2, -21) and tensile loading direction is shown in figure 3.10. Each plane trace has been identified as shown in the figure.

3.8. Analysis of Grain Orientation

3.8.1. Use of EBSP and SACP to determine grain orientation

The grain normal and rotational axis vectors obtained from the EBSP analysis were input into the stereographic projection program described in section 3.7.2 and plotted as shown in figure 3.11. The grain normal was marked "+" in the stereographic projection. The diffraction pattern obtained from an EBSP usually provided around 65 degrees of pattern information whereas the angular spread for an SACP was only about 8 degrees. However, this 8-degree limitation was overcome by tilting the specimen to

obtain similar information obtained in the EBSP patterns. However the stage can only be tilted in one direction, so to achieve a larger angular view; the specimen was rotated and tilted to obtain the necessary information using SACPs. By collecting SACPs at specific tilt and rotation angles, composite SACP maps were obtained.

In figure 3.11 a stereographic projection is shown with a schematic of the specimen and the tilt needed to obtain information in different parts of diffraction space using SACPs. To view diffraction space above the pattern center ("+") the specimen must be aligned such that the notch is at the bottom of the specimen and tilted about the specimen x axis to obtain the necessary diffraction information (see figure 3.11, sample A with the direction of the tilt arrow). To obtain information viewed in the direction towards the left, the specimen must be tilted as shown in figure 3.11, sample D, with the direction of the tilt arrow indicated. Likewise, the same is done for the other two directions as shown in samples B and C. The tilt mechanism that was fitted to the present microscope (CamScan 44FE SEM) allows tilt in one specific direction. Consequently, in order to achieve the desired tilt shown in figure 3.11 it was necessary to rotate the sample first to the orientation that allows for tilting about the correct axis. Figure 3.12 shows how sample D (shown in figure 3.11), was rotated through 90 degrees, counterclockwise, in order to allow proper SACP imaging of similar diffraction pattern shown by the stereograph.

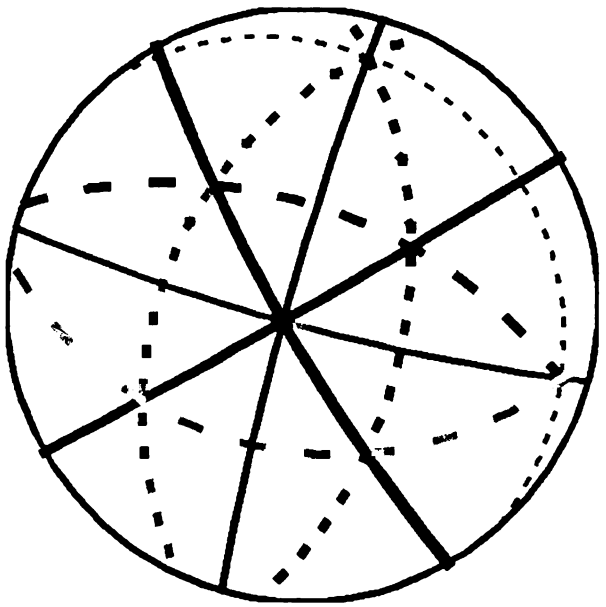

Color	**Traces**
Red (thin-solid)	(100)
Purple (thin-solid)	(010)
Orange (thin-dashed)	(001)
Black (thick-solid)	(110)
Blue (thick-solid)	(1-10)
Green (thick-dashed)	(101)
Cyan (thick-dashed)	(-101)
Blue (thick-dotted)	(011)
Magenta (thick-dotted)	(01-1)

Figure 3.9. A computed stereographic projection with the grain normal (3,2, -21) and a horizontal tensile loading direction [4,15,2] and its corresponding color code labeled in the inserted table.

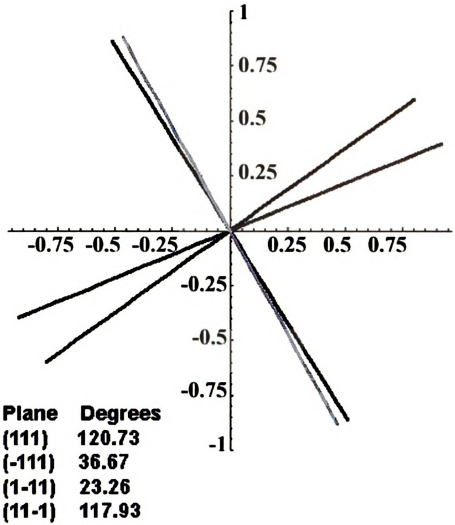

Figure 3.10. Plot of the plane trace with respect to the grain normal, (3,2, -21), and tensile loading direction, [4,15,2].

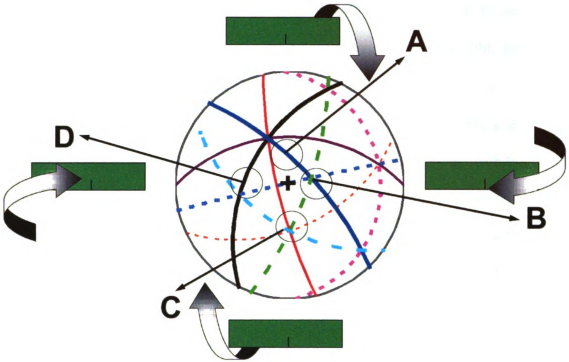

Figure 3.11. In order to confirm orientation information obtained from a proposed stereographic projection, the specimen must be rotated and tilted in order to obtain SACP patterns that can be compared to the three stereographic projections obtained from OIM data. If the stereographic projection is viewed from the grain normal (marked "+") towards the left, then the specimen has to be rotated such that the notch is at the bottom of the sample and tilt to the required angle to obtain the needed information.

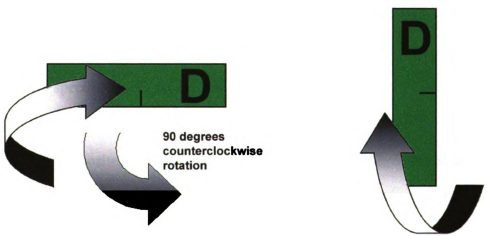

Figure 3.12. The tilt mechanism allows only tilt in one direction. Thus it was necessary to rotate the sample to a specific orientation first before tilting to the correct angle.

As an example, to determine the orientation for grain 4, the analyzed EBSP data provides three possible grain orientations (figure 2.15 of section 2.14) because of its inability to resolve the small c/a ratio in the γ-TiAl alloy. The stereographic projections of these three potential orientations are plotted in figure 3.13. For the γ-TiAl alloy, the [110> bands are superlattice bands and are color coded in solid blue or black lines. The SACP composite map of grain 4 reveals a superlattice band (highlighted with black bold parallel lines) approximately 25 degrees above the grain normal. This observation corresponds with stereographic projection ***b***, which has the blue [110> (superlattice band) in the same orientation as observed in the SACP composite. Note that stereographic projection ***a*** has a magenta dotted [011] color band and stereographic projection ***c*** has a cyan dashed [-101] color band in the same direction thereby confirming that stereograph ***b*** is the correct orientation for grain 4 (grain normal (2,17, -14) with rotation axis [4,2,3]).

A SACP composite map was used in the above example to illustrate the location of the grain normal with respect to the observed patterns and how the observed SACP composite map relates to the stereograph as the specimen (with the notch shown on the top of the specimen) is tilted about the x-axis.

In the next example, the specimen had to be rotated (with the notch shown on the left side of the specimen) and tilted in order to obtain the SACP for the superlattice bands. Though a SACP composite map is shown (see figure 3.13), it is not necessary to generate such a composite map, since collecting the critical observation of a superlattice band in the microscope (along with the tilt information) is sufficient to identify whether stereographic projections a, b, or c is the correct grain orientation. Three possible stereographic projections of a grain are shown in figure 3.14 along with an SACP image

obtained when the specimen was tilted ~ 5 degrees with the notch positioned as shown in the figure. The observed [110> superlattice band matches the traces in stereographic projection c, thereby indicating the correct grain normal is (6,4,1) with a rotational axis of [4, -7,4].

There are cases when it is not possible to image a particular superlattice band because the required tilt is too high to generate a proper SACP imaging condition. In such a case, the same logic can be used in reverse, to eliminate a stereograph simply because it predicted a superlattice band whereas the SACP did not reveal it. By eliminating two out of the three stereographic projections, the third stereographic projection can be concluded as having the correct orientation. This has been shown in figure 3.15.

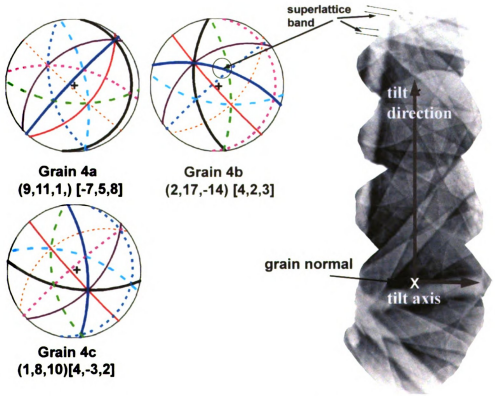

Figure 3.13. Three possible stereographic projections obtained from an EBSP scan, and a SACP composite of grain 4. The SACP composite reveals a superlattice band, approximately 25 degrees from the grain normal. This matches stereographic projection b having grain normal (2,17, -14).

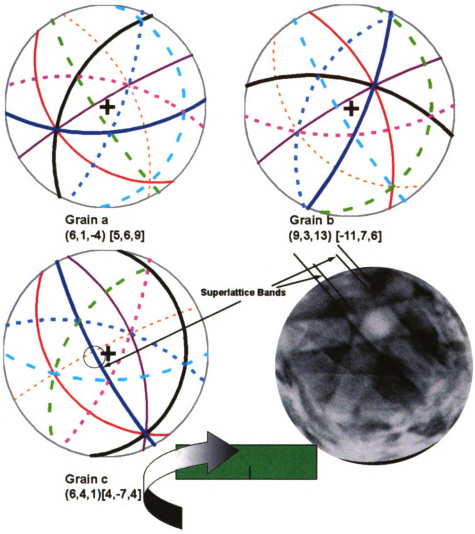

Figure 3.14. Three possible stereographic projections (a-c) and the observed [110> superlattice band observed in the SACP when the specimen was rotated such that the notch is at the bottom and the specimen is tilted ~5 degree as shown.

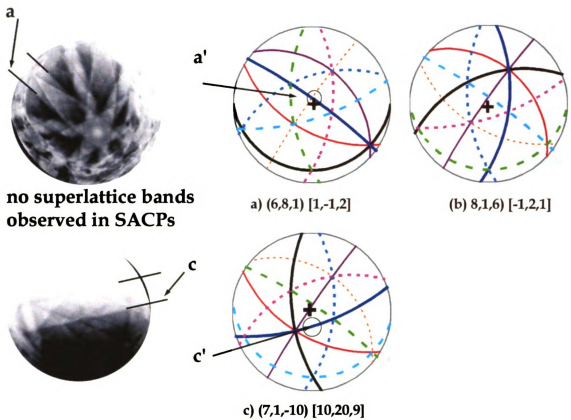

Figure 3.15. Three possible stereographic projections for grain 8. The band ***a*** from the top SACP corresponds to the superlattice band ***a'*** shown in the stereographic projection **a** and band ***c*** from the bottom SACP corresponds to superlattice band ***c'*** (stereographic projection c). Since both bands ***a*** and ***c*** do not show any superlattice information, stereographic projections **a** and **c** are incorrect and are eliminated. Stereographic projection **b** is therefore the correct solution for grain 8.

3.8.2. Use of Schmid factor and trace analysis to determine grain orientation

With smaller or heavily deformed grains, it is difficult to obtain a good SACP with the superlattice information necessary to determine the correct grain orientation. In such cases, given the three possible grain orientation solutions, it is possible to plot the plane traces and obtain each Schmid factor corresponding to the plane trace. This information (Plane traces and Schmid factors) can be compared with the deformed grains to match dominant twin traces with the highest Schmid factors.

The Schmid factor, m, is based on the computation of the product of two cosine angles; firstly, the angle between the normal of the twinning planes and the tensile loading direction and secondly, the angle between the twin vector for that particular plane and the tensile loading direction. A schematic is shown in figure 3.16. This calculation required expressing the plane normal and slip directions in the specimen coordinate system, and was incorporated into the Fracture Propagation Parameter Program (see Appendix 3).

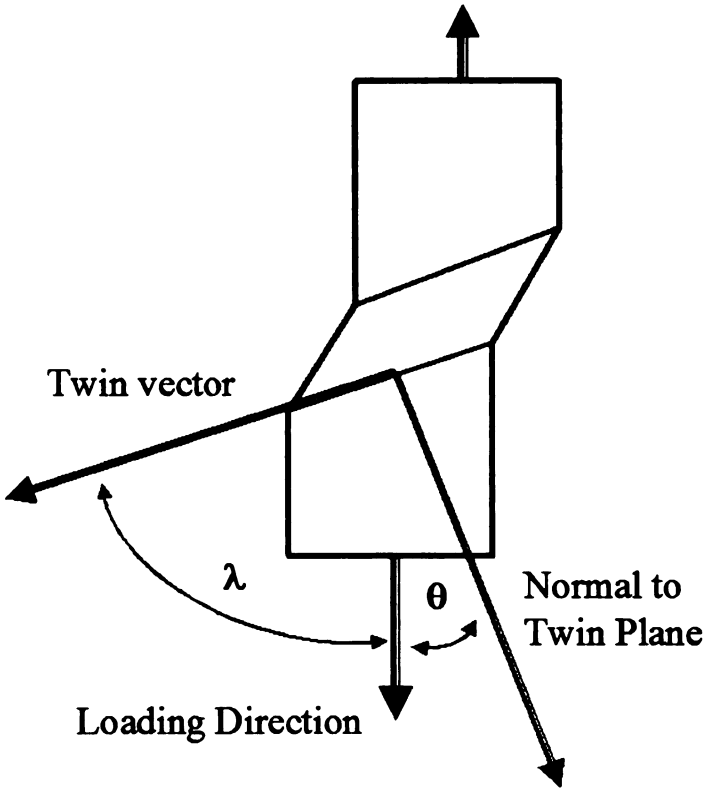

Figure 3.16. Diagram for calculating the Schmid factor.

In order to provide a good analysis of the plane traces in this alloy, the characteristics of the pre-existing twins and the deformation twins is needed. A comparison of the pre-existing twin and the deformation twins due to the induced 4-point bend loading is shown in Figure 3.17. Figure 3.17a showed fairly visible preexisting

twins on several grains. Figure 3.17b showed the effect of the propagating crack as it passes on the right of these images. Deformation twins were activated in most of the grains but these deformation twins were not as uniformly distributed as previous noted (figure 3.4 and 3.5).

Consider grains α, β, δ, κ and ϕ in Figure 3.17. Most of these grains showed increased twin activity within the grain after deformation and the increased twin activities were not uniformly distributed. In grain ϕ, the twin activity is very localized with most of the deformation twins located nearer to the crack. Grain $\alpha$with a large annealing twin in the grain had visible preexisting thin twins widely spaced out within the grain, as shown in Figure 3.17a. But with the crack propagating nearby (to the right), these thin twins had grown thicker and were highly intensified. The vaguely visible preexisting twins in grain β were also highly intensified after the crack had propagated nearby. Grain κ was the only grain that showed no sign of any twin activity in either before or after the crack had propagated nearby.

These images (other than grain κ) are typical and are representative of the effect of the crack on the activation of the deformation twins on the grains. In general, preexisting twins were widely spaced. These preexisting twins were thin and were uniform in thickness. Non-preexisting twins, on the other hand, tend to vary in twin thickness, and/or tend to have a larger number of twins clustered together nearer to the crack region.

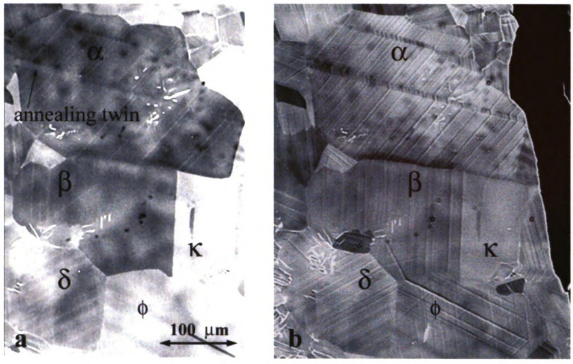

Figure 3.17. Comparison between pre-existing and deformation twins due to the induced 4-point bend loading.

With the background information on the pre-existing twins and the data from the plane trace and Schmid factors, the grain orientations for grains whose SACP is not possible can be analyzed. As an example, the plane traces of the three possible grain orientations for grain I were plotted, and superimposed onto the grain as shown in figure 3.18. In the backscattered electron (BSE) image on the far right, the dominant twinning system is observed to have propagated over another earlier set of twins. The observed dominant plane traces (colored blue) correspond well with the high Schmid factors of 0.41 for the (-111) plane in grain Ic. Similar traces in potential orientations ***a*** and ***b*** showed negative Schmid factors (-0.12 and –0.28 respectively) for the observed dominant plane traces. On the other hand, another set of horizontal twins was highly visible. From the characteristics of pre-existing twins and the observed location of these horizontal twins with respect to the direction of the propagated crack, this set of twin is

most likely to have preexisted before the deformation. This is because with the crack running from the top to the bottom of the image and if that (horizontal) twin was activated, it would have been more localized closer to the crack. On the other hand, the other set of twin (colored blue) showed higher twin trace intensity nearby the crack path then away from the edge. This is evidence that this twin (colored blue) must be the dominant twin that was activated. Thus the grain normal (2,8,5)[13, -7,6] is most likely the correct orientation for grain I. The horizontal twins in the neighboring grain (grain H) to the right have a Schmid factor of 0, and the vertical twins have a Schmid factor of 0.41. From a similar analysis presented later, it is evident that the horizontal twin blocked the vertical twins, implying that they (the horizontal twins) were preexisting.

This method works very well with grains that are highly deformed, since the highly deformed grains will show dominant twinning systems that allows comparison with the computed plane traces. This method was used when the usual SACP method failed to provide a good pattern to analyze the bands (due to a small grain size or large amount of deformation. However, unlike the cases described above, the degree of certainty is not 100%, because the local stress state may be different from the global stress state, and/or pre-existing twins can complicate the analysis.

The tools and analytical techniques described in this chapter allow a systematic approach to investigating the slip/twinning deformation process in detail. This will be dealt with in the next chapter.

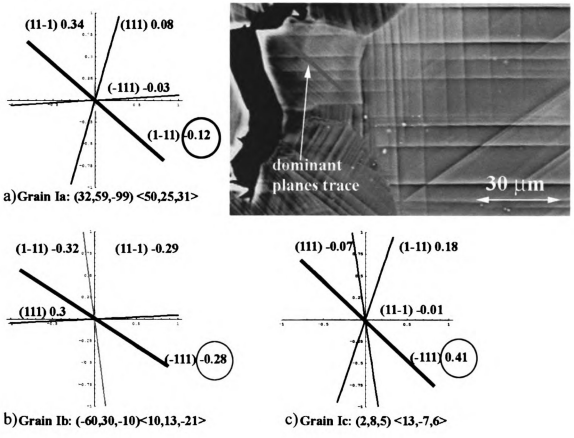

Figure 3.18. BSE image of grain I with one dominant twinning plane (colored blue). Note how the dominant plane traces propagate across another set of preexisting twins Inserts a-c are plots of the three possible plane trace solutions with Schmid factors indicated for the true twinning system on that plane. The observed dominant twinning system corresponds well with plane trace plot c, (grain Ic) displaying high Schmid factors (0.41) for the dominant plane traces. Plane trace plots a and b ((grain Ia and grain Ib respectively) had negative Schmid factors for the observed dominant twin traces.

Chapter 4: Results from Initial Crack

4.1. Overview

A texture analysis was performed using x-ray diffraction to determine the preferred crystal orientation of these γ-TiAl alloys. Sample A was subjected to a 4-point bend loading to initiate a crack to grow and propagate mid-way through the specimen width before arresting the crack. Defect analysis of dislocations and twins was done to determine the extent of plastic deformation within grains near the crack path. Twin thickness was imaged using ECCI imaging and the thickness measured using the NIH Image software. Crystal orientations were determined using a combination of EBSP and SACP techniques, as described in chapter 3.

4.2. X-ray Analysis of near-γ TiAl alloy

An x-ray pole figure scan of Sample B (figure 4.1) showed that the specimen had strong peaks from a few strongly diffracting (large) crystals, but with no obviously preferred orientations, as indicated by the second set of pole figures where the specimen was oscillated under the beam to improve sampling statistics. The oscillated pole figures are more suitable for comparing the effect of texture on crack characteristics.

In view of this analysis and the orientation of samples A and B, both had the dominant tensile stress in the same direction (TA). For Sample A, the TD direction at the notch root contract due to the bending process (the back end will expand and get thicker). Since there are more crystals near [111], the stiffest orientation (218 GPa)[58], there will be less elastic strain along the crack front (TD direction) for specimen A than in specimen B, which would have more, as the ND direction is more compliant (139

GPa)[58] in [100] direction), allowing more elastic strain in the ND direction at the crack tip, and perhaps, more elastic strain incompatibility.

In terms of plastic deformation, Specimen A needs to plastically expand in the TD direction. In that direction, there is a small fraction of material where ordinary dislocations have a high Schmid factor, and a small fraction of material where true tensile twins have a high Schmid factor. In contrast, Specimen B needs to expand plastically in the ND direction, and it has a higher volume fraction of grains with high Schmid factors for twins and ordinary dislocations, and comparatively less material in hard orientations near 001.

Taken together, it appears that more plastic deformation probably occurred in specimen B than in A, leading to more work hardening, and hence higher stress before the final crack propagated.

4.3. Initial loading of the 4-point bend specimen

Initial loading of the 4-point bend sample (a) resulted in mixed mode cracking with the crack running approximately 1.2 mm from the notch root as shown in figure 4.4. The load was 126lbs when the crack propagated from the notch. Extensive twin and dislocation generation is apparent ahead of the crack tip as shown in figure 4.3. This crack was observed to alternate between intergranular fracture and cleavage (Figure 4.4). Areas where the crack was intergranular are highlighted in figure 4.4.

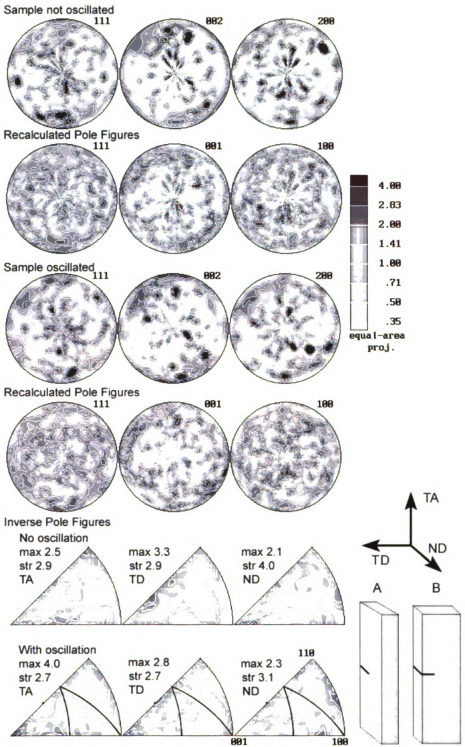

Figure 4.1. X-ray pole-figure scan of specimen b with the orientation indicated reveals a strong heterogeneous texture. The effect of oscillation alters the texture measurement slightly, and inverse pole figures show that there are no highly preferred crystal orientations. Great circle passing through {101} and {111} poles are shown, and the little nub shown in the pole figures indicate 112 directions.

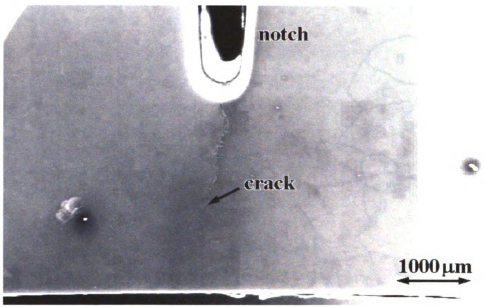

Figure 4.2. Secondary electron (SE) image of the crack running approximately 1.2mm from the root of the notch.

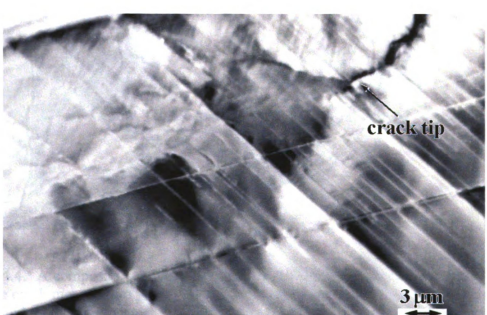

Figure 4.3. High magnification ECCI images of the crack tip showing extensive plastic deformation ahead of the crack tip. Both twin and dislocation contrast is observed.

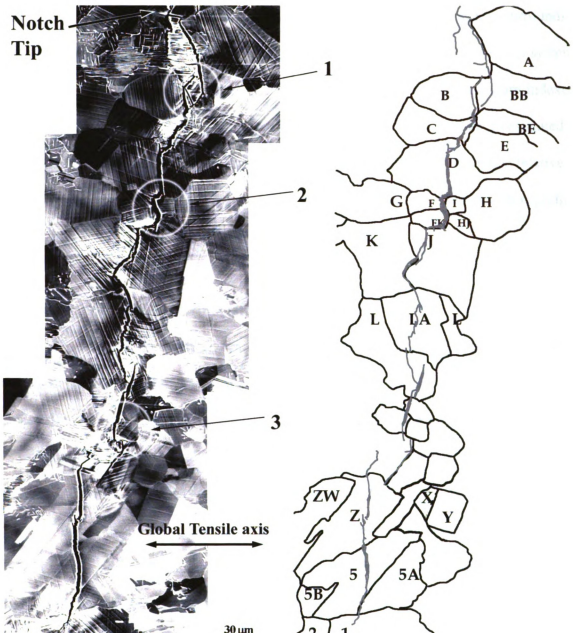

Figure 4.4. A composite backscattered electron (BSE) image of the crack path showing how the crack moved from intergranular to transgranular and back to intergranular. The intergranular crack regions are highlighted and numbered 1 – 3. The notch is located at the top of the image while the arrested crack tip is located at the bottom of the image. A schematic of the layout of the grains is shown on the right. The tensile direction is horizontal.

.

Large amounts of plastic deformation are also evident in the grains surrounding the arrested crack tip shown in figure 4.5. In this figure, traces of different slip systems are evident in the surrounding grains. The plane traces of grains 1, 2, and 4 are indexed. The region indicated by arrows (Start and End) in figure 4.5 was further investigated at higher magnification as shown in figure 4.6. This image (figure 4.6) is rotated relative to figure 4.5 and shows microcracks generated along the grain boundary between grain 1 and grain 2.

4.4. Width of twins and shear strains

The width of the twins was measured directly from higher magnification images (for example, see figure 4.7) with an accuracy of +/- 20%. To check this approach, selected images were scanned and analyzed using the NIH Image analysis software. Full-Width-Half-Max (FWHM) measurement of intensity plots of selected areas (see figure 4.8) resulted in comparable twin thickness measurement to those measured manually.

Figure 4.9 shows a plot of the twin thickness with respect to the location along the grain boundary for grain 1. Twins that correlate with microcrack formation are labeled. In general, twin widths greater than 175 nm were correlated with microcracks. The exception is microcrack #3, which was associated with a group of closely spaced finer twins with a total width of 300 nm. All the microcracks observed opened asymmetrically in relation the twin generated at the grain boundary. This is shown in Figure 4.10.

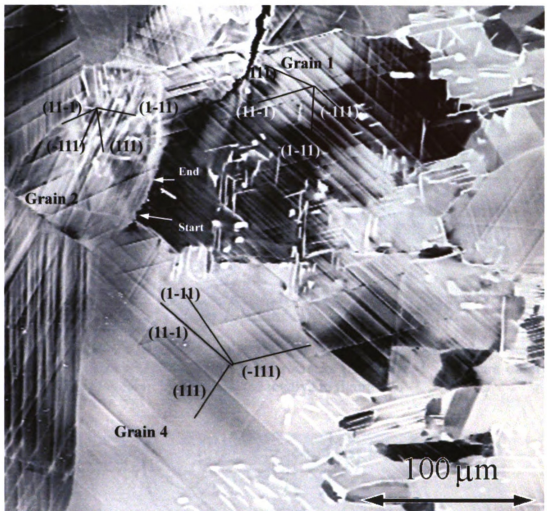

Figure 4.5. BSE image showing the arrested crack tip and the surrounding grains 1,2, and 4. The tensile axis is horizontal. The local strain along the grain boundary between grain 1 and grain 2 was studied between the indicated arrows showing the start and the end of the strain computation.

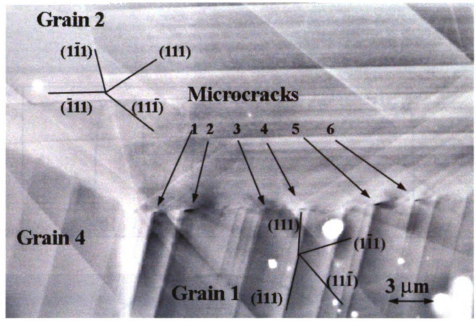

Figure 4.6. ECCI image shows the leading (-111) twins from grain 1 and the corresponding plane traces in grain 2. Microcracks (numbered 1 – 6) were observed along the grain boundary. Image is rotated relative to figure 4.5.

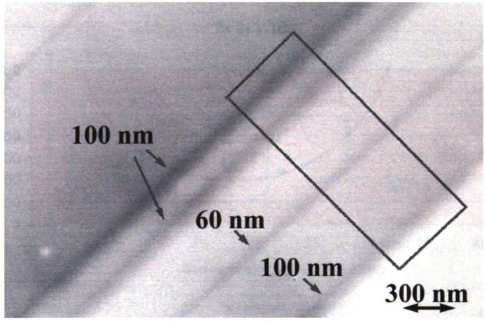

Figure 4.7. High magnification ECCI image of twins. Dimensions were measured directly from this image. The highlighted region (rectangular) was analyzed using the NIH Image Software as shown in figure 4.8 and resulted in comparable FWHM thickness measurements.

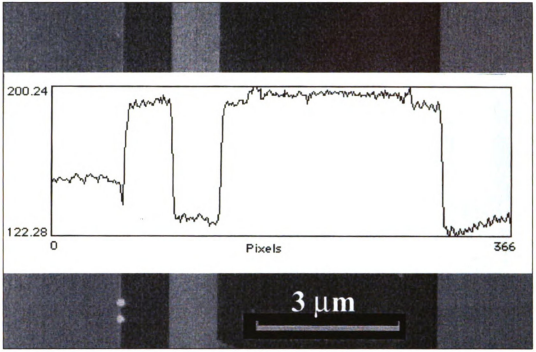

Figure 4.8. Examples of two twin measured using the NIH software to quantify the gray scale. The intensity plot was superimposed over the high magnification BSE image.

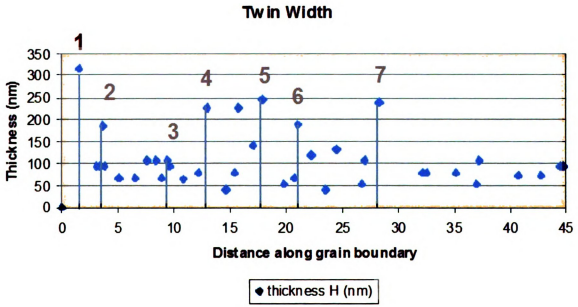

Figure 4.9. Plot of twin width vs. position along the grain boundary. The indexed numbers correspond to the observed microcracks along the grain boundary. Microcrack #7 s not shown in figure 4.6.i

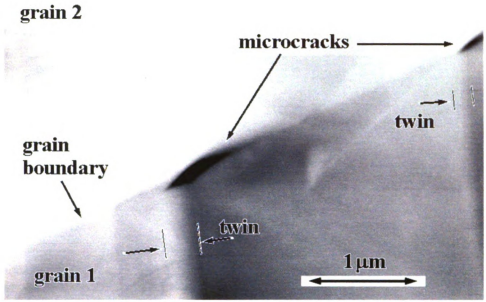

Figure 4.10. High magnification ECCI image of two microcracks, 5 and 6, (see figures 4.5 and 4.6 for location of these microcracks). Both microcracks opened asymmetrically in relation to the twin generated at the grain boundary.

4.5. General observation of deformation twins and dislocations

It was generally observed that if strain from the twin shear within one grain was accommodated or transferred to the adjacent grain, it was either by the generation of dislocations and/or another set of twinning planes in the adjacent grain, as shown in figures 4.11-4.13. Figure 4.11 shows two grains, (labeled x and y) located ~100 microns from grain 5A in sample A (see figure 4.4). A higher magnification image of the highlighted region is shown in figure 4.12. In this figure (figure 4.12), two plane traces, y1 and y2 (from grain y), were observed to have some correlation with dislocation activity in grain x. A higher magnification BSE image (figure 4.13) showed that the twin plane y1 resulted in the generation of dislocations across from the grain boundary, as shown by the high contrast from a large dislocation density. Twin plane y2, on the other

hand resulted in the formation of deformation twins (plane x1) in the adjacent grain x (figure 4.12).

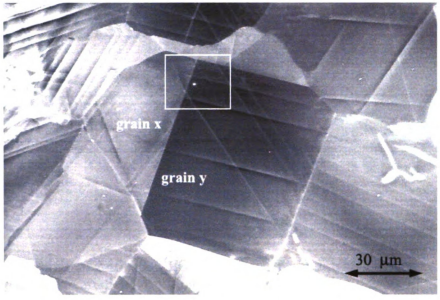

Figure 4.11. BSE image of neighboring grains x and grain y. The region of interest is highlighted and shown in figure 4.13.

.

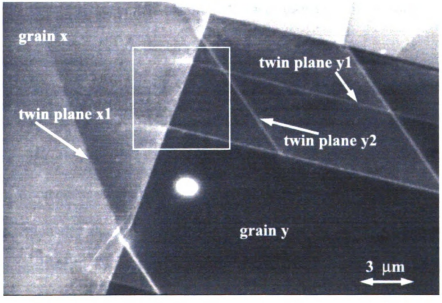

Figure 4.12. ECCI image of neighboring grains x and y that were highlighted in figure 4.12. Note that the end of twin plane y1 (at the grain boundary) showed a large amount of plastic deformation in grain x that gives high contrast. Also, there is correlation between twin plane y2 to twin plane x1.

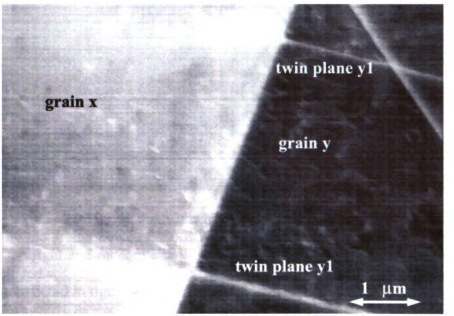

Figure 4.13. A high magnification ECCI image of the highlighted region in figure 4.13 reveals high contrast variations resulting from a high dislocation density in grain x ahead of the twin plane y1.

4.6. Reloading of the cracked specimen.

When this first specimen (sample A) was re-loaded in 4-point bending, the microcracks at the boundary between grain 1 and grain 2 opened further. At the same time, the surface relief from the deformation twins associated with the grain boundary microcracks increased (Figure 4.14a). Examination of this surface relief using secondary electron imaging reveals that the magnitude of the deformation twin topography decreased with distance away from the grain boundary (Figure 4.14b). An ECCI image of the same region also showed deformation twin contrast diminishing with distance from the grain boundary (Figure 4.15). Microcracks also nucleated along the grain boundary between grain 1 and grain 4 during the reloading of the specimen, as shown in figure 4.16.

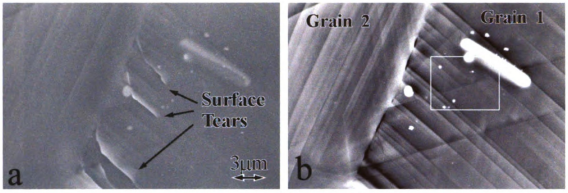

Figure 4.14. a) Secondary electron image showing surface features that diminish with distance from the grain boundary. b) ECCI image reveals the heavily twinned planes in grain 1 on the right and moderate twin activity in grain 2. Note that microcracks have grown compared with figure 4.6. Some twins terminate in the grain in the boxed region, shown in more detail in figure 4.15. The tensile axis is horizontal.

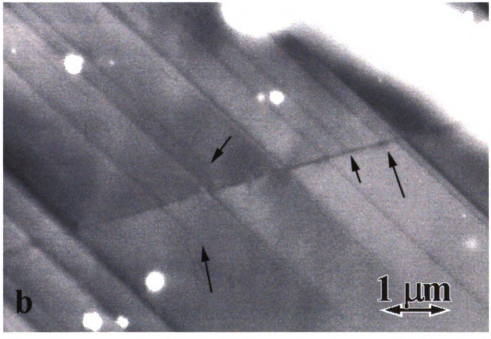

Figure 4.15. Inset from figure 4.14b shows traces of twinning planes terminating in the interior of the grain (arrows).

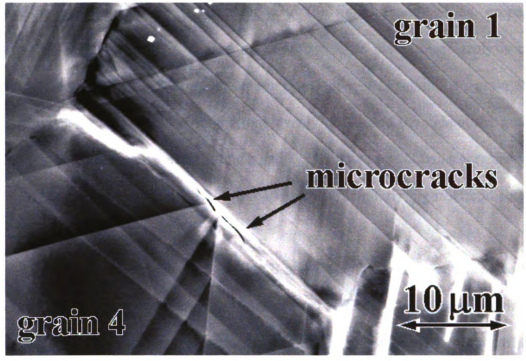

Figure 4.16. Microcracks nucleated along the grain boundary between grains 1 and grain 4 near the triple point with grain 2.

4.7. Examination of grains along the crack path

An OIM scan of the crack path was performed on the arrested crack sample and is shown in figure 4.17. As observed, different shades of color can be seen within each grain due to EBSP software's inability to resolve the small c/a ratio. The corresponding BSE image of the crack path is shown in figure 4.18. The grain orientations closest to the crack path were determined using the technique of combining EBSP with SACP or the Schmid factor values with plane trace analysis. These results are shown in Appendix A. The grain orientations (grain normal and the stage tilt axis directions) are tabulated in Table 4.1.

Schmid factors for twinning and ordinary dislocation activity were determined for each grain. For example, a BSE image of the interaction between grains B and C is

shown in figure 4.19. The crack path is to the right of both grains, propagating downwards in the direction indicated in the image. The plane traces analysis and its corresponding Schmid factors were superimposed over each grain. In grain B, two dominant sets of twins were observed (one evenly distributed throughout the grain and the second was more active near the crack path). These two sets of twins correspond well with (-111) and (1-11) plane traces, which have with similarly high Schmid factors of 0.38.

The grain boundary between grains B and C was intact and there is some degree of correlation between the observed heavily twinned vertical (-111) planes in grain B and both (111) and (-111) twinning systems in grain C. In grain C, however, it is difficult to relate the observed twin traces with the low Schmid factors (including negative values). The changes in localized stress states as the crack propagated may have accounted for the activity of some of the twinning systems, or, these twins may have been pre-existing (e.g. twins on (111) and 1-11) planes.

There is a remarkable degree of correlation between the vertical (-111) twins in grain B and concentrated slip or twins on (-111) planes in grain C. The Luster and Morris parameter (table 4.2) showed that there is a strong degree of slip compatibility between (-111) twins in grain B and (-111) twins in grain C (m'=0.35) and (-111) ordinary dislocations in grain C (m'=0.65). But the interpretation of slip in grain C is also complicated by the annealing twin boundary in grain C near grain B.

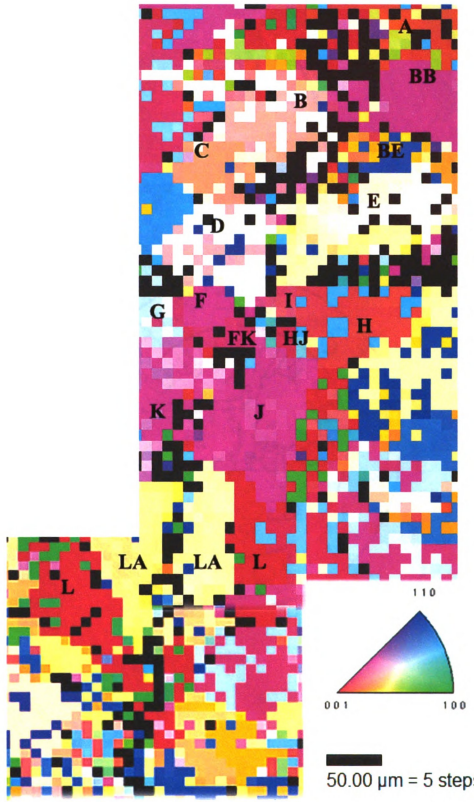

Figure 4.17 Orientation image mapping (OIM) image of crack path, shown in a normal direction inverse pole figure map.

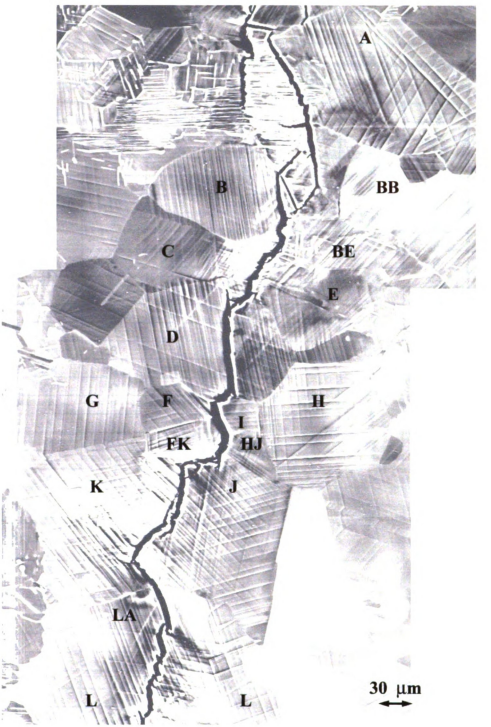

Figure 4.18. Composite BSE image of the crack with the notch on the top and the crack tip located towards the bottom of the image. The grains that are close to the crack path are labeled as shown.

Table 4.1: Grain Orientations

Grain	h	k	l	*u*	*v*	*w*
A	1	3	6	-15	1	3
B	8	3	-10	-3	8	0
BB	11	10	-13	8	-1	6
BE	6	4	1	4	-7	4
C	100	26	-75	53	84	100
D	9	11	3	-1	0	3
E	6	16	-17	17	0	6
F	10	11	16	9	-14	4
FK	1	1	-3	15	-9	2
G	9	3	-4	-1	15	9
H	3	7	15	-11	-6	5
HJ	31	25	-99	100	40	41
I	32	59	-99	50	25	31
J	7	8	10	2	-3	1
K	7	10	6	-4	1	3
L	3	2	-21	4	15	2
LA	6	6	-1	-2	3	6
ZW	0	2	3	1	-12	8
Z	7	20	-17	100	0	41
1	1	5	6	3	-3	2
2	61	0	100	-99	92	60
3	13	5	4	2	-14	11
4	1	12	-10	4	3	4
5	4	13	-12	3	0	1
5A	13	20	0	-99	65	16
6	9	1	20	-8	12	3
7	9	11	0	-11	9	13
8	8	1	6	-8	10	9
9	8	10	1	-4	3	2
9twin	10	2	11	-3	4	2
10a	10	1	7	-5	8	6
10b	1	3	0	-25	5	-2
11	7	2	-15	5	-10	1
12	9	2	8	-4	-10	7
13	6	1	-9	6	9	5
14	3	2	11	-19	1	5
15	4	7	-8	-3	4	2
16	4	1	-6	10	14	9
17	6	1	4	-8	12	9
18	4	1	-6	9	12	8
21	49	100	-48	100	-9	80
21a	12	1	19	-1	12	0

Table 4.1: Cont'd

Grain	h	K	l	*u*	*v*	*w*
22	70	40	-41	0	1	1
23	81	17	100	-25	100	4
23a	5	6	1	-8	5	10
31	8	12	5	-4	1	4
32	2	3	-18	9	0	1
33	5	3	-3	3	11	16
33a	15	7	8	0	-4	3
33b	1	2	-7	-1	4	1
33c	10	9	14	-4	6	-1
35	41	90	-40	1	0	1
36	29	100	0	-99	29	8
37	100	15	68	-48	100	49
49a	11	15	1	6	-5	9
49b	11	1	-9	3	3	4

In figure 4.20 the interaction between grains I, H and HJ is shown. The path of the crack is to the left of these grains. Both grains I and HJ show large amounts of deformation twinning in the grains. There was a moderate amount of twin deformation in grain H. Plane trace analysis and corresponding Schmid factors were superimposed on each grain. A higher magnification BSE image of highlighted area A is shown in figure 4.21. Microcracks were observed along the grain boundary between adjacent grains HJ and H as indicated by the arrows. Images of other grain boundary interactions with and without microcracks are provided in figure 4.22 and in Appendix 2.

Figure 4.22 shows a BSE image of grains L and LA with a portion of the OIM map (see figure 4.17) inserted on the left bottom corner to facilitate identifying the grain boundary between these two grains. The primary crack propagating through grain LA alternates between cleavage and jogging to a nearby intragranular microcrack, changing its path several times. Two microcracks are evident at the grain boundary region between grain L and LA as shown within the highlighted circle. These grain boundary

microcracks are identified by the sharp protrusion and are usually at an angle to the crack path.

The presence of grain boundary cracking or the lack of it between adjacent grains can thus be systematically investigated and will be described in the next chapter.

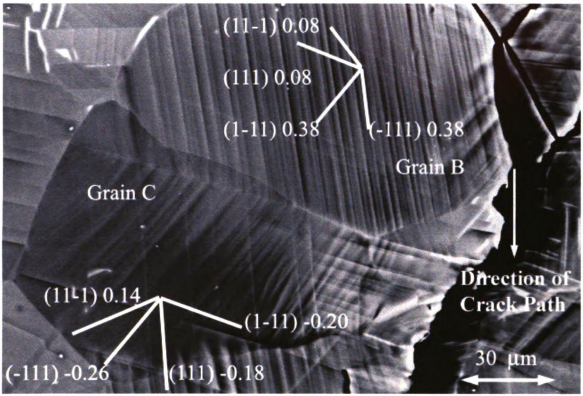

Figure 4.19. BSE image of grains B and C with the plane traces and corresponding Schmid factors superimposed on the grains.

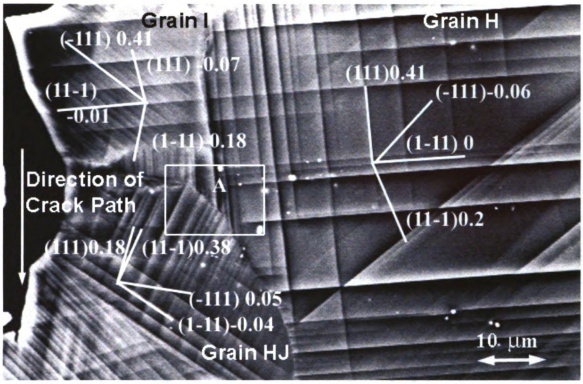

Figure 4.20. BSE image of grains H, I, and HJ with the plane traces and corresponding Schmid factors superimposed on the grains. Higher Magnification BSE image of highlighted area A is shown in Figure 21.

Table 4.2: Luster and Morris Slip Compatibility Factors for grain B and C.

Schmid Factor			-0.18	-0.14	***-0.26***	**0.37**	-0.2	0.2	0.14	0.02
	Plane	**grain C**	(111)	(111)	***(-111)***	***(-111)***	(1-11)	(1-11)	(11-1)	(11-1)
	grain B	**Direction**	1/6[11-2]	1/2[1-10]	***1/6[-11-2]***	***1/2[110]***	1/6[1-1-2]	1/2[110]	1/6[-1-1-2]	1/2[1-10]
0.08	(111)	1/6[11-2]	0.34	0.09	-0.07	-0.27	0.5	0.87	**-0.04**	0.07
-0.31	(111)	1/2[1-10]	0.1	0.21	-0.08	0.16	0.85	-0.51	0.25	0.15
0.38	***(-111)***	***1/6[-11-2]***	0.36	-0.3	***0.35***	**0.65**	-0.05	0.28	-0.18	-0.28
0.31	***(-111)***	1/2[110]	0.08	0.46	-0.5	0.43	0.09	0.19	-0.27	0.44
0.38	(1-11)	1/6[1-1-2]	-0.69	-0.06	-0.41	-0.15	0.32	0.1	0.36	0.05
-0.31	(1-11)	1/2[110]	-0.1	-0.59	0.36	-0.31	0.11	0.22	-0.28	0.46
0.08	(11-1)	1/6[-1-1-2]	-0.39	0.38	0.51	0.12	-0.05	-0.06	0.36	-0.56
0.31	(11-1)	1/2[1-10]	-0.15	-0.29	0.14	-0.27	-0.23	0.14	0.69	0.43

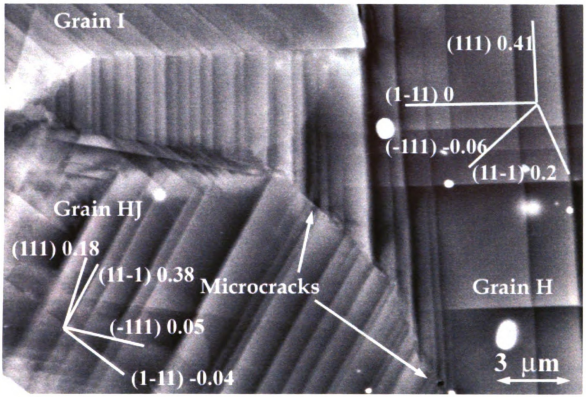

Figure 4.21. Higher magnification of the highlighted region marked A in figure 4.20 showed microcracks along the grain boundary between grains H and HJ.

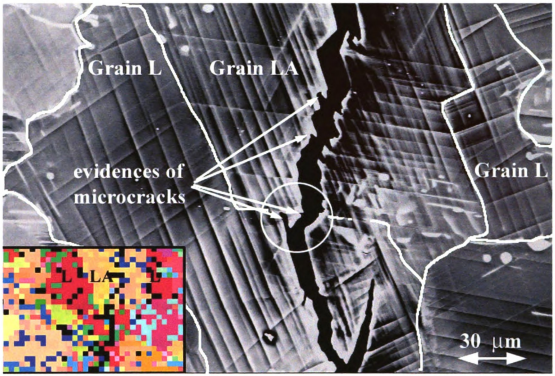

Figure 4.22. BSE image of grains L and LA with a portion of the OIM map (see figure 4.17) inserted. Primary crack changes its path several times as it cleaves within grain LA. Microcracks are evident within grain LA (arrows) and at the grain boundary region between grain L and LA as shown within the highlighted circle.

Chapter 5: Analysis of Arrested Crack

5.1 Overview

Luster and Morris (LM) geometric compatibility factor was used to provide some insight into the slip transfer between grains along the initial crack path but the LM numeric values were not wholly satisfactory in identifying or predicting the microcracks at the grain boundaries. A fracture propagation parameter was developed to address this problem (identify boundaries that are prone to microcracking).

5.2. Crack path and microcrack nucleation

The composite backscattered electron (BSE) image of the crack path (shown in figure 4.6) that varies between transgranular to intergranular is consistent with observation of mixed mode failure noted by other researchers [59,60]. The extensive twin and dislocation generation observed ahead of the crack tip suggests that even though the crack propagated mostly by cleavage, it generated plastic deformation ahead of the crack tip. With sufficient plastic deformation in a grain ahead of the crack, the crack tip blunted and stalled as shown figures 4.5 and 4.7. At the same time, microcracks nucleated at the nearby grain boundary between grains 1 and 2 in figure 4.7 (arrows indicate the region of interest) that indicates in a change in the crack path from transgranular to intergranular. The nucleation/formation of microcracks ahead of the crack tip is analyzed and discussed in more detail in sections 5.3-5.

5.3. Compatibility Factor for Active Twin Systems

With the ability to determine each grain orientation, plane traces can be easily identified for deformed grains and the interactions between the adjacent grains can be analyzed using the Luster and Morris compatibility factors. As the general state of stress is known, it is possible to estimate the Schmid factors for the observed deformation systems. Schmid factors were calculated based on the principal tensile stress direction, and are only approximate since the actual stress condition changed as the crack grew. The Schmid factors, along with the compatibility factors m' between active twin systems in grains 1 and 2, are shown in Table 5.1 *in italics*. Negative compatibility factors imply that twinning on one system requires anti-twinning on the other, which is not probable, while positive factors indicate various degrees of twin compatibility, ranging up to a value of 1 for full compatibility.

As shown in table 5.1, the (-111) twinning planes in grain 1 have the highest Schmid factor (0.42) and this is consistent with the large numbers of twins observed in grain 1 (see figure 4.5). Traces of (11-1) and (1-11) twins are also observed in this grain, fewer due to their lower Schmid factors. Figures 4.5 and 4.6 show that microcracks are correlated with these active twin systems.

In grain 2, (figure 4.5) the most heavily twinned system was found to be (-111) although the Schmid factor is –0.23, the lowest of the 4 {111} twin systems in the grain. The reasons for this are not entirely clear. It is possible that the tensile loading direction changed as the crack grew. Traces of the other twin systems are evident but to a lesser amounts.

Table 5.1 shows that the highest value of m' = 0.46 occurs for twin systems that have negative Schmid factors. This illustrates how a high m' value with low Schmid factors does not necessarily mean that compatible slip transfer occurred.

The heavily twinned (-111) planes in grain 1 have poor geometric compatibility with the (111) planes in grain 2 (m'=0.14), which also has a negative Schmid factor (-0.11). However, in figure 4.6 there appears to be some correlation between these two deformation systems even though the geometric compatibility is low. The (11-1) traces in grain 2 that have the highest twinning Schmid factor (0.21) and a negative compatibility factor (-0.54) were not observed close to the boundary with grain 1. There was better compatibility between the grain 1 dominant (-111) twinning system and ordinary dislocation slip systems (including highly stressed (001)[110]) having high Schmid factors in grain 2, with compatibility factors > 0.5.

The large number of twins observed in grain 1 relieved the large stress fields ahead of the crack tip in grain 1. The deformation twin strain can either be dissipated into other grains by strain accommodation at the grain boundaries via generation of dislocations or twins in the adjacent grain, or stresses will accumulate at the grain boundaries. If these stresses accumulate at the grain boundary, it may then result in microcrack nucleation. Although there is twin activation in grain 2, there is weak indication of twin to twin strain transfer from grain 1 to grain 2 (figure 4.6). This appears to be consistent with the significant numbers of microcracks opened up in direct correlation to the most distinct (-111) twins in grain 1 (arrows in figure 4.6). However, slip activation in grain 2 correlated with the dominant twins in grain 1 appears to be more likely, on (-111) and (1-11) planes.

Table 5.1: Schmid factor and the geometric compatibilty factor m' between active slip and twin systems in grains 1 and 2 (refer to figure 4.5 and 4.6)

Schmid Factor		**grain 2**	**-0.11**	0.15	**-0.22**	-0.37	**-0.15**	0.18	**0.23**	0.04	-0.1	0.48
	Slip Plane		(111)	(111)	(-111)	(-111)	(1-11)	(1-11)	(11-1)	(11-1)	(001)	(001)
grain 1		**Direction**	1/6[11-2]	1/2[1-10]	1/6[-11-2]	1/2[110]	1/6[1-1-2]	1/2[110]	1/6[-1-1-2	1/2[1-10]	1/2[1-10]	1/2[110]
-0.09	(111)	1/6[11-2]	*-0.31*	0.23	**0.46**	0.52	*-0.01*	-0.44	*-0.04*	-0.29	-0.05	0.06
-0.22	(111)	1/2[1-10]	-0.22	-0.07	0.46	-0.27	-0.5	0.23	0.51	0.09	-0.02	0.03
0.43	(-111)	1/6[-11-2]	*0.14*	-0.03	*-0.08*	**0.66**	***-0.1***	**0.44**	*-0.54*	-0.07	-0.09	**0.94**
0	(-111)	1/2[110]	0.04	-0.37	0.47	-0.04	-0.19	-0.02	0.12	-0.74	0.95	0.06
0.16	(1-11)	1/6[1-1-2]	*-0.98*	-0.1	*-0.25*	-0.22	*-0.14*	-0.11	*0.14*	0.04	-0.06	-0.28
0	(1-11)	1/2[110]	-0.1	0.97	-0.28	0.02	0.08	0.01	0.06	-0.38	0.52	0.03
-0.09	(11-1)	1/6[-1-1-2	*-0.12*	-0.11	*0.06*	-0.35	*0.43*	0.67	*-0.16*	0.35	0.2	0.28
0.22	(11-1)	1/2[1-10]	-0.1	-0.03	-0.28	0.17	0.72	-0.32	0.59	0.1	0.06	-0.14
0.39	(001)	1/2[1-10]	-0.28	0.09	0.15	0.09	0.18	-0.08	0.94	0.17	0.07	-0.15
0	(001)	1/2[110]	-0.05	-0.53	0.16	0.01	-0.09	-0.01	0.17	-0.96	-0.38	-0.02

*** Values discussed in the text are in bold**

Comptability factor m' between active twin systems are shown in *italics

In short, the Luster and Morris parameter offers some insight on the role of slip transfer, but not on microcrack formation, as microcracks developed in a boundary where twin to ordinary slip transfer occurred. Also the Luster-Morris parameter it is not wholly satisfactory, because it is clear that the magnitude of the Schmid factor is also important.

5.4 Microcrack formation

The microcracking between grains 1 and 2 can be directly correlated with the geometry of the primary twinning system in grain 1. The shear developed by twinning on the (-111) plane in the [-11-2] direction resulted in a local tensile stress on one side of the twins where grain boundary microcracks nucleated. Figure 5.1 shows a projected image of the (-111) twinning plane as it is tilted within the crystal. The (-111) plane is represented by vectors for [110] ordinary dislocations (dashed line) and [011] and [10-1] superdislocations (solid lines). The plane normal has a component out of the page and the projection of the [-11-2] twining direction bisects the 'triangle' and is perpendicular to the [110] ordinary dislocation direction. When this image is superimposed on grain 1, (Figure 5.2), the direction of the twinning Burgers vector is to the left and into the grain boundary.

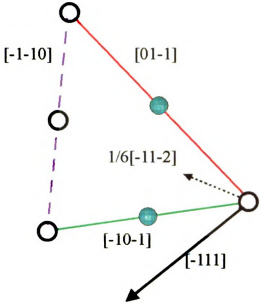

Figure 5.1. The computed projection of the (-111) plane based upon the known crystal orientation of grain 1 (normal direction [1,5,6], and the horizontal tensile direction (stage rotation axis), [3, -3,2]), shows superdislocation directions, (solid lines), the ordinary dislocation direction (dashed) and the plane normal (bold arrow) that has a component pointing out of the page. The [-11-2] twinning direction bisects the triangle and is projected into the page.

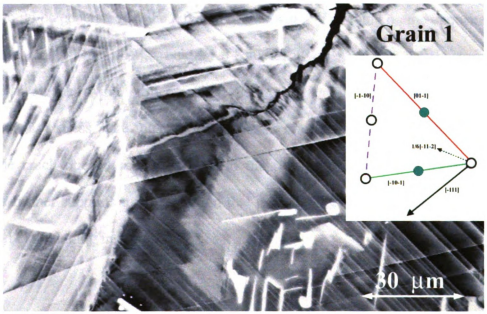

Figure 5.2. The projection of the (-111) twin plane superimposed on grain 1 provides a means to visualize how twinning vector (bisects the triangle) moves towards the left and into the page.

With the direction of the twinning vector defined, it is possible to explain the asymmetric opening of the microcracks in relation to the twins. Figure 5.3 shows a crack opening with the twinning plane from grain 1 perpendicular to the page. The projection of this corresponding (-111) twin plane is inserted above and left of the image while the projection of the (111) twin plane from grain 2 (which has the highest geometric compatibility factor of 0.14) is inserted above and right of the BSE image. The twinning vector [-11-2] from grain 1 is projected into the page and upwards whereas the twinning vector [11-2] from grain 2 is projected out of the page and to the left. A schematic thin twin (-111) in grain 1 is shown in figure 5.4a. As the twin grew, the resulting twin vector [-11-2] is projected upwards and into the paper on the left side of the twin. For a thin twin, the adjacent grain could easily accommodate this small amount of shear elastically. However, for a thicker twin, the shear at the boundary (see figure 5.4b) and the inability of the adjacent grain to accommodate the larger amount of shear, a local compressive stress would be generated on the left side of the twin . (Twinning on the opposite side of this plane, i.e. (1-1-1) [1-12], would have equivalently resulted in a tensile stress on the right side of the twin). Superposing the global tensile stress state on the local twin/boundary stress state intensifies the tensile effects on the right side of the twin. Thus the crack opened asymmetrically to the right of the twins, as observed. This analysis further supports the observation that microcracks form as a direct consequence of the (-111) twinning in grain 1.

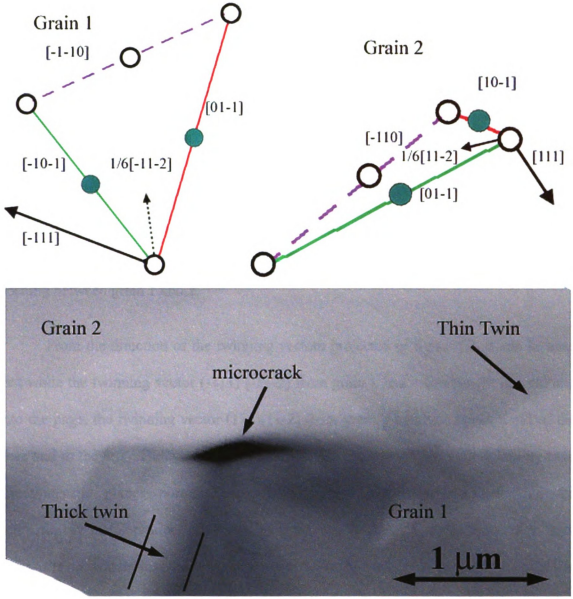

Figure 5.3. BSE image of a crack opening. Projections of the corresponding twin planes are shown on the top of the BSE image. Solid arrows have component out of page while the dotted arrow has a component going into the page.

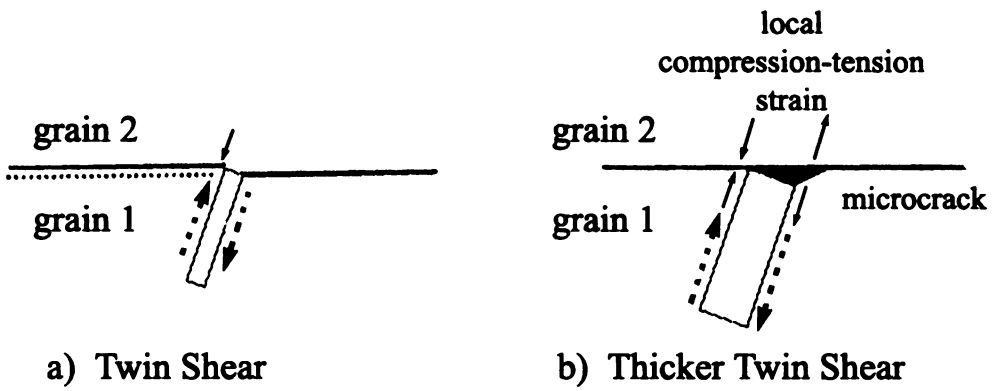

Figure 5.4. a) Thin twin shear. b) Thicker twin shear causes a local compression-tension strain. This strain resulted in a local tension opening force and hence, a microcrack opening between grain 1 and 2.

From the direction of the twinning vectors projected in figure 5.3, it can be seen that while the twinning vector (-111) [-11-2] from grain 1 had a component upward and into the page, the twinning vector (111)[11-2] from grain 2 had a component out of the page and to the left. Though the two vectors appear to have negative compatibility twin direction, the planes normals also have a negative compatibility, making the compatibility factor product positive. With the two twinning systems opposed to each other, it is no wonder that the strain was not completely transferred across from grain 1 to grain 2 by twinning.

5.5 Subsequent Re-Loading

When the specimen was re-loaded in 4-point bending after the characterization described above, surface ledges developed along some of the (-111) twins in grain 1 (Figure 4.14). These features appear to be largest at or near the grain boundary and diminish in the direction toward the center of the grain.

The twin contrast also appears strongest at the grain boundary and often disappears toward the grain interior (see-highlighted region in figure 4.14(b) that is magnified in figure 4.15. This suggests that the twins were activated at the boundary between grains 1 and 2 and propagated into grain 1, but only some of the twins propagated across the entire grain (Figure 4.5). This history implies that the operative twinning system in grain 1 was the compliment to the one used in characterizing, i.e. instead of a (-111) [-11-2] twinning system, it is more likely that the (1-1-1)[1-12] twinning system operated, which moved mass away from the boundary on the side that the crack opened up. Microcracks also nucleated along the grain boundary between grains 1 and 4 during re-loading of the specimen, as shown in Figure 4.17. As noted in Table 5.2, the heavily twinned (-111) planes in grain 1 have very poor geometric compatibility with any of the twin systems in grain 4, with the highest factor m' of 0.06 between a/6[-11-2](-111) twins of grain 1 and a/6[11-2](111) twins of grain 4. With such low compatibility between twinning systems between these two grains, it is not surprising that the boundary cracked. Furthermore, only the most dominant twinning (11-1) system in grain 4 interior has a positive, but moderate, Schmid factor. The (111)a/6[11-2] and (-111)a/6[-11-2] twin systems that interact with the grain boundary cracks, have negative Schmid factors implying a more complex local state of stress, were operating, or that most of the twins were preexisting.

Interestingly, the Luster and Morris geometric compatibility factor showed that the heavily twinned (-111) planes in grain 1 have a good geometric compatibility with the (1-11)[110] ordinary dislocation in grain 4, having a high m' value of 0.85. But even

with that high m' value, microcracks were observed along the grain boundary between grain 1 and grain 4.

As shown in figures 4.3, and 4.5, plastic deformation readily occurs near the crack tip by available slip and twinning systems, but the ability to dissipate this deformation to neighboring grains is hampered by the need for effective accommodation of concentrated twin shear at the grain boundaries with neighboring grains. Table 5.2 shows that there are no high compatibility values for twin transfer, though several slip systems have high compatibility with the dominant (-111)[-11-2] twins in grain 1.

Luster and Morris examined the relationship between deformation systems across γ-TiAl grain boundaries using a geometric compatibility factor m'. Based on this assumption, it would be reasonable to use this factor m' to serve as a microcrack predictor or indicator, low m' for microcrack possibility and high m' for no microcrack formation or intact boundaries. But judging from the two sets of grain boundary interactions for grain boundaries 1-2 and 1-4, it is not entirely clear that the Luster-Morris parameter can unambiguously predict conditions for microcracking. The high value of m' (0.85) between the dominant twin in grain 1 and the most highly stressed ordinary dislocation system (1-11) [110] in grain 4, provides some indication that slip transfer occurred across the boundary, but this does not explain the occurrence of microcracks at these boundaries.

The ability to predict microcrack formation may be the key to understanding toughness or the lack of it, in a material. Thus a new parametric approach is needed to predict this microcrack formation.

Table 5.2: Schmid factor and the geometric compatibilty factor m' between active slip and twin systems in grains 1 and 4 (refer to figure 4.5)

Schmid Factor		**grain 4**	-0.07	-0.11	-0.15	-0.2	-0.2	0.35	0.27	-0.03	0.07	0.48	0.09	-0.09
	Slip Plane		(111)	(111)	(-111)	(-111)	(1-11)	(1-11)	(11-1)	(11-1)	(001)	(001)	(1-10)	(-110)
grain 1		**Direction**	1/6[11-2]	1/2[1-10]	1/6[-11-2]	1/2[110]	1/6[1-1-2]	1/2[110]	1/6[-1-1-2	1/2[1-10]	1/2[1-10]	1/2[110]	1/2[110]	1/2[-110]
-0.09	111	1/6[11-2]	*0.06*	0.27	*0.05*	0.08	*-0.32*	0.1	*-0.47*	-0.88	-0.52	0.15	0.01	-0.7
-0.22	111	1/2[1-10]	-0.08	0.15	0.25	-0.16	0.12	-0.21	0.88	-0.47	0.28	0.32	0.03	0.38
0.43	-111	1/6[-11-2]	***0.06***	-0.13	*0.04*	-0.28	*-0.51*	**0.85**	*-0.24*	-0.1	-0.2	**0.48**	**0.7**	0.02
0	-111	1/2[110]	-0.33	-0.17	0.11	0.17	-0.85	-0.51	-0.09	-0.14	0.26	0.3	0.42	-0.03
0.16	1-11	1/6[1-1-2]	*-0.47*	0.88	*-0.31*	-0.09	*0.05*	-0.07	*0.07*	-0.31	0.5	-0.13	0.01	-0.73
0	1-11	1/2[110]	0.88	0.47	0.12	0.19	0.24	0.15	-0.1	-0.16	0.26	0.29	-0.02	-0.38
-0.09	11-1	1/6[-1-1-2	*-0.26*	0.11	*-0.54*	-0.84	*0.05*	0.27	*0.05*	0.12	0.21	-0.5	0.67	0.02
0.22	11-1	1/2[1-10]	-0.08	0.15	-0.84	0.54	0.1	-0.18	-0.32	0.17	0.28	0.32	-0.44	0.02
0.39	(001)	1/2[1-10]	-0.14	-0.26	-0.52	-0.33	0.18	-0.34	**0.48**	-0.26	0	0	-0.41	-0.31
0	(001)	1/2[110]	0.48	-0.25	0.21	-0.32	-0.53	-0.32	-0.16	-0.25	0	0	-0.39	-0.3
0	(1-10)	1/2[110]	0.75	-0.38	0	0	0.67	0.41	-0.02	-0.02	0.32	0.36	0.25	-0.25
0	(-110]	1/2[-110]	0	0.01	-0.66	-0.43	-0.01	0.02	-0.74	0.4	0.34	0.39	-0.25	0.25

*** Values discussed in the text are in bold**

Comptability factor m' between active twin systems are shown in *italics

5.6 Examination of microcracks along various grain boundaries

Grain boundaries between two adjacent grains along the path of the crack were examined for possible microcrack nucleation. In areas slightly away from the crack path, it is easy to spot the microcracks along the grain boundaries. On the other hand, it is n7t possible to see microcracks if they grew to become part of the primary crack. In such cases, it is important to observe 'tell tale' signs. These 'tell tale' signs include sharp protrusion of the microcracks at an angle with respect to the direction of the crack path as shown in figure 4.22. It is common to see microcracks lying at an angle to the primary crack along a grain boundary. In other cases, the slight change in the path of the primary crack suggests that it had probably passed through grain boundary microcracks that grew and eventually joined up similar to that observed in Figure 4.14b.

5.7 Fracture Propagation Parameter

A total of 39-grain boundaries surrounding the primary crack were analyzed to allow the development of a fracture propagation parameter analogous to Simkin's fracture initiation parameter (see section 2.7). In this study, the role of twinning as a deformation accommodation mechanism in grain B due to twinning deformation in grain A was examined (noting that the lack of compatible twinning may correlate with microcracking). This requires consideration of directionality of twin to twin deformation transfer that was not considered by Simkin, since deformation transfer by twinning requires that the *absolute* direction of the twinning shear be not opposed to twinning in the neighboring grain (as depicted in figure 5.5). Directionality is also relevant to the process of crack propagation, because a crack approaching grain A before grain B will

cause more deformation in grain A than B (see figure 5.6). Thus, slip transfer is more important from grain A to B than B to A.

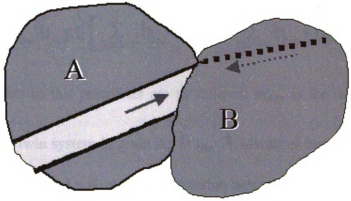

Figure 5.5. Slip transfer by twinning requires that the absolute direction of the twinning shear be not opposed in a twin system in the neighboring grain.

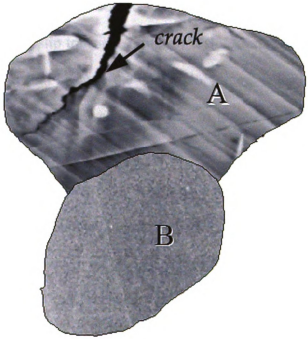

Figure 5.6. Directionality is important in evaluating the deformation of grains in the path of the crack. A crack approaching grain A before grain B will cause more deformation in grain A then in grain B.

An adaptation of Simkin's fracture initiation parameter that takes directionality into account can be expressed as

$$F_{A\leftarrow B} = m_{Atw}|\hat{b}_{Atw}\bullet\hat{t}|\left[\sum_{Bord=1}^{2}|\hat{b}_{Atw}\bullet\hat{b}_{Bord}| + \sum_{Btw=1}^{4}\hat{b}_{Atw}\bullet\hat{b}_{Btw}|_{if>0}\right]$$

The three parts of this parameter are as follows: m_{Atw} is the maximum Schmid factor for a reference twin system in grain A; $\hat{b}_{Atw}\cdot\hat{t}$ identifies how well the reference twin Burgers vector is aligned with the tensile traction unit vector $\hat{t}$ (for simplicity, in the direction of tensile loading); the two sums of the dot products in large square brackets describe how well the Burgers vector of this most highly stressed twin system in grain A is aligned with the Burgers vectors for ordinary dislocations and/or twins in grain B, indicating the possibility of slip transfer. Ordinary dislocations and the twins in grain A are not considered in the sum because the dot product terms will always contribute the same values to the sum. Absolute values are used to identify interactions that are slip based, where either slip direction is equally probable. The second sum recognizes the directionality of twin shear (Figure 5.5). It is also possible to relax the directionality requirement but such attempts resulted in poor statistics as shown in Appendix 4.

Ideally, if two grains have a highly compatible pair of twin orientations, then one of the twin system in grain Y will be more closely aligned with the burgers vector for twins in grain Y'. For example, grain Y with orientation (7,20, -17)[100,0,41] and grain Y' with orientation (7,20, -9)[100,0,78] are misoriented by 20.2° but there is an 8° difference between (-111) plane normals). One of the twin system, (-111)[-11-2], in grain Y is closely aligned with the burgers vector for twins (-111)[-11-2] in grain Y' than the other twinning or dislocations systems (see Table 5.3) with m' =0.93. The same twin

system (-111)[-11-2] in grain Y however, may not be as closely aligned with the other three sets of slip systems in grain Y'. But this slip compatibility with only the most highly stressed twinning system in grain Y' is sufficient to allow twin-based slip transfer across that leaves only some residual strain in the grain boundary. Note that all of the other Luster-Morris parameters have low values, making the overall sum rather low, too. Taking into account the summation of all the interaction of the twin slip in grain Y with the ordinary dislocations and the twin system in the adjacent grain (grain Y'), the Fracture Propagation Parameter computation indicated a low $F_{A\to B}$ value of **0**.59.

On the other hand, if the twin system (1-11)[1-1-2] in grain K is not aligned with any of the four twin system in grain J (see Table 5.4), then there will be more residual strain left on the grain boundary, creating a highly stressed boundary that is more likely to result in microcracks. The Fracture Propagation Parameter would have a much higher value (1.31), due to many more combinations of slip systems that have modest values of the Luster-Morris parameter.

With this fracture propagation parameter established, two sets of the fracture propagation parameter values (abbreviated as $F_{A\to B}$ values) were computed for each set of grain boundary interactions in Table 5.5. There are two sets of $F_{A\to B}$ values simply because of the directionality of the interaction between grain X to grain Y or grain Y to grain X. If the direction of the crack is moving from grain X to grain Y, then the value of x-y is used. But if both grain X and grain Y are lying side-by-side, then the maximum value is selected. The final selection of the $F_{A\to B}$ value for each grain boundary interaction and its corresponding observation of cracked (denoted as 1) or intact (denoted as 0) grain boundary is shown on the far right hand column.

Table5.3: Schmid factor and the geometric compatibility factor m' between active slip and twin systems in grains Y and Y' (idealized case with misalignment of ~ 8 degrees).

Schmid Factor			-0.15		0.07		-0.16		0.08	
	Plane	grain Y'	(111)	(111)	(-111)	(-111)	(1-11)	(1-11)	(11-1)	(11-1)
	grain Y	Direction	1/6[11-2]	1/2[1-10]	1/6[-11-2]	1/2[110]	1/6[1-1-2]	1/2[110]	1/6[-1-1-2	1/2[1-10]
0.05	(111)	1/6[11-2]	0.89	-0.04	0.29	0.47	0.17	0.3	0	0
	(111)	1/2[1-10]	0.01	0.93	-0.36	0.06	0.19	0.04	0	0.01
0.21	(-111)	1/6[-11-2]	0.05	-0.03	0.93	0.2	-0.14	-0.08	0.28	-0.27
	(-111)	1/2[110]	0.02	-0.01	-0.19	0.91	0.13	-0.36	-0.42	-0.06
0.04	(1-11)	1/6[1-1-2]	0.21	0.16	-0.07	-0.09	0.93	0.33	0.18	0.26
	(1-11)	1/2[110]	0.07	-0.03	0.05	-0.26	-0.33	0.93	-0.35	-0.05
0.21	(11-1)	1/6[-1-1-2	-0.39	-0.06	0.08	-0.03	0.19	-0.06	0.89	0.1
	(11-1)	1/2[1-10]	0	-0.6	-0.07	0.01	0.12	0.03	-0.11	0.93

Table5.4: Schmid factor and the geometric compatibility factor m' between active slip and twin systems in grains K and J.

Schmid Factor			0		0.46		0.29		-0.03	
	Plane	**Grain J**	(111)	(111)	(-111)	(-111)	(1-11)	(1-11)	(11-1)	(11-1)
	Grain K	**Direction**	1/6[11-2]	1/2[1-10]	1/6[-11-2]	1/2[110]	1/6[1-1-2]	1/2[110]	1/6[-1-1-2	1/2[1-10]
0	(111)	1/6[11-2]	-0.41	-0.91	0.07	-0.06	-0.27	-0.07	0.07	0.35
	(111)	1/2[1-10]	0.91	-0.41	0.25	0.15	0.13	0.16	-0.13	0.15
-0.09	(-111)	1/6[-11-2]	-0.28	-0.13	0.03	0.21	-0.56	-0.81	0.05	-0.15
	(-111)	1/2[110]	-0.07	-0.18	0.06	-0.15	-0.82	0.57	-0.33	-0.2
0.19	(1-11)	1/6[1-1-2]	0.06	-0.24	-0.38	0.11	0.03	0.07	-0.51	0.85
	(1-11)	1/2[110]	-0.06	-0.15	0.1	-0.26	0.22	-0.15	0.85	0.51
-0.17	(11-1)	1/6[-1-1-2	0.07	0.12	-0.49	0.86	0.05	-0.34	-0.18	0.07
	(11-1)	1/2[1-10]	-0.34	0.15	-0.86	-0.5	0.16	0.2	-0.08	0.09

Population means from these two sets of $F_{A\to B}$ values can be easily calculated. To compare the population means of these two distribution to see if they are significantly different, the student t–test was used.

In a typical t-test, using a null hypothesis that the population means are equal, the t-statistics, which involves the difference of the two sample means, was computed to see how extreme it (t-statistic) is. If the t statistic is unusually large, which says that the difference of means is great compared to its estimated standard deviation, then the difference is statistically significant.

The t-test analysis can be easily performed using the Data Analysis Tools found in Microsoft Excel and the results are shown in Table 5.6

The t-test analysis showed that the sample mean and the standard deviation for the intact boundary are 0.73 and 0.31 respectively while those of the cracked boundary is 1.23 and 0.15 respectively. Assuming a null hypothesis that the two sample means are statistically equivalent, there is a 99% chance that t critical (for two-tail) will fall within +/- 2.99. From the analysis, t-statistic was computed to be +/-5.47, a value that is much larger than the t-critical value. This suggests that the difference of means is great and is statistically significant. There is a 99% confidence that the cracked population, μ_{ABc}, exceeded the intact population mean, μ_{ABi}, with individual confidence intervals (based on the mean and +/- standard deviation) for μ_{ABc} and μ_{ABi} of (1.07, 1.38) and (0.42, 1.03), respectively.

Figure 5.7 shows a histogram of both the intact and cracked $F_{A\to B}$ values. It is clear that microcracking is unlikely when $F_{A\to B} < 1.0$, but is more likely when $F_{A\to B} > 1.0$. Thus, this parameter may be used to predict a path for crack propagation (i.e., grain

boundaries with $F_{A\to B} > 1.0$ are prone to fracture while boundaries with lower values resist cracking).

As shown in figure 5.7, there were a number of intact values with high $F_{A\to B}$ values. These adjacent grains were re-examined to seek possible reasons for the lack of boundary cracking. Table 5.7 lists grain boundaries with high $F_{A\to B}$ values that were intact. The reasons for having intact boundaries while having a high $F_{A\to B}$ values are listed on the right hand column of the table.

In grains BE and E (see appendix 2-Figure A2-2) the grain boundary was almost at 90 degrees to the path of the crack. The net tensile stress on this boundary is small since the boundary is parallel to the stress axis.

There was only a small boundary length between grains L and J, compared to their overall grain sizes and as such this boundary may have been insignificant. This boundary was also further away from the crack (see appendix 2-Figure A2-10).

For the other grain boundaries, it was observed that there were higher $F_{a\to b}$ values near the regions of interest and the crack had continued to move towards those boundaries with higher high $F_{a\to b}$ values instead. (See appendix 2- Figure A2-5).

The Luster-Morris compatibility factors provide information on the slip compatibility between two adjacent grains but the numeral value thus obtained does not provide a convincing way to describe the effectiveness of the deformation transfer across the neighboring grain or prediction of microcracking at the grain boundaries. The newly developed fracture propagation parameter, on the other hand, will be evaluated to determine if it can predict intact or cracked boundaries. Knowledge about these intact or

cracked boundaries will lead to understanding how effective the deformation transfer had been in these grains.

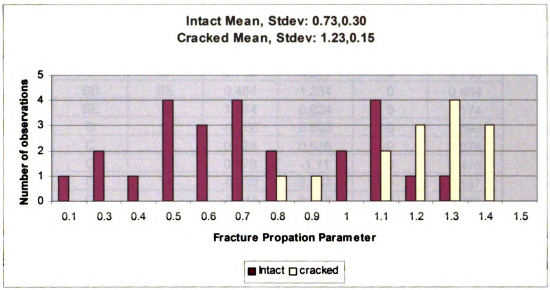

Figure 5.7. Histogram of intact and cracked boundaries using $F_{a\to b}$ values.

Table 5.5: Values of the Fracture Propagation Parameters assigned to each set of grains, depending on the direction of the crack path as it moves into these grain boundaries. The selected F value is displayed on the far right hand side.

Grain X	Grain Y	F_{A-B} (x - y)	F_{A-B} (y - x)	Intact=0, crack=1	Selected F value
A	BB	0.407	0.349	0	0.407
B	C	0.755	0.517	0	0.755
BB	BE	0.464	1.234	0	0.464
BE	E	1.174	0.624	0	1.174
D	E	-0.766	0.593	0	0.593
C	E	0.528	0.576	0	0.576
C	D	0.476	-1.11	0	0.476
D	H	-0.832	0.137	0	0.137
D	F	-0.915	0.312	0	0.312
H	J	1.26	1.468	0	1.26
G	F	0.347	1.09	0	1.09
F	FK	0.983	0.88	0	0.983
FK	K	0.986	0.42	0	0.986
H	HJ	1.066	-0.067	0	1.066
HJ	J	1.084	0.8532	0	1.084
K	LA	0.712	-0.398	0	0.712
J	L	1.09	0.941	0	1.09
K	L	0.44	0.709	0	0.709
L	LA	0.699	-0.315	0	0.699
ZW	Z	0.41	0.468	0	0.468
5	Z	0.72	0.53	0	0.72
5	5B	0.44	0.6	0	0.6
ZW	6	0.47	1.234	0	0.47
5	2	0.847	0.77	0	0.847
Z	6	0.32	0.765	0	0.32
BB	B	0.4364	0.841	1	0.841
D	I	-0.82	1.309	1	1.309
H	I	1.29	1.31	1	1.31
F	I	1.42	1.43	1	1.43
I	FK	1.28	1.02	1	1.28
HJ	FK	1.399	1.12	1	1.399
FK	J	0.93	1.08	1	1.08
K	J	0.632	1.311	1	1.311
J	LA	1.153	-0.35	1	1.153
5	5A	0.72	1.19	1	1.19
5	1	0.35	0.87	1	0.87
5A	1	1.13	1.011	1	1.13
1	2	1.15	0.668	1	1.15
1	4	1.38	0.895	1	1.38

Table 5.6: t-test analysis for the intact and cracked boundary (precracked).

t-Test: Two-Sample		
	Intact	*Cracked*
Mean	0.73	1.23
Standard deviation	0.30	0.15
Variance	0.093	0.024
Observations	24	13
Pooled Variance	0.069	
Hypothesized Mean Difference	0	
df	35	
t Stat	-5.47	
P(T<=t) one-tail	1.90E-06	
t Critical one-tail	2.72	
P(T<=t) two-tail	3.81E-06	
t Critical two-tail	2.99	

Table 5.7: Intact Grain Boundaries with high $F_{A\to B}$ values

Grain X	***Grain Y***	$F_{A\to B}$ **Values**	**Comment**
D	H	1.278	Boundary with higher F value nearby
BE	E	1.174	Grain boundary || stress direction
G	F	1.09	Boundary with higher F value nearby
J	L	1.09	Short grain boundary length, far from crack
HJ	J	1.084	Boundary with higher F value nearby
H	HJ	1.066	Boundary with higher F value nearby

Chapter 6: Results of Microcrack Extension

6.1 Overview

In this section the Fracture Propagation Parameter was evaluated near the crack tip to allow prediction of the path of the crack. This sample (A) was subsequently loaded to induce further cracking and the predicted path and the actual path were compared. This Fracture Propagation Parameter was also applied to another sample (B) to see if it was able to account for the way the crack had propagated.

6.2 Sample A

The undamaged microstructure below the primary crack was analyzed and the grains labeled numerically as shown in figure 6.1. Figure 6.2 shows a schematic representation of the grain boundaries in this region with the $F_{A\to B}$ values indicated. Black arrows were inserted to denote the likelihood of fracture for deformation increasing in the direction of the arrows across the boundaries whereas gray arrows indicate otherwise. Grain boundaries highlighted with thick black lines denote boundaries with directional F values > 1, i.e. weak boundaries. A higher magnification of the boxed region is shown in figure 6.3. From identification of weak boundaries the crack can be predicted to follow the path highlighted in red as shown in figure 6.4.

Figure 6.1. The undamaged microstructure below the primary crack was analyzed for grain orientations, and the grains were labeled numerically.

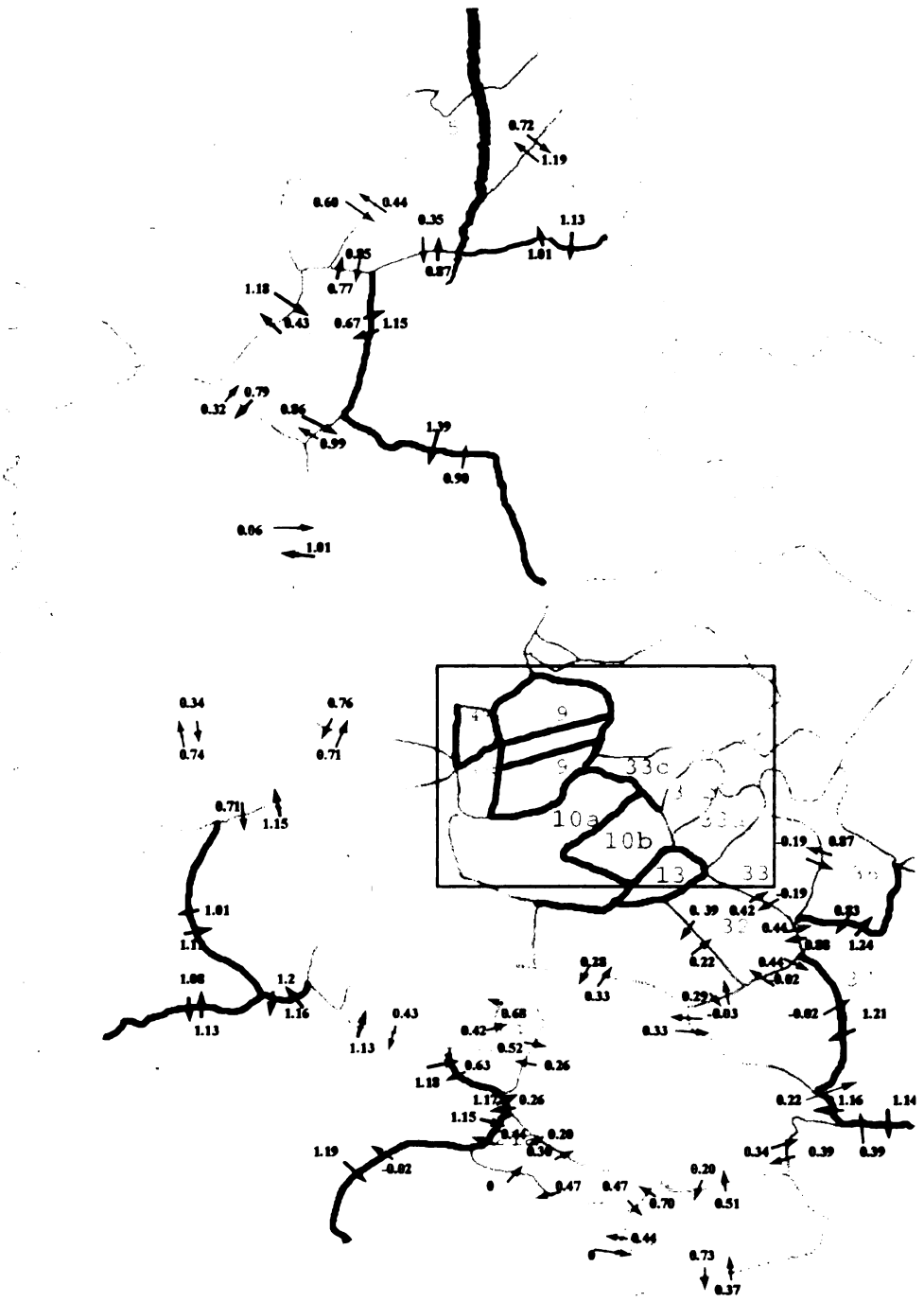

Figure 6.2. Schematic diagram shows the $F_{A \to B}$ values, the directional arrows (black or gray), and the weak boundaries highlighted in thick black color.

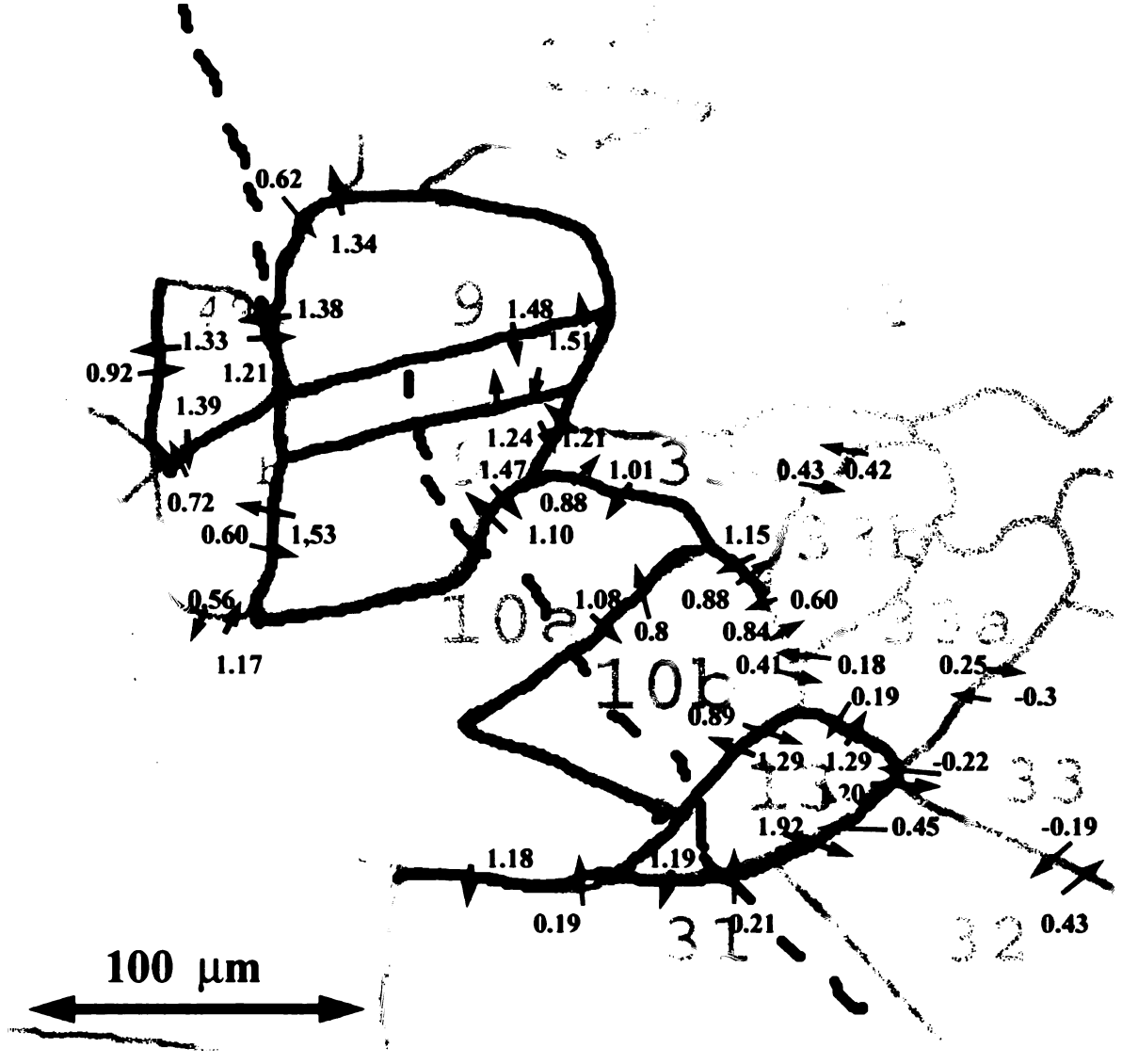

Figure 6.3. Higher magnification of the boxed region shown in figure 6.2. The fracture propagation parameters are computed for each grain boundary and the weak boundaries are identified with thick black lines.

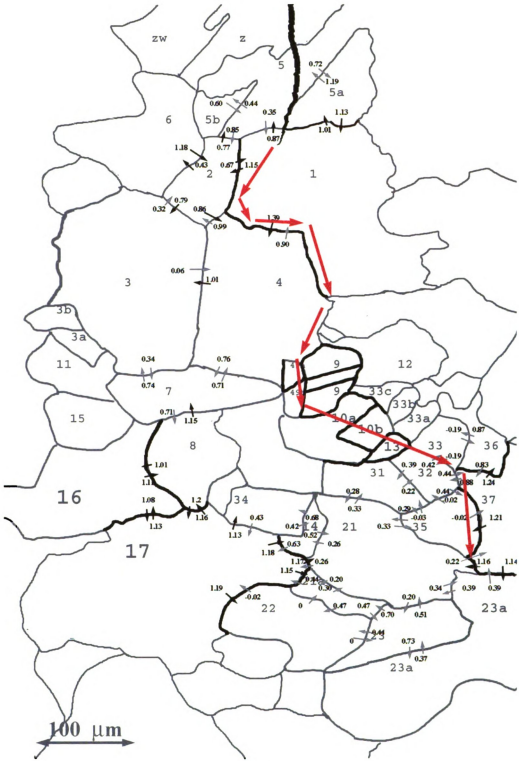

Figure 6.4. Based on the observed weak boundaries, crack path was predicted to move in the direction as shown in red.

When the specimen was deformed further, the microcracks that formed along the 1-2 grain boundary as well as the 1-4 grain boundary linked up. Other microcracks were generated farther down the 1-4 grain boundary, as shown in figure 6.5. With continued deformation, the crack changed direction (see figure 6.6) to follow along the 1-4 grain boundary until a jog in the boundary (see figure 6.7) caused the crack to extend by cleavage through grain 4. A cluster of Ti_3Al had diverted the propagating crack downwards into the grain 4.

Figure 6.8 shows the primary crack moving towards a group of weak boundaries around grain 9, (figures 6.2 - 6.4). Grain 9 had a pre-existing annealing twin bisecting the whole grain as shown in figure 6.9, as well as some pre-existing deformation twins. New microcracks (arrowed) were observed ahead of the crack path. These cracks occurred at the grain boundaries between 7-49a, 9-49a, and 49a-49b boundaries. As the specimen continued to be stressed, microcracks continued to form as highlighted in black arrows in figure 6.10 and higher magnification images of these grain boundaries where the cracks formed are shown in figures 6.11 through 6.14.

Figure 6.1 shows the path of the crack as the specimen was stressed in the 4-point bend fixture. The primary crack continued its path via cleavage in grain 4 towards grain 9, jogged just below but parallel to the annealing twin within grain 9 and continued to cleave via grain 10a and grain 10b towards grain 13 (a grain similar to grain 9, having weak boundaries and an annealing twin within). The primary crack was arrested in grain 31 as shown in the figure while a new crack initiated in the neighboring grain 32 and continued down towards another cluster of weak boundaries at the junction of grains 21-

35-37-23a. The grain boundary between 31 and 32 has very low $F_{A \to B}$ values (figure 6.2).

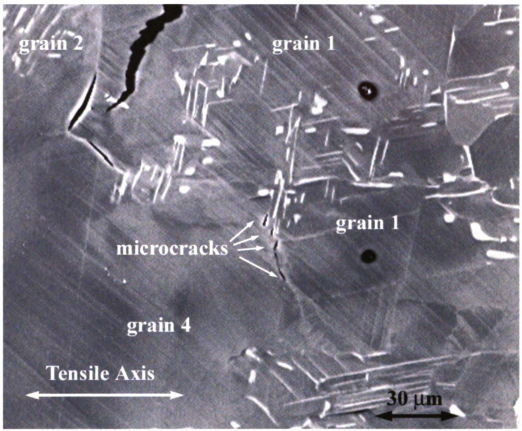

Figure 6.5. When the sample was further loaded, the microcracks along 1-2 boundary as well as 1-4 boundary linked up. Microcracks were also observed farther down the 1-4 grain boundary.

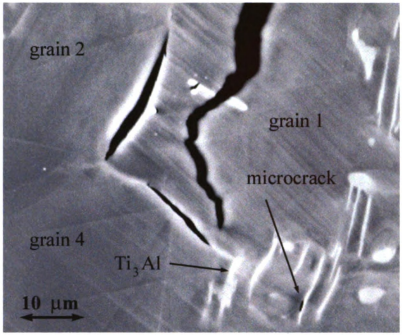

Figure 6.6. The crack path changed direction from the 1-2 boundary towards the 1-4 boundary.

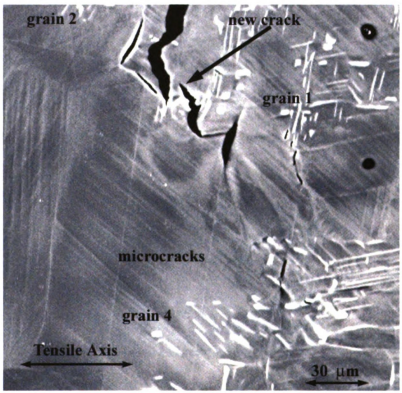

Figure 6.7. The crack was arrested near some Ti3Al particles at the 1-4 grain boundary while a new crack had resurface further along the 1-4 boundary and cleaved into grain 4.

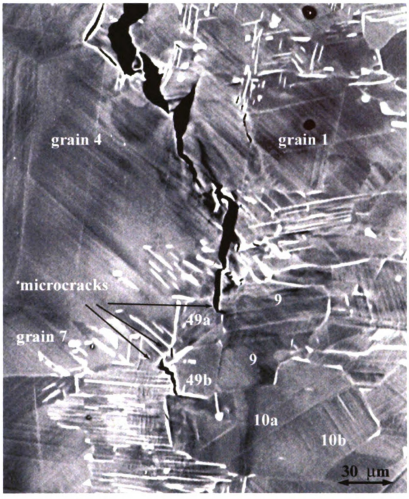

Figure 6.8. The crack extended towards a group of weak boundaries around grain 9.

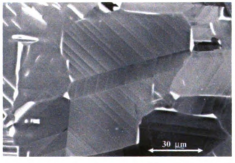

Figure 6.9. Pre-existing twins in undeformed grain 9 include the annealing twin that divides grain 9 into two smaller grains.

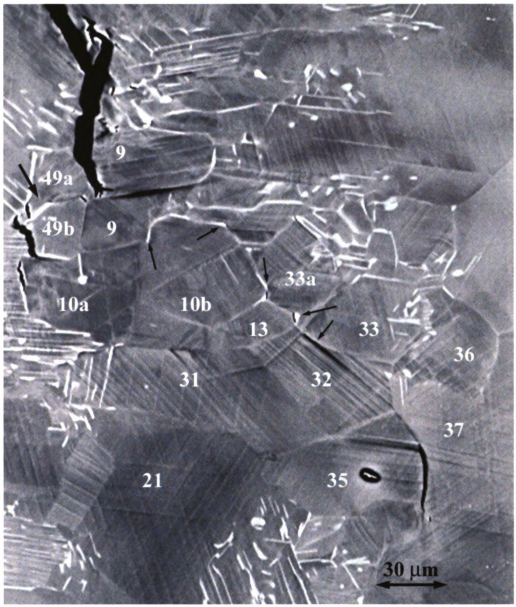

Figure 6.10. Microcracks developed as the crack was further loaded. Arrows indicate the locations of fine microcracks. Higher magnification images of these microcracks are shown in figures 6.10 through 6.13.

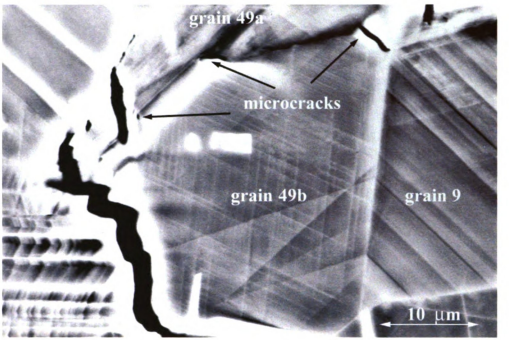

Figure 6.11. Microcracks (arrowed) along the 49a-49b grain boundary. On the left of grain 49b is a platelet of Ti3Al.

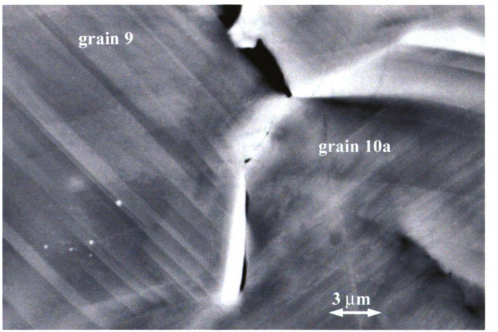

Figure 6.12. Microcracks developed along grain boundary between grain 9 and grain 10a. The microcrack developed in a Ti_3Al grain boundary precipitate.

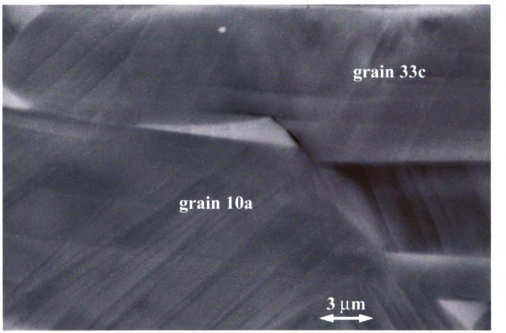

Figure 6.13. Microcrack occurred between the grain boundary bordering grain 10a and grain 33c when the specimen was further loaded. The microcrack developed in a Ti_3Al grain boundary precipitate.

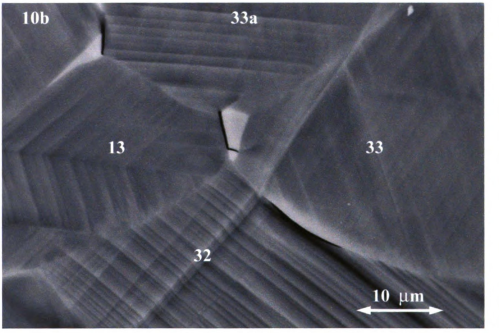

Figure 6.14. Microcracks formed along the grain boundary Ti_3Al between grain 10b and 33a, grain 13 and grain 33a, grain 13 and grain 33 as well as between grain 32 and grain 33 when the specimen was further stressed via 4-point bending.

Even though microcracks nucleated in some of the weak boundaries ahead of the crack tip, the crack did not divert directly towards these cracks, similar to the microcracks in grains 1-2, and 1-4. Instead, the crack continued towards the next cluster of weaker boundaries. Microcracks were observed in weak boundaries between grains 49a-49b, 10a-13, 13-33a, 10a-31, 31-35, and 35-37, and many of these boundaries had Ti_3Al precipitates.

Although the crack did not directly follow weak boundaries, perhaps due to the influence of grains beneath the surface, the surface microcracks had a disproportionately strong effect on the crack path.

Figure 6.16 shows a histogram of both intact and cracked boundaries for the lower portion of the crack path. It is again clear that microcracking is less likely when $F_{A\to B} <$ 1.0 but is more likely when $F_{A\to B} > 1.0$.

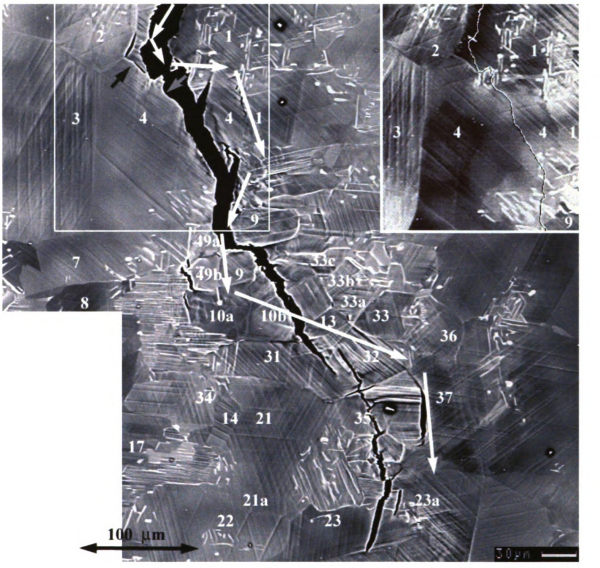

Figure 6.15. Path of the propagated crack with predicted path (white arrows) superimposed over it. The black arrow indicates the grain boundary cracking in the 1-4 boundary and the grey arrow shows where the crack deviated by cleavage of grain 4 towards the weak boundaries in grain 9. Insert shows an image of the region before the crack propagated through grain 4.

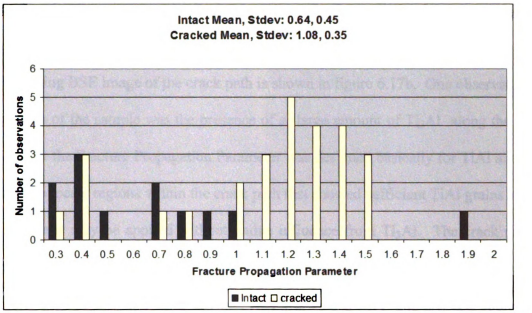

Figure 6.16. Histogram of intact and cracked boundaries of the lower portion of the crack path.

6.3 Sample B

Sample B, from the same casting and with similar geometry, but a different orientation, (see figure 3.1) was loaded in 4-point bending but the crack propagated through the whole sample. As with sample A, sample B also had mixed mode cracking[1]. Figure 6.17 shows an SE image and its corresponding BSE (at higher magnification) image of sample B. Because the crack had propagated through the specimen, it resulted in a large crack opening displacement. Obtaining meaningful information near these widely opened crack edges were more difficult since backscattered electrons escape via these crack edges as the beam is rastered near to these edges [61]. A region nearer to the crack tip region (where the opening of the crack was smaller) was thus examined and an OIM scan was performed. This region (boxed) is shown in figure 6.18a.

[1] The extensometer and the load cell used with the E. Fullam deformation stage was not working properly and thus did not register the extension or the load when the crack propagated through the notch.

The OIM scan of the boxed region is shown in figure 6.17a. Different colors are present within each grain due to the inability of EBSP to resolve the small c/a ratio. The corresponding BSE image of the crack path is shown in figure 6.17b. One observation on this portion of the sample was the presence of a large amount of Ti_3Al along the crack path. Since the Fracture Propagation Parameter was designed basically for TiAl alloys, it is crucial to locate regions within the crack path that showed sufficient TiAl grains so that this parameter may be applied without undue influence from Ti_3Al. The crack path in this sample could then be analyzed to see if the concept of this fracture propagation parameter (i.e., intact boundaries having low $F_{A\to B}$ values (<1) and cracked boundaries having high $F_{A\to B}$ values (>1)) could work with a differently oriented sample using the same specimen geometry.

A portion of the cracked region (away from the high density Ti_3Al region was thus located and analyzed (see figure 6.17b). The crack cleaved through grain D5 before terminating in grain D4, but a new crack had initiated at the grain boundaries between D4-D1 and D1-D3 regions and moved downwards through the D4-D3 grain boundary.

Using the Fracture Propagation Parameter, this microstructural patch was labeled with the directional arrows corresponding to the $F_{A\to B}$ values as shown in figure 6.18. The weak boundaries were also identified and highlighted in black bold lines. Similar to the previous sample (A), it was observed that the crack in this region of the sample ran through regions of weak boundaries or jumped from one region/cluster of weak boundaries to another weak cluster of boundaries. Given that the orientation of the specimen with respect to the texture is different, the fracture propagation parameter appears to be a robust predictor of crack propagation.

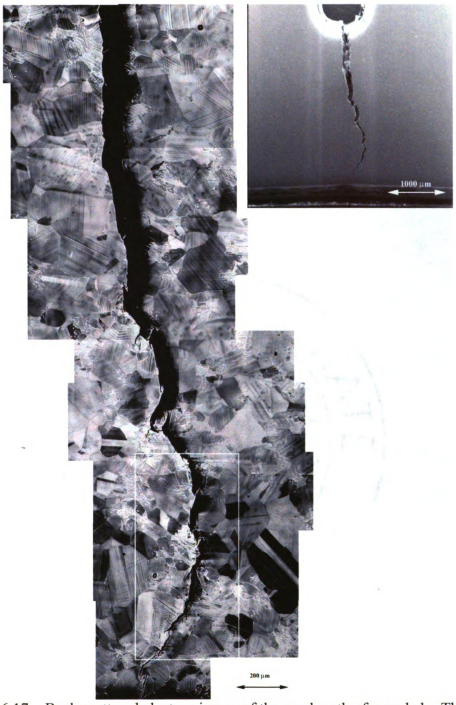

Figure 6.17. Back scattered electron image of the crack path of sample b. The SE image is on the right top corner. The crack propagated completely through the sample. The boxed region was analyzed and is shown in figure 6.18.

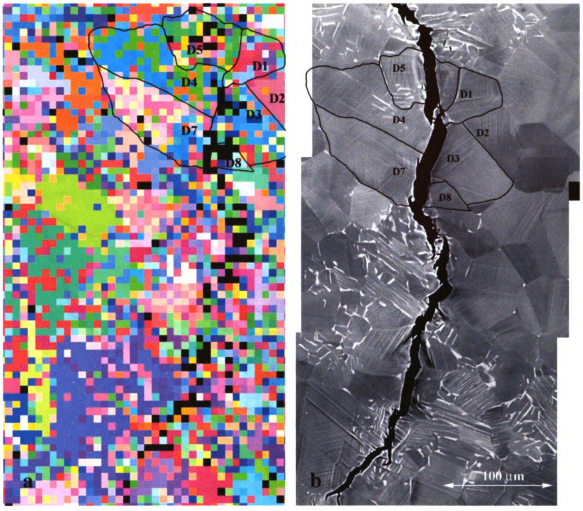

Figure 6.18. a) OIM image of the crack path. b) Corresponding BSE image. A large amount of Ti_3Al was observed along the crack path. A small cluster of grains were labeled and analyzed using the fracture propagation parameter.

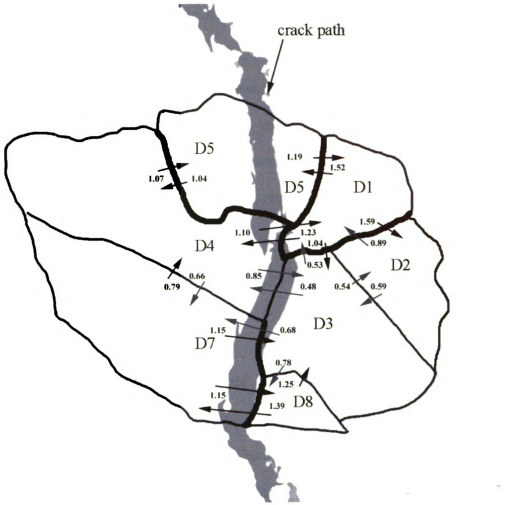

Figure 6.19. Schematic diagram of the area of interest shows the $F_{A \to B}$ values, the directional arrows (black or gray), and the weak boundaries highlighted in thick black color.

Chapter 7: Discussion

7.1 Overview

A fracture propagation parameter was used to explain the observed crack path for two samples with different orientations with respect to the casting (Samples A and B). Boundaries with fracture propagation parameter > 1 were identified as weak boundaries and the primary crack had a tendency to propagate towards clusters of weak boundaries. Where it is not possible to follow a boundary directly, the crack cleaved through a grain, via the shortest distance towards the next cluster of weak boundaries.

7.2 Sample A

Further deformation of sample A showed that the crack deviated from the 1-2 grain boundary towards the 1-4 grain boundary direction where microcracks had also formed with the additional loading. The crack did not follow the 2-4 boundary that was aligned with the growing crack because the fracture propagation parameter between grains 2 and 4 was $F_{2\_4} = 0.99$ and whereas was $F_{1\_4} = 1.39$. Though the F_{2_4} value is ~1, the weaker boundary between grains 2 and 4 provided a lower energy path for the crack despite the fact that this boundary was nearly parallel to the maximum tensile direction. In other words, the boundary between grains 1 and 4 is weaker than the boundary between 2 and 4 and hence was easier to fracture. The crack sought weak boundaries in preference to boundaries with high tensile stress acting on them, and thus, followed a path that connected weak boundaries (high F_{A_B} values).

The advancing crack shown in figure 6.5 was diverted towards the 1-4 grain boundary. This crack was subsequently arrested as it approached some clusters of α_2

(Ti_3Al) alloy particles as shown in figure 6.6. The presence of these $\alpha 2$ particles has previously been found to have some effect on the TiAl[1] [8,62]. It was also observed that sometimes cracks formed in the interface between γ and α_2 for reasons that are probably similar to the reasons that are being sought for the boundaries in the γ phase, but this is beyond the scope of this project.

With continued loading, a new crack surfaced slightly further along the 1-4 grain boundary (see figure 6.7) but since it is not possible for cracks to move parallel to the tensile loading direction indefinitely, the crack extended by cleavage through grain 4, perhaps triggered by the microcrack adjacent to Ti_3Al. The crack by-passed the microcracks that had formed along the 1-4 boundary, (see figure 6.5) in the process. The cleavage crack grew downward towards the next nearest cluster of weak boundaries surrounding grain 9. The crack took the "shorter route" towards the next cluster of weak boundaries surrounding grain 9.

The annealing twin interfaces within grain 9 (see figure 6.8) have high F_{A_B} values, and although the boundary was not highly stressed in Mode I, the boundary fractured parallel to the stress axis along the lower twin boundary (see figure 6.15), and then fractured by cleavage toward the grain boundary between grains 9 and 10a that has a high F_{9_10} value =1.47. The crack path is clearly heading towards the next cluster of weak boundaries, which surround grain 13. The boundaries along grain 13 are apparently very weak, showing F_{A_B} values as high as 1.92.

[1] It has been argued that the α_2 phase scavenges interstitial impurities from the γ phase, thereby lowering its oxygen content, causing an increase in ductility in the γ phase

The crack subsequently moved transgranularly into grain 31 and was arrested. Grain 31 had strong boundaries with all of its neighboring grains. But a new crack initiated in the neighboring grain 32 and continued down the path towards another cluster of weak boundaries at the junction of grain 21-35-37-23a. The cause for this discontinuity in the path may be due to the fact that the boundary between grains 31 and 32 was strong. It is interesting to note that even though a large microcrack had grown in the 35-37 grain boundary (see figure 6.9), the crack did not divert towards that weak boundary but continued its path downwards, cleaving transgranularly into grain 35. It subsequently stalled at the grain boundary between grain 23 and grain 23a; grain 23a was heavily twinned similar to grain 1, where the crack was stalled earlier.

The observation of microcracks between grains 49a-9, 49a-7, 49a-49b, 9-10a, 10a-33c, 10b-33a, 13-33, 32-33 (see figure 6.9–6.13) ahead of the advancing primary cracks corresponded very well with high F_{A_B} values. The only exception was the observation of a single tear along the boundary between grains 32 and 33, which had a low F_{A_B} value of 0.43 (Figure 6.14). Even though microcracks nucleated in some of the weak boundaries ahead of the crack tip, the crack did not divert directly towards these microcracks (similar to the microcracks in the 1-2 and 1-4 grain boundaries) but rather, it continued towards the next cluster of weaker boundaries.

The F_{A_B} values for both the intact and cracked boundaries beyond the original crack were further analyzed using the student t-test and the results are shown in Table 7.1. Again, assuming a null hypothesis that the two sample means are equal, there is a 99% chance that t critical (for two-tail) would fall within +/- 2.98. From the analysis, t-statistic was computed to be +/-3.347, a value that is larger than the t-critical value. This

suggests that the difference of two sample population means is great and is statistically significant. The mean value of $F_{A\rightarrow B}$ for the cracked population, μ_{ABc}, exceeded the intact population mean, μ_{ABi}, with 99% confidence that $\mu_{ABc} > \mu_{ABi}$, with individual confidence intervals for μ_{ABc} and μ_{ABi} of (0.73, 1.44) and (0.18, 1.09), respectively.

Table 7.1 t-test analyses for the intact and cracked boundaries (post cracked).

t-Test: Two-Sample : intact and cracked boundaries		
	Intact	*Cracked*
Mean	0.64	1.08
Standard deviation	0.45	0.35
Variance	0.20	0.12
Observations	12	27
Hypothesized Mean Difference	0	
df	37	
t Stat	-3.35	
t Critical one-tail	2.71	
t Critical two-tail	2.98	

Based on the analyzed data, (grain orientation, dot product of the interaction between the highly stressed twinning vector with the ordinary dislocations and twins from the adjacent grain) and the observed microcracks, high F_{A_B} values between two adjacent grains, would most likely result in the creation of microcracks along the grain boundaries. The crack, however, did not exactly follow boundaries that had microcracks.

Instead, it tended to cleave within a grain in order to connect regions having clusters of weak boundaries. Hence, the path of a crack in a γ-TiAl alloy could be predicted by noting the locations of weak boundaries.

There were four cracked boundaries with low values. In figure 6.13 Ti3Al had precipitated along the boundary. The microcrack formed between the Ti_3Al/TiAl interface in grain 33c. This microcrack may have developed due to the strain incompatibility between these two phases since there are fewer facile slip systems in the Ti3Al compared to TiAl.[63])]. This microcrack is close to another microcrack formed nearby (in the 32-33 grain boundary) (see figure 6.14). The low $F_{A\text{-}B}$ value indicates a strong boundary (32-33), suggesting that the microcracks observed in these two sets of boundaries might have been connected below the surface.

Two cracked boundaries that were almost parallel to the tensile loading direction with low $F_{A\text{-}B}$ values (31-35, 32-35, Figure 6.2) opened up as the crack propagated perpendicular to these boundaries. This also suggests that the crack may have been connected below the surface,

7.3 Sample B

The concept that a primary crack, in a γ–TiAl alloy will propagates via regions of high F_{A_B} values or weak boundaries has been demonstrated using sample A. To determine if this hypothesis will work with any gamma-TiAl alloy with similar specimen geometry and loading conditions, sample B was tested, which had texture differences perpendicular to the loading axis.

In this sample, the primary crack ran almost entirely through the width of the specimen. This might have been due to poor bonding of the epoxy resin, but there was no evidence of delamination between the TiAl and the aluminum backing. Thus, assuming that the aluminum or bond did not account for the greater initial stored energy prior to cracking, the elastic analysis based upon the texture is considered next.

As shown in figure 4.1, the x-ray analysis revealed that sample A and sample B were oriented differently in terms of their orientation with respect to the notch root. Both specimens have the same texture/properties along the primary tensile axis (TA). Figure 7.1 shows how elastic modulus and highly stressed slip and twinning systems are related to crystal orientation. The effect of dominant crystal orientation on properties in the notch direction is summarized in Table 7.2. This indicates that the greater amount of strain energy release in Sample B (longer crack propagation) can be understood in terms of elastic and plastic deformation processes that depend on texture.

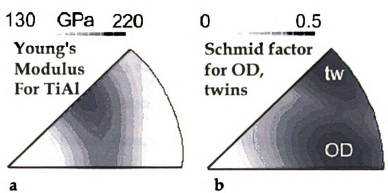

Figure 7.1. Relationship between texture and deformation processes in the direction of the notch root are examined in Table 7.2 by considering maxima for Young's modulus and Schmid factor maxima for twins and ordinary dislocations.

Table 7.2: Effect of dominant crystal orientation on deformation along notch root.

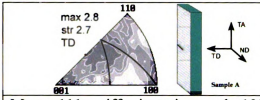	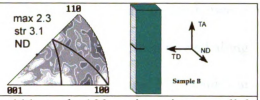
More <111> stiff orientations and <100> compliant orientation parallel to notch root.	Less <111> and <100> orientations parallel to notch root.
Heterogeneous elastic strains resulted from the different sets of orientations.	More homogenous elastic strains since there are no distinct set of orientations.
Have fewer orientations that have high Schmid factors for twins and ordinary dislocations.	More orientations with high Schmid factors for twins and ordinary dislocations, i.e. a high Schmid factor indicates that the deformation system is able to operate to carry the strain.
Due to differences in orientations (stiff and compliant), there is modest plastic deformation in the notch root with minimal shape change.	Due to the more homogeneous orientations and higher Schmid factors for twins and ordinary dislocations, there are substantial plastic deformations in the notch root resulting in shape change.
With modest plastic deformation, local stresses are built up at the grain boundaries and fracture stress is reach with elastic strain.	With substantial plastic deformation, the material is also worked hardened, thereby increasing its stored strain energy.
When fracture stress is reached, there is less stored strain energy released with the fracture.	When fracture stress is reached, there is a huge amount of stored strain energy released with the fracture.

An OIM scan was performed on a region closer to the crack tip since the width (gap) of the crack at that region was smaller and ECCI/EBSP analysis was possible. As shown in figure 6.17b, the presence of Ti_3Al particles complicated the analysis of grain orientation and plane traces. Thus, only regions with fewer Ti_3Al particles were selected and analyzed.

The fracture propagation parameter can explain the behavior of this portion of the crack path easily. Using the same concept of weak boundaries for high F_{A_B} values (>1), it was observed that sample B followed similar fracture trends as sample A, i.e. the crack propagated via weak boundaries or connected via weak boundaries.

The primary crack (shown in figure 6.16) cleaved through grain D5 and was arrested in grain D4. But a new crack had surfaced along the boundary region between grain D1 and D4. This region had a high F_{A_B} value of 1.23. The crack then moved along the grain boundary and connected with boundaries with the next highest F_{A_B} values at the boundary region between D7 and D3 (F_{A_B} values = 1.15). From there, the crack moved on to grain D7 and D8 which had a F_{A_B} values of 1.39. Within this small region, it was observed that the crack continued to move in a way consistent with the observed crack path in sample A, that is, the crack sought out and linked the weakest boundaries as it propagated.

The student t-test was performed on this small population to see if the difference between sample means for both the intact and crack population were statistically significant. Again assuming a null hypothesis that the two population means were the same, the analysis (Table 7.3) showed a 95% chance that the t critical (for two-tail) would fall within +/- 2.84. From the analysis, t-statistic was computed to be +/-2.85, a value that is slightly larger than the t-critical value. Hence the difference of two sample population means is statistically significant, despite the smaller population of misorientations. The mean value of $F_{A\rightarrow B}$ for the cracked population, μ_{ABc}, exceeded the intact population mean, μ_{ABi}, with 95% confidence that $\mu_{ABc} > \mu_{ABi}$, with individual confidence intervals for μ_{ABc} and μ_{ABi} of (1.05, 1.34) and (0.60, 1.07), respectively. However this analysis is based upon a much smaller population of datum points.

Table 7.3: t-test analyses for intact and cracked population means (Sample B)

t-Test: Two-Sample :intact and cracked boundaries		
	Intact	*Cracked*
Mean	0.83	1.20
Standard deviation	0.23	0.15
Variance	0.05	0.02
Observations	5	4
Hypothesized Mean Difference	0	
df	7	
t Stat	-2.85	
t Critical one-tail	2.36	
t Critical two-tail	2.84	

7.4 Evaluating the Fracture Propagation Parameter for Other Samples

Development of the fracture propagation parameter was based on examination of the surface of the crack induced as result of a 4-point bend loading as shown in figure 7.2a. To see if this fracture propagation parameter can be applied to a similar material but with different loading geometry (see figure 7.2b), grain information from Simkin's thesis/experiment was used to generate the $F_{A\rightarrow B}$ values. Simkin's studies involved bending a smooth bar of the same γ-TiAl alloy (see figure 7.2b) and examining the tensioned surface for microcracks along the grain boundaries. With Simkin's 4-point loading condition, it can be assumed that all the grains on the tensile surface were stretched similarly at the same time. Consequently, the selection of the $F_{A\rightarrow B}$ values between two adjacent grains were based on the larger of the two values (because there was no reason to choose one grain as a reference grain without an existing crack), similar

to Simkin's selection criteria. The $F_{A\to B}$ values and Simkin's F values, together with the condition of the boundaries (either cracked or intact) were tabulated as shown in Table 7.4. Both parameters showed similarly high $F_{A\to B}$ values for cracked boundaries but intact boundaries showed otherwise a variety of values. While the fracture initiation parameter used by Simkin produced generally low F values, ranging from 0.59 to 1.11, the analysis using the fracture propagation parameter showed a wider range of $F_{A\to B}$ values, ranging from 0.57 to 1.32.

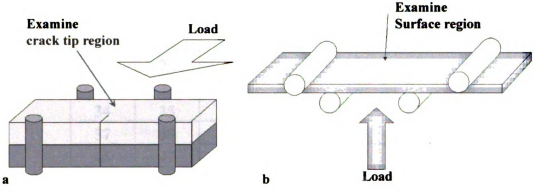

Figure 7.2. Examination of specimen surfaces. a) Ng's specimen b)Simkin's specimen.

The t-tests for both methods are shown in Tables 7.5 and Table 7.6. While there is a significant difference between the values of the cracked and intact boundaries using Simkin's Fracture Initiation Parameter (see Table 7.5, where the t Stat value of -3.24 is outside the t Critical value of +/-2.44), the t-test for the values of the cracked and intact values using the Fracture Propagation Parameter in Table 7.6 showed otherwise. The sample mean and its standard deviation for the cracked boundaries were 1.08 and 0.30 respectively. These values are comparable with sample A. So the fracture propagation parameter is fairly accurate in describing conditions where microcracks form. But the

sample mean and its standard deviation for the intact boundaries were 0.95 and 0.26 respectively. This value is slightly higher than the data set from sample A.

Table 7.4: Simkin's dataset using both the Fracture Propagation Parameter and Fracture Initiation Parameter.

Grain	Grain	Propagation Parameter	Initiation Parameter	Fracture?
1	3	1.12	0.685	Yes
7	8	1.18	1.317	Yes
10	12	1.31	0.868	Yes
14	15	1.61	1.414	Yes
18	19	0.92	1.06	Yes
28	29	1.04	1.155	Yes
32	33	0.8	1.124	Yes
34	35	1.1	1.389	Yes
37	38	1.38	1.467	Yes
45	47	0.62	0.907	Yes
48	49	0.85	1.108	Yes
1	5	0.57	0.876	No
6	8	1.32	1.048	No
6	9	0.85	1.04	No
13	16	1.18	0.749	No
14	17	0.81	1.119	No
19	20	1.25	0.782	No
31	33	1.13	1.044	No
44	46	0.61	1.039	No
n1	n2	0.6	0.715	No
n1	n3	0.77	0.593	No
n4	n5	0.96	0.827	No

Assuming a null hypothesis and a 95 % confidence, t critical (for two-tail) would fall within +/- 2.44 whereas the t-statistic was computed to be +/-1.06. Because the t-statistic falls within the t critical value, the null hypothesis is true, that is, there is no statistically significant difference in the two sets of population means. Hence this fracture propagation parameter does not work well with the specimen geometry shown in figure 7.2b. The reasons for this difference will be examined in the next section.

Table 7.5: t-test Analysis for Simkin's specimen using Fracture Initiation Parameter.

t-Test: Two-Sample: Intact and Cracked Boundaries		
	Intact	*Cracked*
Mean	0.89	1.18
Standard deviation	0.18	0.21
Variance	0.03	0.04
Observations	10	10
Pooled Variance	0.04	
Hypothesized Mean Difference	0	
df	18	
t Stat	-3.24	
t Critical one-tail	2.10	
t Critical two-tail	2.44	

Table 7.6: t-Test Analysis for Simkin's specimen using Fracture Propagation Parameter.

t-Test: Two-Sample : Intact and Cracked Boundaries		
	Intact	*Cracked*
Mean	0.95	1.08
Standard deviation	0.260	0.30
Variance	0.06	0.09
Observations	10	10
Pooled Variance	0.08	
Hypothesized Mean Difference	0	
df	18	
t Stat	-1.06	
t Critical one-tail	2.10	
t Critical two-tail	2.44	

7.5 Analysis of intact boundaries that have high $F_{A\rightarrow B}$ values

One of the grain boundaries (grain 13-grain 16) that did not result in cracking although registering a high $F_{A\rightarrow B}$ value (1.18) is shown in figure 7.3. The dominant twin traces for grains 13 and 16, their Schmid factors and the $F_{A\rightarrow B}$ value are provided. As shown at the top of the figure, the (-111) twin in grain 13 with the highest Schmid factor of 0.49 and $F_{A\rightarrow B}$ =1.18 might have resulted in the grain boundary cracking with grain 16, but these twins were not observed near the boundary. Instead, the twinning system with

$F_{A\to B}$ = 0.78 was most active at the boundary between grains 13 and 16, so the boundary remained intact.

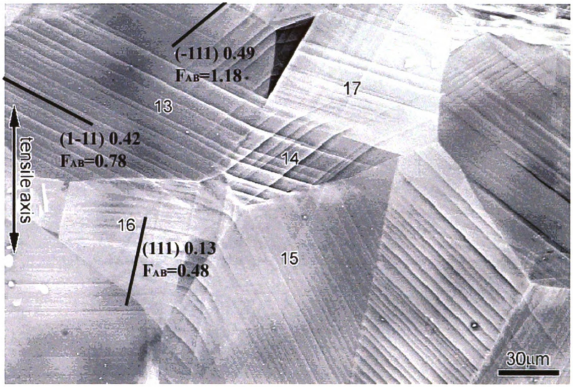

Figure 7.3. Interaction between grain 13 and grain 16. The dominant plane traces for both grains, their schmid factor and their $F_{A\to B}$ values were inserted. [16].

Another grain boundary with a high $F_{A\to B}$ value that remained intact is shown in figure 7.4. The interaction between grains 8 and 6 was calculated to have a high $F_{A\to B}$ value of 1.32 in the direction from grain 8 towards grain 6. Note that the boundary segment between grains 8 and grain 6 is relatively small. The stress and strain from either grain 6 or grain 8 were probably absorbed/accommodated by grains 7 or 9 that have a much larger contact with grains 6 and 8. The fact that a small microcrack occurred in the 7-8 grain boundary may have relieved the stress in the grain 6-8

boundary. Interestingly, the propagation parameter identified the 6-8 boundary as weaker than the 7-8 boundary, whereas the initiation parameter predicted the opposite.

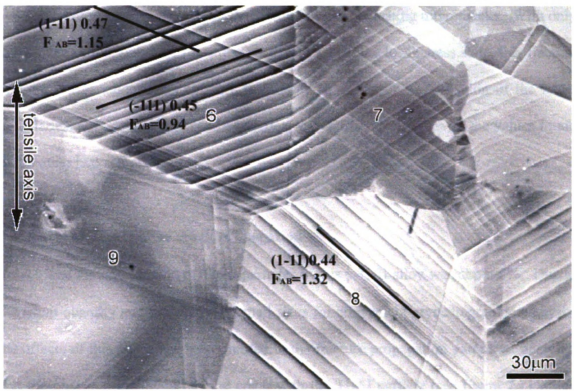

Figure 7.4. The grain boundary between grain 6 and grain 8 shows intact boundary [16].

If three of the intact boundaries (with high $F_{A\to B}$ values) were eliminated from the analysis, then there is a 90 % confidence that it will continue to follow the prediction of the Fracture propagation parameter. These two observations of exceptional intact grain boundaries indicates that the stress and strain shielding by neighboring grains is significant, making prediction strategies more complex.

The fracture propagation parameter takes into account the directionality of the twinning vector of the individual grain and their placement with respect to the direction of the propagating crack, as well as allowing twinning and ordinary dislocations to

accommodate strain across a boundary. That provides a very strong sense of the direction of the shearing strain. With Simkin's test specimen, twinning as an accommodation mechanism was not considered, suggesting that ordinary dislocation accommodation is more significant than twinning for nucleating microcracks. With only knowledge of the global tensile stress state, rather than the local stress state, this fracture propagation parameter was not able to provide as robust of a prediction of the intact boundaries, although the cracked boundaries were fairly consistent with the values found in the other two samples.

7.6 Effect of Ti_3Al on the crack propagation.

The volume fraction of Ti_3Al particles in this γ-TiAl alloy was about 8%. Due to the small quantity and prohibitively small sizes for convenient crystallographic analysis, the effects of this phase has been omitted in the fracture propagation parameter analysis. But the observed interaction of the crack with the Ti_3Al particle (see figure 7.1) which resulted in stalling the primary crack (toughening mechanism) and the formation of 140microcracks (non-toughening mechanism) on the edge some of these Ti_3Al particles (figure 6.7, 6.9 – 6.13), suggests that these inclusions might play a dual role in the fracture analysis. Further work is needed to examine how slip transfer does / does not occur from γ to the α_2 phase.

Samples A and sample B have slightly different geometry in terms of their orientation with respect to the notch root and the fracture propagation factor was robust enough to effectively predict the formation of microcracks and thereby provide the data needed to predict the path of the crack. Microcracks may nucleate at the grain boundary

due to the high $F_{A\to B}$ value between the two adjacent grains but the primary crack may not propagate through these microcracks. The primary crack, instead, will propagation via weak boundaries through the shortest route possible, cleaving into a crystal in order to move from one cluster of weak boundaries to another cluster of weak boundaries.

Chapter 8: Conclusions

This dissertation has focused primarily on active cracks as they propagated through the γ–γ grain boundaries. Cracks propagating through bulk γ-TiAl alloys were studied using a combination of electron backscattered patterns, selected area channeling patterns, electron channeling contrast imaging and x-ray techniques.

The Luster and Morris geometric compatibility factor was used to provide some insights into the slip transfer from one grain to another but the numeric value does not provide a convincing way to describe the effectiveness of the deformation transfer across the neighboring grain or to predict the opening of microcracks at the grain boundaries.

Microcracks nucleated at the grain boundaries as a result of the inability of the neighboring grain B to effectively accommodate the shear generated by the dominant deformation twins in grain A.

The microcracks observed at the γ–γ boundaries correlate well with a fracture propagation parameter $F_{A\text{-}B}$:

$$F_{A\rightarrow B} = m_{Atw}\left|\hat{b}_{Atw}\bullet\hat{t}\right|\left[\sum_{Bord=1}^{2}\left|\hat{b}_{Atw}\bullet\hat{b}_{Bord}\right| + \sum_{Btw=1}^{4}\hat{b}_{Atw}\bullet\hat{b}_{Btw}\Big|_{if>0}\right]$$

The fracture propagation parameter takes into account the directionality of the twinning vector of an individual grain and its orientation with respect to the direction of the propagating crack, as well as allowing twinning and ordinary dislocations to accommodate strain across a boundary.

With this fracture propagation parameter, it was observed that microcracking is less likely when $F_{A\rightarrow B} < 1.0$ but is more likely when $F_{A\rightarrow B} > 1.0$. This fracture

propagation parameter was able to predict intact or cracked boundaries following further crack growth based on the $F_{A\to B}$ values.

Although cracks nucleated in some of the weak boundaries, the primary crack did not necessary divert towards these microcracks. The primary crack had a tendency to propagate towards clusters of weak boundaries. Where it was not advantageous to follow a boundary directly, the crack cleaved through a grain, via the shortest distance towards the next cluster of weak boundaries.

This fracture propagation parameter was robust enough to consistently explain the observed crack path for two samples with different orientations with respect to the casting. Differences in texture in these two specimens had a large impact on the crack arrest capability.

Further work can be done to continue to improve on this parameter. Ti_3Al particles account for more than 8% of the weight percent and it was observed that these particles may either cause microcracks to form at the α_2–γ interface, which counterbalances the increase in ductility in the TiAl phase due to gettering effects. These particles and their effects were left out of the formulation. The fracture propagation parameter computed the relationship between the dominant twinning vector in one grain and the other slip vectors in a neighboring grain.

The plane normal criterion present in the Luster-Morris parameter was not considered in the computation of the fracture propagation parameter. Since directionality is important in this parameter, the change in orientation of the accommodating plane with respect to the dominant twinning plane might have some effect on this fracture

propagation parameter and the observed microcrack formation, and this warrants further investigation.

REFERENCES

1 M. Yamaguchi, "High Temperature Intermetallics- with Particular Emphasis On TiAl", Materials Science and Technology, April 1992, vol.8, 299-307 (1992).

2 D.M. Dimiduk, "Gamma Titanium Aluminides-An Emerging Materials Technology", Gamma Titanium Auminides, Edited by Y-W. Kim, R. Wager, and M. Yamaguchi, The Minerals, Metals & Materials Society, pp. 3-20 (1995).

3 D.M. Dimiduk, "Gamma Titanium Aluminide Alloys – An Assessment Within The Competition Of Aerospace Structural Materials", Materials Science and Engineering A263 281-288 (1999).

4 Young-Won Kim, "Intermetallic Alloys Based On Gamma Titanium Aluminde", JOM, Vol. 41, No. 7, July 1989, pp. 24-30 (1989).

5 D. Shechtman, M.J. Blackburn and H.A. Lipsitt, "The Plastic Deformation of TiAl", Metallurgical Transactions, Volume 5, June , pp.1373-1381 (1974).

6 S.M.L. Sastry and H.A. Lipsitt, "Fatigue Deformation of TiAl Base Alloys", Metallurgical Transactions A, Vol. 8A, February 1977, pp 299-308 (1977).

7 M. Yamaguchi and H. Inui, "TiAl Compounds For Structural Applications", Structural Intermetallics, Ed by R. Darolia, J.J. Lewandowski, C.T. Liu, P.L. Martin, D.B. Miracle and M.V. Nathal, The Minerals, Metals & Materials Society, pp. 127 – 142 (1993).

8 S. Huang, "Alloying Considerations in Gamma-Based Alloys", Structural Intermetallics, Ed by R. Darolia, J.J. Lewandowski, C.T. Liu, P.L. Martin, D.B. Miracle and M.V. Nathal, The Minerals, Metals & Materials Society, pp 299-307 (1993).

9 J.T. Czernuszka, N.J. Long and P.B. Hirsch, "Analysis of Defects in Bulk Semiconductors Using Electron Channeling Contrast Imaging", Inst. Phys. Conf., Ser. No 117: Section 10 (1991).

10 D.C. Joy, "Direct defect imaging in the high resolution SEM," MRS Proceeding, Vol. 183, Materials Research Society, pp. 199-209 (1990).

11 A.J. Wilkinson and P.B. Hirsch, "The effects of surface stress relaxation on electron channeling contrast imaging," Philosophical Magazine A, 72, No. 1, pp. 81-103 (1995).

12 A.J. Wilkinson, G.R. Anstis, J.T. Czernuszka, N.J. Long and P.B. Hirsch, "Electron channeling contrast imaging (ECCI) of interfacial defects in strained silicon-germanium layers on silicon," Philosophical Magazine A, 68 pp. 59-80 (1993).

13 B.C. Ng, B.A. Simkin and M.A. Crimp, "Examination of dislocations near crack tips in stoichiometric NiAl," Deformation and Fracture of Ordered Intermetallic Materials III, edited by W.O. Soboyejo, T.S. Srivatsan and H.L. Fraser, The Minerals, Metals and Materials Society, pp. 337-348 (1996).

14 M.N. Alam, M. Blackman and D.W. Pashley,"High-angle Kikuchi patterns," Proceeding of the Royal Society of London, Series A, Vol. 221, No, 1145, Jan. 21 1954, pp. 224-242 (1954).

15 S. Kikuchi, Japan Journal of Physic. 5, pp. 83-96 (1928).

16 B.A. Simkin, "Tensile crack initiation in γ–TiAl," Ph.D. Thesis, Michigan State University (2003).

17 Young-Won Kim, "Ordered Intermetallic Alloys, Part III: Gamma Titanium Aluminides", JOM, July 1994, pp.30-39 (1994).

18 H. Inui, A. Nakamura, M.H. Oh and M. Yamaguchi, "Deformation Structures in Ti-Rich TiAl Polysynthetically Twinned Crystals", Philosophical Magazine A, Vol. 66, No. 4, pp. 557-573 (1992).

19 H. Inui, M.H. Oh, A. Nakamura and M. Yamaguchi, "Ordered Domains in TiAl Coexisting With Ti3Al In The Lamellar Structure of Ti-rich TiAl Compounds," Philosophical Magazine A, Vol. 66, No. 4, pp. 539-555 (1992).

20 R.LeHolm, H. Clemens and H.Kestler, " Powder Metallurgy (PM) Gamma-Based Titanium Aluminide Structures For Use in Various High Temperature Aerospace Applications", Gamma Titanium Aluminides 1999, Edited by Y-W. Kim, D.M. Dimiduk, and M.H. Loretto, The Minerals, Metals & Materials Society, pp. 49-58 (1999).

21 M. Yamaguchi, and Y. Umakoshi, "The Deformation Behavior of Intermetallic Superlattice Compounds", Progress in Materials Science Vol. 34, pp. 1-148 (1990).

22 Fu-Sheng Sun, C.X. Cao, M.G. Yan, Y.T. Lee and S.E. Kim, "Solid solution strengthening mechanism of TiAl alloy," Gamma Titanium Auminides 1999, Edited by Y-W. Kim, D.M. Dimiduk, and M.H. Loretto, TMS, pp. 415-422 (1999).

23 S.C. Huang and E.L. Hall, "The Effects Of Cr. Additions To Binary TiAl-Base Alloys," Metallurgical Transactions A, Vol. 22A, pp. 2619-2627 (1991).

24 S.C. Huang and E.L. Hall, "Characterization Of The Effect Of Vanadium Additions To TiAl Base Alloys," Acta Metallurgical Materialia, Vol. 39 No. 6 pp. 1053-1060 (1991).

25 T. Tsujimoto and K. Hashimoto, "Structures And Properties of TiAl-based Alloys Containing Mn," Materials Research Society Symposium. Proceeding, Vol. 133, pp391-396 (1989).

26 Yoo-Dong Hahn and Sung H. Whang, " Deformation And Its Structure In $L1_0$ Ti-Al-Nb Compound Alloys," Materials Research Society Symposium. Proceeding, Vol. 133, pp. 385-390 (1989).

27 D.Hu, A.B. Godfrey and M.H. Loretto, "Characterization Of Thermally Exposed TiAlCrNb Alloys," Gamma Titanium Aluminides 1999, Edited by Y-W. Kim, D.M. Dimiduk, and M.H. Loretto, The Minerals, Metals & Materials Society, pp. 409-414 (1999).

28 T. Sikora, M. Jaouen and G. Hug, "Bonding mechanisms in ternary g-TiAl + X (X=Cr, Mn, Nb): a comparison between absorption near edge fine structures and theoretical predictions," Gamma Titanium Auminides 1999, Edited by Y-W. Kim, D. M. Dimiduk, and M. H. Loretto, The Minerals, Metals & Materials Society, 1999, pp. 83-88 (1999).

29 T. Kawabata, T. Tamura and O. Izumi, "Parameters for ductility improvement in TiAl," High Temperature Ordered Intermetallic Alloys III, edited by C.T. Liu, A.I. Taub, N.S. Stoloff and C.C. Koch, Materials Research Society Symposium Proceedings, Vol. 133, pp. 329-334 (1989).

30 C. Woodward, S.A. Kajihara, S.I. Rao, and D.M. Dimiduk, " The Influence Of Solid Solutions On Flow Behavior In Gamma-TiAl," Gamma Titanium Aluminides 1999, Edited by Y-W. Kim, D.M. Dimiduk, and M.H. Loretto, The Minerals, Metals & Materials Society, pp. 49-58 (1999).

31 H. Mecking, CH.Hartig, and U. F. Kocks, "Deformation Modes in γ-TiAl As Derived From The Single Crystal Yield Surface", Acta Materialia, Vol. 44, No. 4, pp. 1300-1321 (1996).

32 M.A. Morris, "Dislocation Configurations In Two-Phase Ti-Al Alloys.III. Mechanisms Producing Anomalous Flow Stress Dependence On Temperature", Philosophical Magazine A, Vol. 69, No. 1, pp. 129-150 (1994).

33 S. Zghal, A. Coujou and A. Couret, "Transmission Of The Deformation Through γ-γ Interface In A Polysynthetically Twinned TiAl Alloy. I. Ordered Domain Interfaces 120° rotational)", Philosophical Magazine A, Vol. 81, No. 2, pp. 345-364 (2001).

34 S. Zghal and A. Couret, " Transmission Of The Deformation Through γ-γ Interface In A Polysynthetically Twinned TiAl Alloy. II. Twin Interface (180° rotational)", Philosophical Magazine A, Vol. 81, No. 2, pp. 365-382 (2001).

35 Gibson MA, Forwood CT, "Slip transfer of deformation twins in duplex gamma - based Ti-Al alloys. III. Transfer across general large-angle gamma - gamma grain boundaries," Philosophical Magazine A. Vol. 82, 1381- 1404 (2002).

36 J. Luster, and M.A. Morris, "Compatibility of Deformation in Two-Phase TiAl Alloys: Dependence on Microstructure and Orientation Relationships", Metallurgical and Materials Transactions A, Vol. 26A, July 1995, pp.1745-1756 (1995).

37 B.A Simkin, T.R. Bieler and M.A. Crimp. "Tensile Microcrack Initiation at γ–γ Boundaries in TiAl", ", Mechanisms and Mechanics of Fracture: The John Knott Symposium, eds. W.O. Soboyejo, J.J. Lewandowski, and R.O. Ritchie, The Minerals, Metals & Materials Society, Warrendale, P.A. pp. 309-314 (2002).

38 B.C.Ng, T.R. Bieler, M.A, Crimp, "Effect of Crystal Orientation on Crack Nucleation and Arrest in a Near-Gamma TiAl Alloy", Mechanisms and Mechanics of Fracture: The John Knott Symposium, eds. W.O. Soboyejo, J.J. Lewandowski, and R.O. Ritchie, The Minerals, Metals & Materials Society, Warrendale, P.A. pp. 303-308 (2002).

39 Dale E Newbury, " The origin, detection, and uses of electron channeling contrast," Scanning Electron Microscopy, pp. 1047-1054 (1974).

40 David Joy, Dale E Newbury, David Davidson, "Electron channeling patterns in the scanning electron microscope," Journal of Applied Physics, Vol. 53, No. 8, August 1982 pp. 81-122 (1982).

41 T. Ichinokawa, M. Nishimura, H. Wada, "Contrast reversals of pseudo-Kikuchi bands and lines due to detector position in scanning electron microscopy," Journal of the Physical Society of Japan, 36 No. 1, pp. 221-226 (1974).

42 D.G. Coates, "Kikuchi-like reflection patterns obtained with the SEM," Philosophical Magazine, 16 (1967), pp. 1179-1184 (1967).

43 G.R.Booker, A.M.B. Shaw, M.J. Whelan, and P.B. Hirsch, "Some Comments on the Interpretation of 'Kikuchi Like Reflection Patterns' Observed by Scanning Electron Microscopy," Philosophical Magazine, 16 , pp. 1185-1191 (1967).

44 B.C. Ng, B. Ghosh and M.A. Crimp, "Electron Channeling Contrast Imaging of dislocations near crack tips in bulk NiAl single crystals", Interstitial and Substitutional Effects in Intermetallics, 1998 TMS Proceedings, editied by I. Baker, R.D. Noebe and E.P. George, pp. 163-176 (1998).

45 B.A. Simkin, M.A. Crimp, "Dislocation detection depth measurements in silicon using electron channeling contrast imaging," Proceedings, Microscopy and Microanalysis, edited by G.W. Bailey, J.M. Corbett, R.V.W. Dimlich, J.R. Michael and N.J. Zaluzec, 1996, pp. 140-141 (1996).

46 J.T. Czernuszka, N.J. Long, E.D. Boyes, and P.B. Hirsch, "Electron Channeling Contrast Imaging (ECCI) of Dislocations in Bulk Specimens, Materials Research Society Symposium Proceeding, Vol. 209, pp. 289-292 (1991).

47 J.A. Venables and C.J. Harland, "Electron back-scattering patterns – A new technique for obtaining crystallographic information in the scanning electron microscope," Philosophical Magazine, 27, 1193-1200 (1973).

48 D.J. Dingley, "Diffraction from sub-micron areas using electron backscattering in a scanning electron microscope," Scanning Electron Microscope. 1984 II: 569-575 (1984).

49 D.J.Dingley and Karim Baba-Kishi, "Use of electron back scatter diffraction patterns for determination of crystal symmetry elements," Scanning Electron Microscopy, vol. II, pp. 383-391 (1989).

50 Tim Maitland, "Electron Backscattered Diffraction", Advanced Materials & Processes, May 2004, pp. 34-36 (2004).

51 Stuart I. Wright and Brent L. Adams, "Automatic analysis of electron backscatter diffraction patterns," Metallurgical Transactions A, vol.23A, March 1992, pp. 759-767 (1992).

52 D.J. Dingley and V Randle, "Review microtexture determination by electron back-scatter diffraction," Journal of Materials Science, 27 pp.4545-4566 (1992).

53 P.N. Quested, P.J. Henderson and M. Mclean, "Observations of deformation and fracture heterogeneities in a nickel-base superalloy using electron back scattering patterns," Acta Metallurgical, Vol. 36, No. 10. pp. 2743-2752 (1988).

54 J.R. Michael and R.P. Goehner, " Crystallographic Phase Identification in the Scanning Electron Microscope: Backscattered Electron Kikuchi Patterns Imaged with a CCD-Based Detector", MSA Bulletin Vol. 23, No. 2, pp. 168-175 (1993).

55 Stuart I. Wright, Brent L. Adams and Karsten Kunze, "Application of a new automatic lattice orientation measurement technique to polycrystalline aluminum," Materials Science and Engineering A160 pp.229-240 (1993).

56 Brent L. Adams, Stuart I. Wright and Karsten Kunze, "Orientation imaging: The emergence of a new microscopy," Metallurgical Transaction A, Vol. 24A, April 1993, pp.819-831 (1993).

57 Michael J. R, Sandia National Laboratories, private communication, Nov. 2001.

58 J.S. Kallend, et. al, "Operational Texture Analysis", Materials Science and Engineering A132, pp.1- 11 (1991).

59 Y.He, et. al., "Elastic constants and thermal expansion of single crystal g-TiAl from 300 to 750 K," Materials Science and Engineering A239-240, pp. 157-163 (1997).

60 J. Zhang, et. al., "A fractographic study on tensile fracture surface of duplex microstructure TiAl alloy," Scripta Materialia, 32 (12) 1815-1818 (1996).

61 B.A. Simkin, M.A. Crimp, T.R. Bieler and D.E. Mason, "The Effect of Crystal Orientation on Deformation Transfer at γ-γ Boundaries in a Near-γ TiAl Based Alloy," Structural Intermetallics 2001, eds. K.J. Hemker, D.M. Dimiduk, et al., TMS, Warrendale, PA, pp. 391-400 (2001).

62 B.C. Ng , B.A, Simkin and M.A, Crimp, "Application of the Electron Channeling Contrast Imaging Technique to the Study of Dislocations Associated with Cracks in Bulk Specimens," Ultramicroscopy 75, pp. 137-145 (1998).

63 V.K. Vasudevan, M.A Stucke, S.A. Court and H.L. Fraser, "The influence of second phase Ti_3Al on the deformation mechanism in TiAl", Phil. Mag. Letter, 59, (6) p. 299-307 (1989).

64 Y.H. Lu, Y.G. Zhang, L.J. Qiao, Y.B. Wang, C.Q.Chen, W.Y. Chu, "In-Situ TEM study of fracture mechanisms of polysynthetically twinned (PST) crystals of TiAl alloys", Materials Science and Engineering A289, pp. 91-98 (2000).

Appendices

Appendix 1
Determination of Grain Orientation

Color	Traces
Red (thin-solid)	(100)
Purple (thin-solid)	(010)
Orange (thin-dashed)	(001)
Black (thick-solid)	(110)
Blue (thick-solid)	(1-10)
Green (thick-dashed)	(101)
Cyan (thick-dashed)	(-101)
Blue (thick-dotted)	(011)
Magenta (thick-dotted)	(01-1)

Reprint from figure 3.9.
The traces in the computed stereographs followed the above color code.

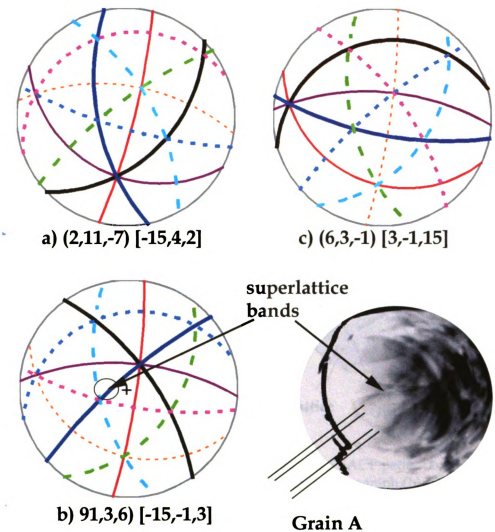

Figure A1-1. Three possible stereographs and a SACP pattern of grain A. The superlattice band from the SACP pattern matches stereograph (b) having grain normal (91,3,6).

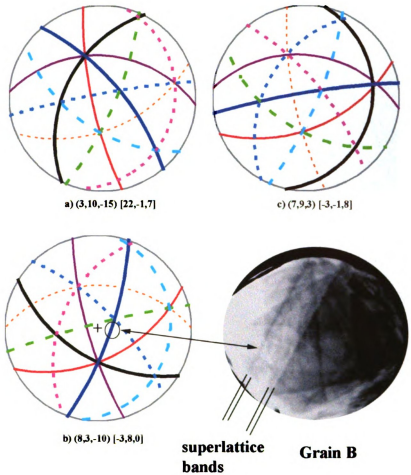

Figure A1-2. Three possible stereographs and a SACP pattern of grain B. The superlattice band from the SACP pattern matches stereograph (b) having grain normal (8,3,-10).

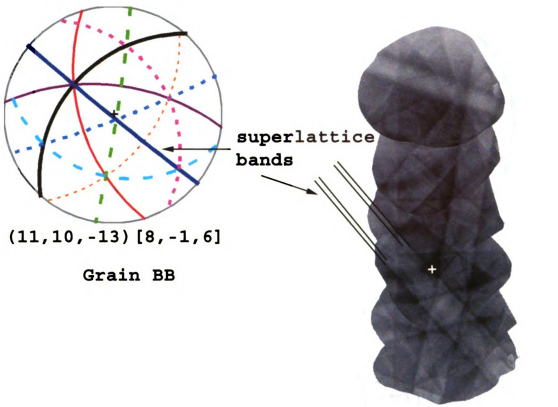

Figure A1-3. Stereograph and composite SACP pattern of grain BB. The superlattice band from the composite SACP pattern matches stereograph with grain normal (11,10,-13).

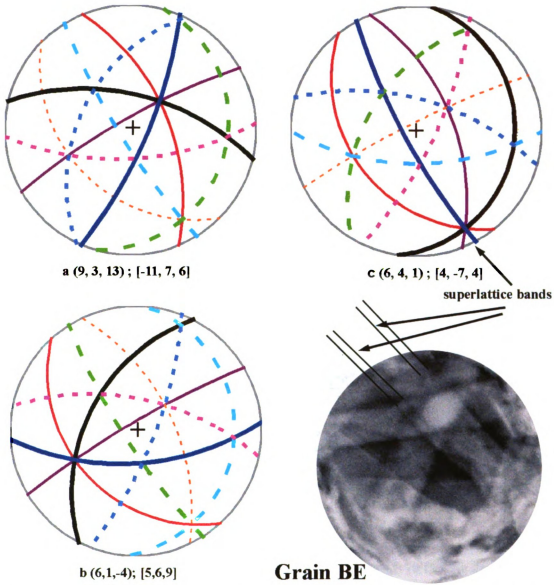

Figure A1-4. Three possible stereographs and a SACP pattern of grain BE. The superlattice band from the SACP pattern matches stereograph (c) having grain normal (6,4,1).

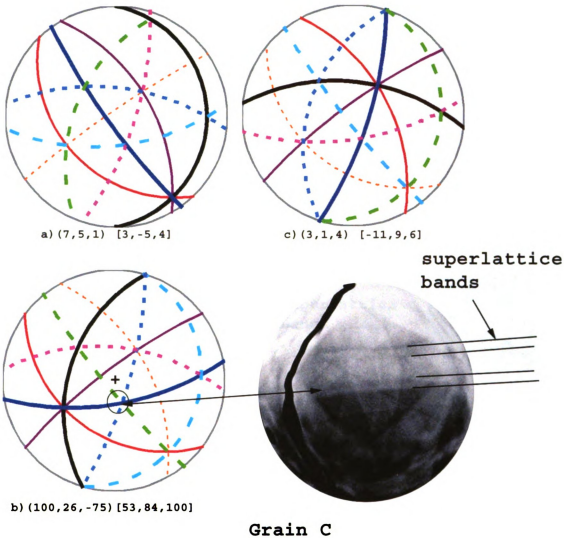

Figure A1-5. Three possible stereographs and a SACP pattern of grain C. The superlattice band from the SACP pattern matches stereograph (b having grain normal (100,26,-75).

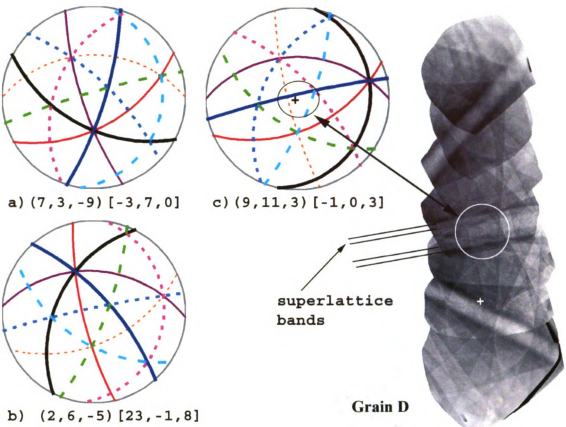

Figure A1-6. Three possible stereographs and a SACP pattern of grain D. The superlattice band from the SACP pattern matches stereograph (c) having grain normal (9,11,3).

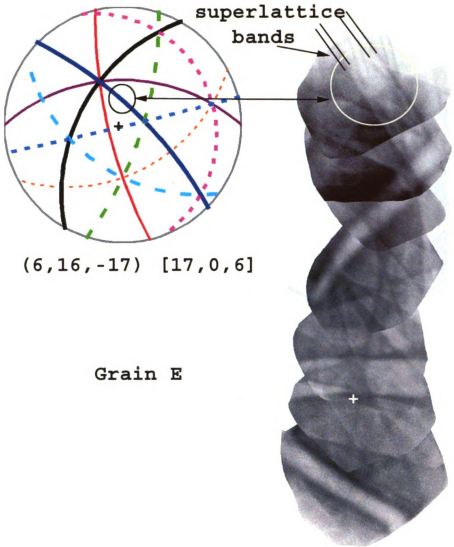

Figure A1-7. Stereograph and composite SACP pattern of grain E. The superlattice band from the composite SACP pattern corresponds well with stereograph with grain normal (6,16,-17).

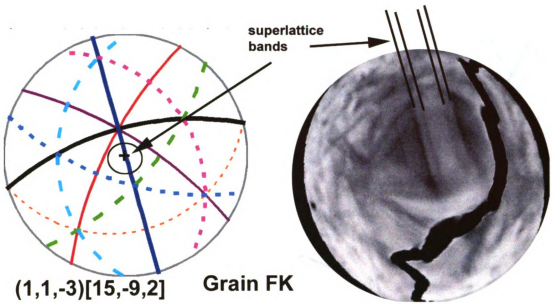

Figure A1-8. Stereograph and composite SACP pattern of grain FK. The superlattice band from the composite SACP pattern corresponds well with stereograph with grain normal (1,1,-3).

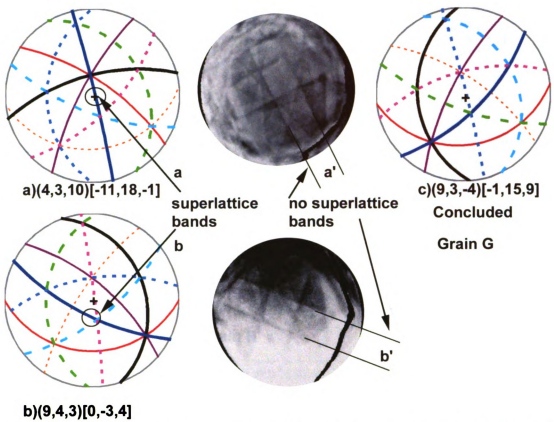

Figure A1-9. Three possible stereographs and a SACP pattern of grain G. The band ***a'*** from the top SACP corresponds to the superlattice ***a*** shown in the stereograph (a) and while band ***b'*** corresponds to superlattice b (b). Since both bands ***a'*** and ***b'*** do not show any superlattice information, stereographs a and b are incorrect and are eliminated. Grain c with normal, (9,3,-4), is therefore the correct solution for grain G.

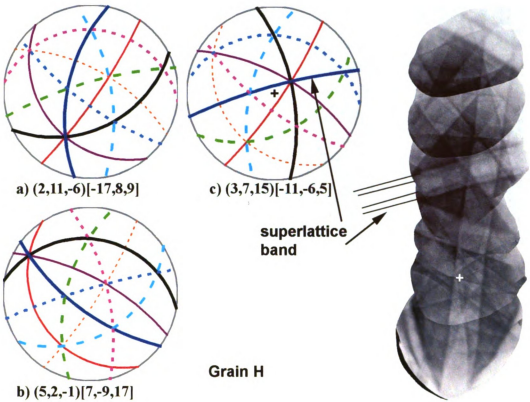

Figure A1-10. Three possible stereographs and a SACP pattern of grain H. The superlattice band from the SACP pattern matches stereograph (c) having grain normal (3,7,15).

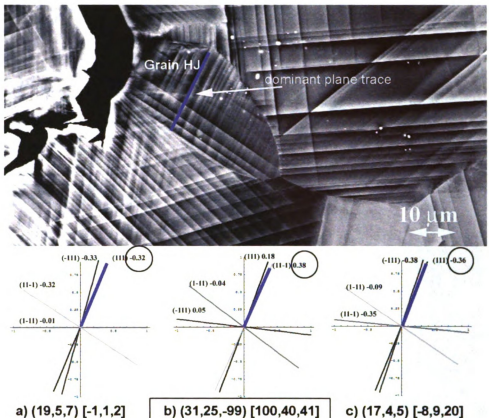

Figure A1-11. BSE image of grain HJ (labeled) with three possible plane traces superimposed on the image. The dominant twining plane corresponds well with the positive Schmid factor displayed by the plane trace analysis (b), with grain normal (31,25,-99).

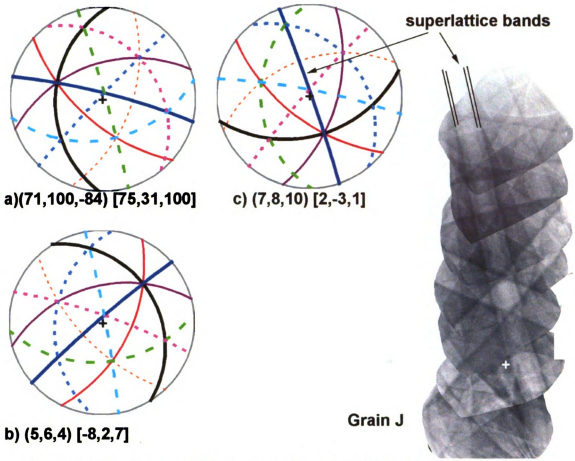

Figure A1-12. Three possible stereographs and a SACP pattern of grain J. The superlattice band from the SACP pattern matches stereograph (c) having grain normal (7,8,10).

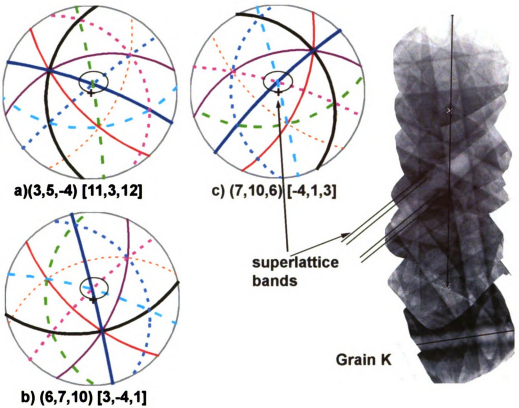

Figure A1-13. Three possible stereographs and a SACP pattern of grain K. The superlattice band from the SACP pattern matches stereograph (c) having grain normal (7,8,10).

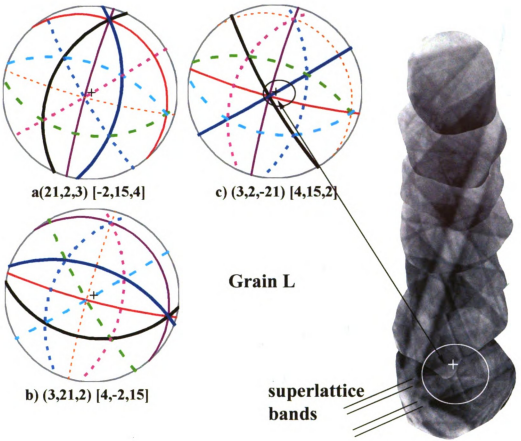

Figure A1-14. Three possible stereographs and a SACP pattern of grain L. The superlattice band from the SACP pattern matches stereograph (c) having grain normal (3,2,-21).

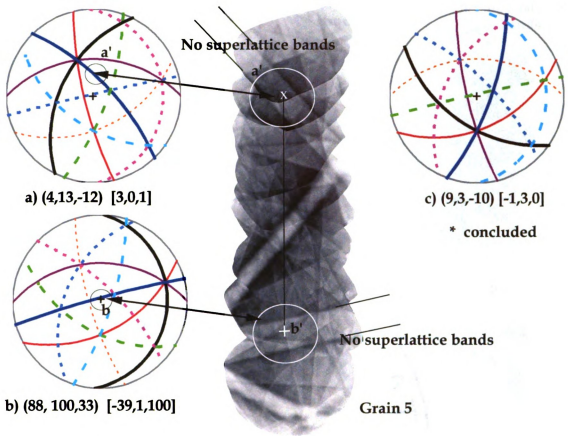

Figure A1-15. Three possible stereographs and a composite SACP pattern of grain 5. The band ***a'*** from the composite SACP corresponds to the superlattice ***a*** shown in the stereograph (a) while band ***b'*** corresponds to superlattice b in sterograph (b). Since both bands ***a'*** and ***b'*** do not show any superlattice information, stereographs a and b are incorrect and are eliminated. Grain 5 with normal, (9,3,-10), is therefore the correct solution for grain 5.

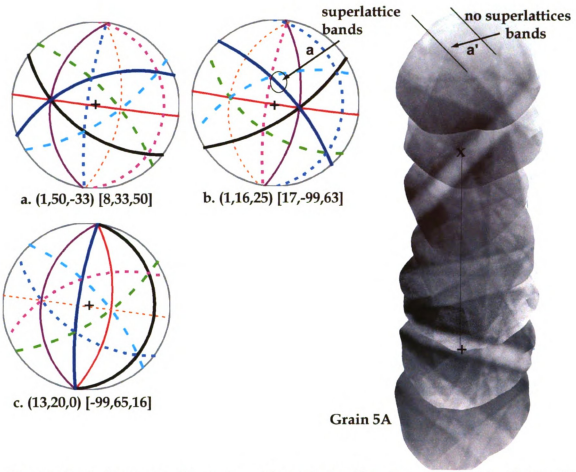

Figure A1-16. Three possible stereographs and a SACP pattern of grain 5A. The band ***a***'from the top SACP corresponds to the superlattice ***a*** shown in the stereograph (a). Since band a' does not shown any superlattice information, stereograph (b) is eliminated. Further analysis is needed and is shown in figure A1-17.

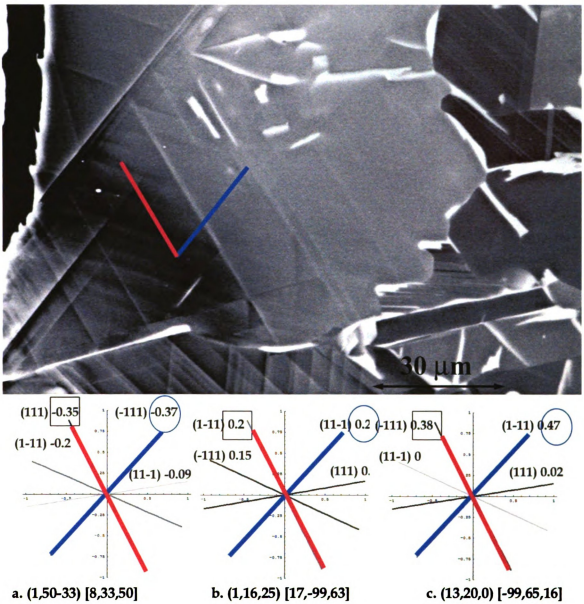

Figure A1-17. BSE image of grain 5A with three possible plane traces superimposed on the image. Since plane trace (b) had been eliminated earlier (see Figure A1-16) and plane trace (a) showed negative Schmid factors for both the dominant twinning planes, the plane trace (c) with normal (13,20,0) was selected as the correct grain orientation.

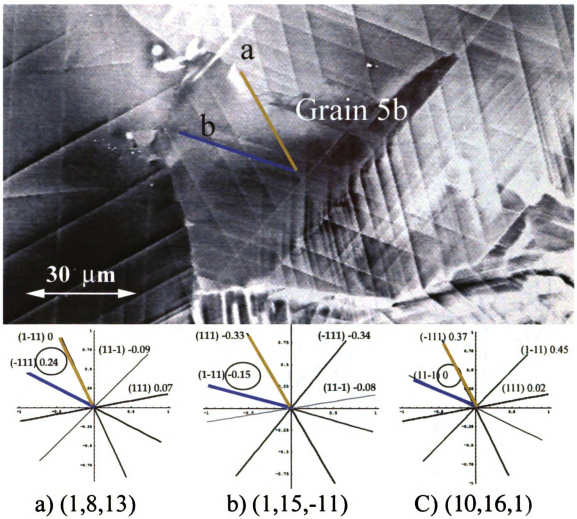

Figure A1-18. BSE image of grain 5B with three possible plane traces superimposed on the image. From the BSE image, plane trace **a** has the characteristic of pre-existed (evenly distributed twins) while plane trace **b** is the dominating deformation twin. Plane trace analysis (a) with a grain normal (1,8,13) and a high positive Schmid factor corresponding to band **b** is the most likely the correct grain orientation. Plane trace analysis (b) and (c) both showed negative and low Schmid factor respectively for the dominating deformation twin.

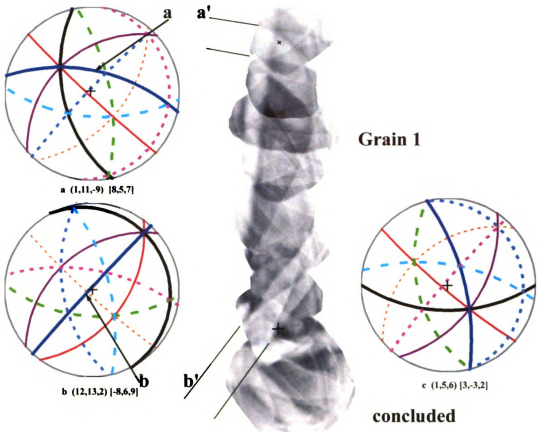

Figure A1-19. Three possible stereographs and a composite SACP pattern of grain 1. The band ***a'*** from the composite SACP corresponds to the superlattice ***a*** shown in the stereograph (a) while band ***b'*** corresponds to superlattice b in sterograph (b). Since both bands ***a'*** and ***b'*** do not show any superlattice information, stereographs a and b are incorrect and are eliminated. Grain 1 with normal, (1,5,6), is therefore the correct solution for grain 1.

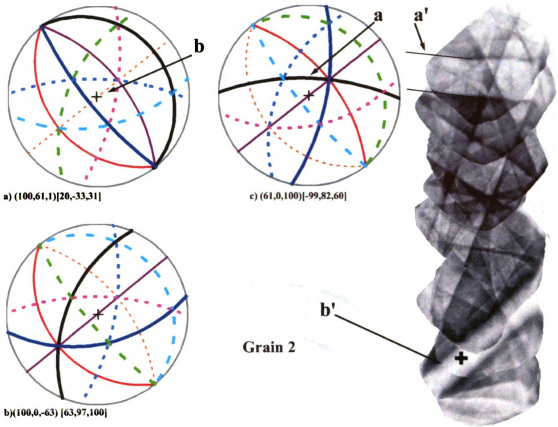

Figure A1-20. Three possible stereographs and a composite SACP pattern of grain 2. The band ***a'*** from the composite SACP corresponds to the superlattice ***a*** shown in the stereograph (c) while band ***b'*** corresponds to superlattice b in sterograph (a). Since both bands ***a'*** and ***b'*** do not show any superlattice information, stereographs a and b are incorrect and are eliminated. Grain 2 with normal, (100,0,-63), is therefore the correct solution.

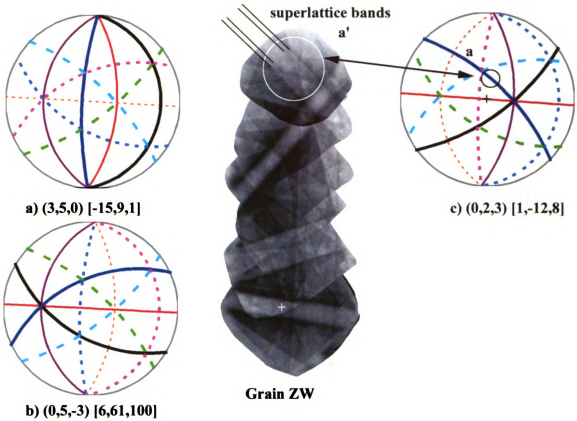

Figure A1-21. Three possible stereographs and a composite SACP pattern of grain ZW. The superlattice band ***a'*** from the composite SACP corresponds to the superlattice ***a*** shown in the stereograph (c), confirming that grain ZW with grain normal (0,2,3) is the correct orientation.

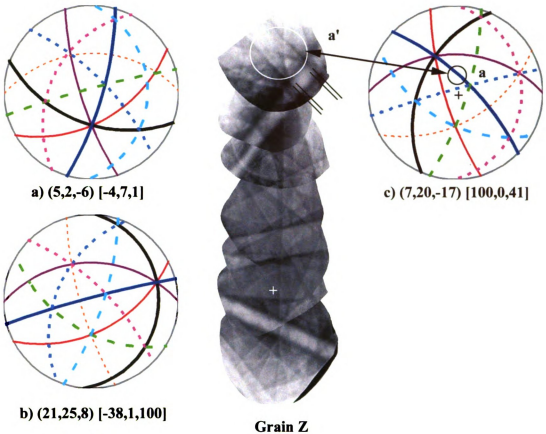

Figure A1-22. Three possible stereographs and a composite SACP pattern of grain Z. The superlattice band ***a'*** from the composite SACP corresponds to the superlattice ***a*** shown in the stereograph (c), confirming that grain ZW with grain normal (7,20,-17) is the correct orientation.

Appendix 2
Images of Grain interactions

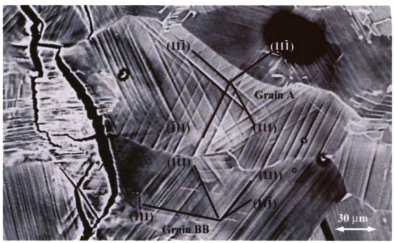

Figure A2-1. Intact boundary between grain A and grain BB

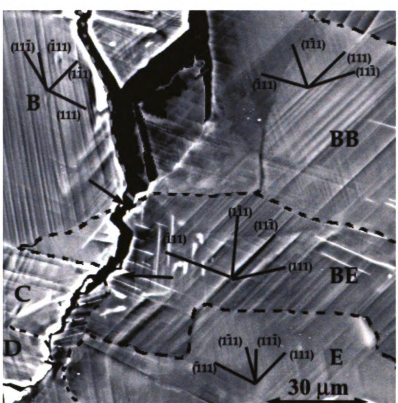

Figure A2-2. Interaction between grains B and BB is shaded gray. Microcracks (arrowed) at the grain boundaries between C and BE and B and BE. Intact boundaries between grains E and BE, BE and BB.

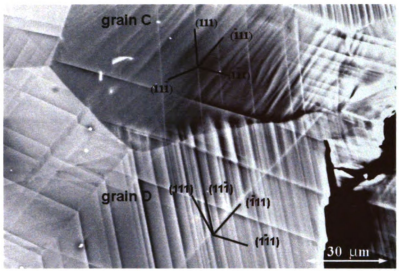

Figure A2-3. Intact grain boundary between grain C and grain D

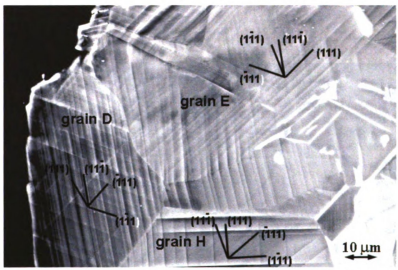

Figure A2-4. Grain interaction between grains D-E-H

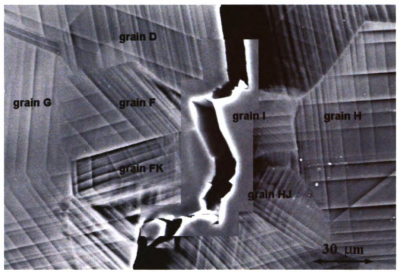

Figure A2-5. Interaction at grain boundaries between grains D, F,FK,H,I and HJ. An SE image had been superimposed over the BSE image to provide additional information on the crack edges. Higher magnifications of the grain interaction are shown in figure A2-6 and A2-7.

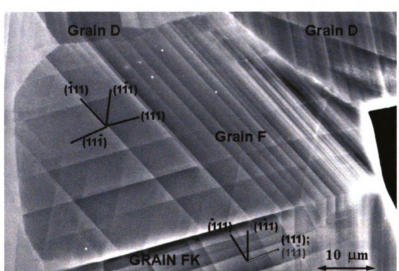

Figure A2-6. Intact boundaries between grains D and F, and between F and FK.

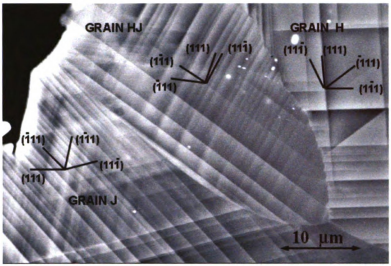

Figure A2-7. Intact boundaries between grains H –HJ and grains HJ- J.

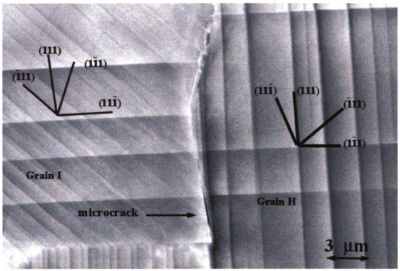

Figure A2-8. Cracked boundary (arrowed) between grain I and grain H.

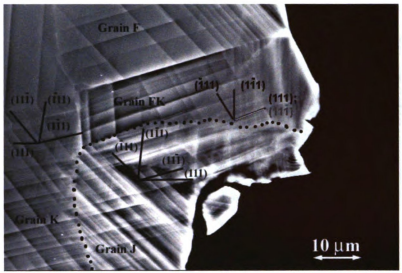

Figure A2-9. Interaction between grains FK – K- J. Intact boundary between grains FK –J as well as between grains FK – K.

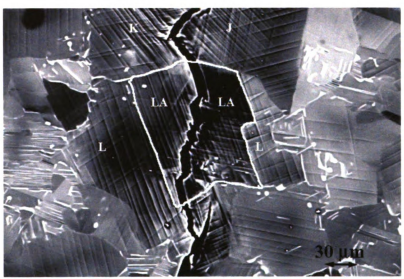

Figure A2-10. Low magnification of grains K-J-L and LA. Higher magnification are shown in figures A2-11-12.

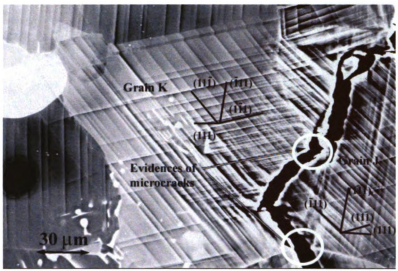

Figure A2-11. Evidences of cracked boundaries between grains K and J. The observation of 'stepped or jogged' in the crack path strongly suggest the presence of microcracks that resulted in the change in the crack path.

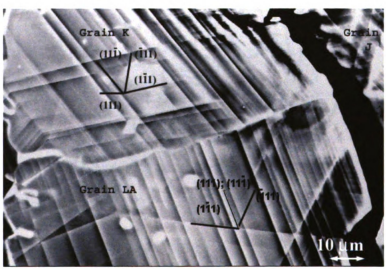

Figure A2-12. Intact boundaries between grains K and LA.

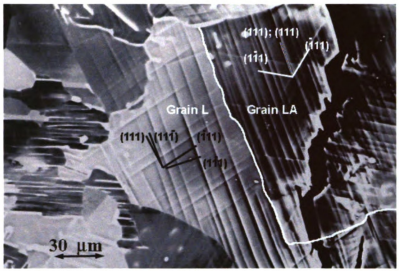

Figure A2-13. Intact boundaries between grains L and LA.

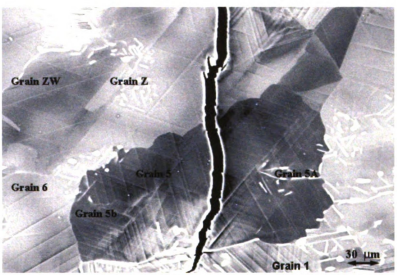

Figure A2-14. Grain interactions between grains ZW-Z-5-5A-5B-1. Higher magnification images are shown in figures A2-15.

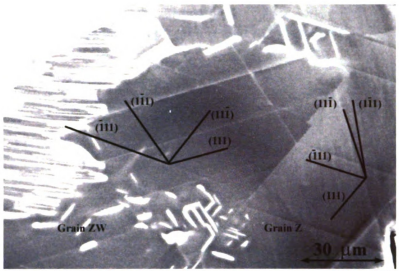

Figure A2-15. Intact boundaries between grains ZW and Z.

Appendix 3
Computational programs used in the analysis

Program #1

Fracture Propagation Parameter Program.
Run via MathCad Software.

Grain A and Grain B
Crystal Information / Lattice Parameters

$$A_1 := \begin{pmatrix} 1 \\ 1 \\ -2 \end{pmatrix}$$

$a := 1$

$b := 1$

$c := 1.02$

Unit Vector WRT Orthonormal CS Given Coordinates WRT Tetragonal CS

$$B_1 := \begin{pmatrix} 0 \\ 1 \\ 1 \end{pmatrix}$$

$$Mag(g) := \sqrt{(g_0 \cdot a)^2 + (g_1 \cdot b)^2 + (g_2 \cdot c)^2}$$

$C_1 := A_1 \cdot B_1$

$$unit(g) := \frac{\begin{pmatrix} a \cdot g_0 \\ b \cdot g_1 \\ c \cdot g_2 \end{pmatrix}}{Mag(g)}$$

$C_1 = -1.00$

Grain Surface Normal/Tensile Axis Information; column i corresponds to the surface normal and tensile axis for that grain with respect to the fct coordinate system.

INDICES ARE INPUTTED VERTICALLY

(h)
(surface normals, tensile directions) (k)
(l)

$$N_g := \begin{pmatrix} 17 & 17 & 3 \\ 7 & 43 & 4 \\ 10 & 24 & 1 \end{pmatrix}$$

$$T_g := \begin{pmatrix} 146 & 497 & 19 \\ -146 & -499 & -18 \\ -146 & 542 & 15 \end{pmatrix}$$

Conversion Of Normal/Tensile Directions To Unit Vectors in Real Space

$N1 := (\text{unit}(N_g^{\langle 0 \rangle}))$
$N2 := (\text{unit}(N_g^{\langle 1 \rangle}))$
$N6 := (\text{unit}(N_g^{\langle 2 \rangle}))$
$T1 := (\text{unit}(T_g^{\langle 0 \rangle}))$
$T2 := (\text{unit}(T_g^{\langle 1 \rangle}))$
$T6 := (\text{unit}(T_g^{\langle 2 \rangle}))$
S1 := T1 × N1
S2 := T2 × N2
S6 := T6 × N6
*** We do not use N6 or the third grain.**

Back-calculation Of Rotation Matrices From Grain To Lab Basis. The transformation operates under the assumptions that N corresponds to k, T corresponds to j, and TxN corresponds to jxk = i.

$$A(N,T,S) := \begin{pmatrix} N_0 & N_1 & N_2 & 0 & 0 & 0 & 0 & 0 & 0 \\ 0 & 0 & 0 & N_0 & N_1 & N_2 & 0 & 0 & 0 \\ 0 & 0 & 0 & 0 & 0 & 0 & N_0 & N_1 & N_2 \\ T_0 & T_1 & T_2 & 0 & 0 & 0 & 0 & 0 & 0 \\ 0 & 0 & 0 & T_0 & T_1 & T_2 & 0 & 0 & 0 \\ 0 & 0 & 0 & 0 & 0 & 0 & T_0 & T_1 & T_2 \\ S_0 & S_1 & S_2 & 0 & 0 & 0 & 0 & 0 & 0 \\ 0 & 0 & 0 & S_0 & S_1 & S_2 & 0 & 0 & 0 \\ 0 & 0 & 0 & 0 & 0 & 0 & S_0 & S_1 & S_2 \end{pmatrix}$$

$$Q(x) := \begin{pmatrix} x_0 & x_1 & x_2 \\ x_3 & x_4 & x_5 \\ x_6 & x_7 & x_8 \end{pmatrix}$$

$$b := \begin{pmatrix} 0 \\ 0 \\ 1 \\ 0 \\ 1 \\ 0 \\ 1 \\ 0 \\ 0 \end{pmatrix}$$

$$Q_1 := Q\left(A(N1, T1, S1)^{-1} \cdot b\right)$$

$$Q_2 := Q\left(A(N2, T2, S2)^{-1} \cdot b\right)$$

$$Q_6 := Q\left(A(N6, T6, S6)^{-1} \cdot b\right)$$

Check Orthogonality:

$$Q_1 \cdot Q_1^T = \begin{pmatrix} 1.00 & 0.00 & 0.00 \\ 0.00 & 1.00 & 0.01 \\ 0.00 & 0.01 & 1.00 \end{pmatrix} \quad Q_2^T \cdot Q_2 = \begin{pmatrix} 1.00 & -0.00 & -0.01 \\ -0.00 & 1.01 & -0.00 \\ -0.01 & -0.00 & 0.99 \end{pmatrix}$$

$$Q_6^T Q_6 = \begin{pmatrix} 1.00 & -0.00 & -0.00 \\ -0.00 & 1.00 & -0.00 \\ -0.00 & -0.00 & 1.00 \end{pmatrix}$$

Check Mapping of Basis Vectors:

$$Q_1 \cdot (T1 \times N1) = \begin{pmatrix} 1.00 \\ 0.00 \\ 0.00 \end{pmatrix}$$

$$Q_1 \cdot T1 = \begin{pmatrix} 0.00 \\ 1.00 \\ 0.00 \end{pmatrix} \qquad Q_1 \cdot N1 = \begin{pmatrix} 0.00 \\ 0.00 \\ 1.00 \end{pmatrix}$$

$$Q_2 \cdot (T2 \times N2) = \begin{pmatrix} 1.00 \\ 0.00 \\ 0.00 \end{pmatrix}$$

$$Q_2 \cdot T2 = \begin{pmatrix} 0.00 \\ 1.00 \\ 0.00 \end{pmatrix} \qquad Q_2 \cdot N2 = \begin{pmatrix} 0.00 \\ 0.00 \\ 1.00 \end{pmatrix}$$

$$Q_6 \cdot (T6 \times N6) = \begin{pmatrix} 1.00 \\ 0.00 \\ 0.00 \end{pmatrix}$$

$$Q_6 \cdot T6 = \begin{pmatrix} 0.00 \\ 1.00 \\ 0.00 \end{pmatrix} \qquad Q_6 \cdot N6 = \begin{pmatrix} 0.00 \\ 0.00 \\ 1.00 \end{pmatrix}$$

It follows that rotation Qi carries a vector written in the crystal basis into its equivalent vector in the lab basis.

Define all possible slip systems:

DEFORMATION SYSTEMS;
M=planes, D=deformation vector.

$$M := \begin{pmatrix} 1 & 1 & 1 & 1 & -1 & -1 & -1 & -1 & 1 & 1 & 1 & 1 & -1 & -1 & -1 & -1 \\ 1 & 1 & 1 & 1 & 1 & 1 & 1 & 1 & -1 & -1 & -1 & -1 & -1 & -1 & -1 & -1 \\ 1 & 1 & 1 & 1 & 1 & 1 & 1 & 1 & 1 & 1 & 1 & 1 & 1 & 1 & 1 & 1 \end{pmatrix}$$

$$D := \begin{pmatrix} 1 & 1 & 1 & 0 & -1 & 1 & 1 & 0 & 1 & 1 & 1 & 0 & -1 & 1 & 1 & 0 \\ 1 & -1 & 0 & 1 & 1 & 1 & 0 & 1 & -1 & 1 & 0 & 1 & -1 & -1 & 0 & 1 \\ -2 & 0 & -1 & -1 & -2 & 0 & 1 & -1 & -2 & 0 & -1 & 1 & -2 & 0 & 1 & 1 \end{pmatrix}$$

Define functions to transform slip system normal and direction vectors into lab basis:

$m_1(i) := Q_1 \cdot (\text{unit}(M^{\langle i \rangle}))$

$m_2(i) := Q_2 \cdot (\text{unit}(M^{\langle i \rangle}))$

$m_6(i) := Q_6 \cdot (\text{unit}(M^{\langle i \rangle}))$

$d_1(i) := Q_1 \cdot (\text{unit}(D^{\langle i \rangle}))$

$d_2(i) := Q_2 \cdot (\text{unit}(D^{\langle i \rangle}))$

$d_6(i) := Q_6 \cdot (\text{unit}(D^{\langle i \rangle}))$

The tensile direction or the tilt direction in lab space (T)

$T := Q_1 \cdot T1$

Calculate compatibilty factors for all possible combinations of slip system combinations between grains 1 and 2 : (m_{1x})

$m_{12}(i, j) := (m_1(i) \cdot m_2(j))(d_1(i) \cdot d_2(j))$

$M_{12} := \text{matrix}(16, 16, m_{12})$

SLIP SYSTEM NUMBERS FOR THE 1st GRAIN VERTICAL,
FOR THE 2nd HORIZ.

$M_{12} =$

	0	1	2	3	4	5	6	7	8	9
0	0.39	0.60	0.64	0.04	-0.14	0.31	0.28	0.03	-0.22	-0.20
1	-0.60	0.22	-0.42	-0.63	-0.52	-0.00	0.45	-0.45	0.22	0.00
2	0.04	0.63	0.35	-0.28	-0.38	0.26	0.46	-0.20	-0.09	-0.17
3	0.63	0.42	0.76	0.34	0.13	0.27	0.02	0.25	-0.30	-0.17
4	-0.22	-0.22	-0.30	-0.08	0.08	-0.00	-0.07	0.07	-1.00	0.01
5	-0.20	-0.00	-0.17	-0.17	-0.00	0.28	0.14	0.14	-0.01	-1.00
6	0.09	0.19	0.18	-0.01	-0.07	0.14	0.13	0.01	0.86	-0.50
7	-0.29	-0.19	-0.35	-0.16	0.07	0.14	0.01	0.13	-0.87	-0.49
8	-0.15	0.53	0.13	-0.39	-0.66	-0.01	0.56	-0.57	0.08	-0.00
9	0.32	0.01	0.28	0.27	-0.01	0.82	0.41	0.40	0.00	0.28
10	0.03	0.46	0.25	-0.20	-0.57	0.40	0.69	-0.30	0.07	0.14
11	0.28	-0.45	0.02	0.47	0.57	0.42	-0.29	0.70	-0.07	0.14
12	0.08	-0.43	-0.15	0.28	-0.14	-0.32	-0.04	-0.28	-0.23	0.21
13	0.44	-0.16	0.30	0.46	-0.53	-0.00	0.46	-0.46	0.23	0.00
14	0.15	0.30	0.28	-0.02	-0.14	0.28	0.26	0.02	0.32	-0.18
15	-0.28	0.46	-0.02	-0.47	0.39	0.28	-0.20	0.48	0.09	-0.19

Calculate the schmid factor for grain 1 (S_{F1x})

For (111) [11-2] with the tensile direction transformed to the lab y axis (010)

$$S_{F10} := [m_1(0)\cdot(Q_1\cdot T1)][d_1(0)\cdot(Q_1\cdot T1)]$$

For (-111) [-11-2] with the tensile direction transformed to the lab y axis (010)

$$S_{F14} := [m_1(4)\cdot(Q_1\cdot T1)][d_1(4)\cdot(Q_1\cdot T1)]$$

For (1-11) [11-2] with the tensile direction transformed to the lab y axis (010)

$$S_{F18} := [m_1(8)\cdot(Q_1\cdot T1)][d_1(8)\cdot(Q_1\cdot T1)]$$

For (-1-11) [1-1-2] with the tensile direction transformed to the lab y axis (010)

$$S_{F112} := [m_1(12)\cdot(Q_1\cdot T1)][d_1(12)\cdot(Q_1\cdot T1)]$$

Calculate the schmid factor for grain 2 (SF2x)

For (111) [11-2] with the tensile direction transformed to the lab y axis (010)

$$S_{F20} := [m_2(0)\cdot(Q_2\cdot T2)][d_2(0)\cdot(Q_2\cdot T2)]$$

For (-111) [-11-2] with the tensile direction transformed to the lab y axis (010)

$$S_{F24} := [m_2(4)\cdot(Q_2\cdot T2)][d_2(4)\cdot(Q_2\cdot T2)]$$

For (1-11) [11-2] with the tensile direction transformed to the lab y axis (010)

$$S_{F28} := [m_2(8)\cdot(Q_2\cdot T2)][d_2(8)\cdot(Q_2\cdot T2)]$$

For (-1-11) [1-1-2] with the tensile direction transformed to the lab y axis (010)

$$S_{F212} := [m_2(12)\cdot(Q_2\cdot T2)][d_2(12)\cdot(Q_2\cdot T2)]$$

Compute the twin vector dot with the tensile direction, denotes as B0,B4,B8,B12 (Absolute Value)

$$B_{10} := |(d_1(0))\cdot(Q_1\cdot T1)|$$
$$B_{14} := |(d_1(4))\cdot(Q_1\cdot T1)|$$
$$B_{18} := |(d_1(8))\cdot(Q_1\cdot T1)|$$
$$B_{112} := |(d_1(12))\cdot(Q_1\cdot T1)|$$

Compute the twin vector dot with the tensile direction, denotes as B0,B4,B8,B12 Absolute Values

$$B_{20} := |(d_2(0))\cdot(Q_2\cdot T2)|$$
$$B_{24} := |(d_2(4))\cdot(Q_2\cdot T2)|$$
$$B_{28} := |(d_2(8))\cdot(Q_2\cdot T2)|$$
$$B_{212} := |(d_2(12))\cdot(Q_2\cdot T2)|$$

Compute the sum of twin vector doted ordinary dislocations denoted as D0,D4,C8,D12 where the twin will interact with all the ordinary dislocations on the other side of the boundary Absolute values

$$D_{10} := \left|(d_1(0))\cdot(d_2(1))\right| + \left|(d_1(0))\cdot(d_2(5))\right| + \left|(d_1(0))\cdot(d_2(9))\right| + \left|(d_1(0))\cdot(d_2(13))\right|$$
$$D_{14} := \left|(d_1(4))\cdot(d_2(1))\right| + \left|(d_1(4))\cdot(d_2(5))\right| + \left|(d_1(4))\cdot(d_2(9))\right| + \left|(d_1(4))\cdot(d_2(13))\right|$$
$$D_{18} := \left|(d_1(8))\cdot(d_2(1))\right| + \left|(d_1(8))\cdot(d_2(5))\right| + \left|(d_1(8))\cdot(d_2(9))\right| + \left|(d_1(8))\cdot(d_2(13))\right|$$
$$D_{112} := \left|(d_1(12))\cdot(d_2(1))\right| + \left|(d_1(12))\cdot(d_2(5))\right| + \left|(d_1(12))\cdot(d_2(9))\right| + \left|(d_1(12))\cdot(d_2(13))\right|$$
$$D_{20} := \left|(d_2(0))\cdot(d_1(1))\right| + \left|(d_2(0))\cdot(d_1(5))\right| + \left|(d_2(0))\cdot(d_1(9))\right| + \left|(d_2(0))\cdot(d_1(13))\right|$$
$$D_{24} := \left|(d_2(4))\cdot(d_1(1))\right| + \left|(d_2(4))\cdot(d_1(5))\right| + \left|(d_2(4))\cdot(d_1(9))\right| + \left|(d_2(4))\cdot(d_1(13))\right|$$
$$D_{28} := \left|(d_2(8))\cdot(d_1(1))\right| + \left|(d_2(8))\cdot(d_1(5))\right| + \left|(d_2(8))\cdot(d_1(9))\right| + \left|(d_2(8))\cdot(d_1(13))\right|$$
$$D_{212} := \left|(d_2(12))\cdot(d_1(1))\right| + \left|(d_2(12))\cdot(d_1(5))\right| + \left|(d_2(12))\cdot(d_1(9))\right| + \left|(d_2(12))\cdot(d_1(13))\right|$$

Compute the sum of twin vector dot other twins from adjacent grain Actual Value

$$E_{Aos10} := d_1(0)\cdot d_2(0) + d_1(0)\cdot d_2(4) + d_1(0)\cdot d_2(8) + d_1(0)\cdot d_2(12)$$
$$E_{Aos14} := d_1(4)\cdot d_2(0) + d_1(4)\cdot d_2(4) + d_1(4)\cdot d_2(8) + d_1(4)\cdot d_2(12)$$
$$E_{Aos18} := d_1(8)\cdot d_2(0) + d_1(8)\cdot d_2(4) + d_1(8)\cdot d_2(8) + d_1(8)\cdot d_2(12)$$
$$E_{Aos112} := d_1(12)\cdot d_2(0) + d_1(12)\cdot d_2(4) + d_1(12)\cdot d_2(8) + d_1(12)\cdot d_2(12)$$
$$E_{Aos20} := d_2(0)\cdot d_1(0) + d_2(0)\cdot d_1(4) + d_2(0)\cdot d_1(8) + d_2(0)\cdot d_1(12)$$
$$E_{Aos24} := d_2(4)\cdot d_1(0) + d_2(4)\cdot d_1(4) + d_2(4)\cdot d_1(8) + d_2(4)\cdot d_1(12)$$
$$E_{Aos28} := d_2(8)\cdot d_1(0) + d_2(8)\cdot d_1(4) + d_2(8)\cdot d_1(8) + d_2(8)\cdot d_1(12)$$
$$E_{Aos212} := \left(d_2(12)\cdot d_1(0) + d_2(12)\cdot d_1(4) + d_2(12)\cdot d_1(8) + d_2(12)\cdot d_1(12)\right)$$

Using Actual Values for twin vector dotted with twin vectors on the other grain.
This subprogram will replace the negative values will be replaced with ZERO as it has not significant meaning.

$$E_{1020} := \left(d_1(0)\right)\cdot\left(d_2(0)\right)$$
$$E_{1024} := \left(d_1(0)\right)\cdot\left(d_2(4)\right)$$
$$E_{1028} := \left(d_1(0)\right)\cdot\left(d_2(8)\right)$$
$$E_{10212} := \left(d_1(0)\right)\cdot\left(d_2(12)\right)$$

$$E_{A0B0} := \text{if}\left(E_{1020} < 0, 0, E_{1020}\right)$$
$$E_{A0B4} := \text{if}\left(E_{1024} < 0, 0, E_{1024}\right)$$
$$E_{A0B8} := \text{if}\left(E_{1028} < 0, 0, E_{1028}\right)$$
$$E_{A0B12} := \text{if}\left(E_{10212} < 0, 0, E_{10212}\right)$$

$$E_{1420} := \left(d_1(4)\right)\cdot\left(d_2(0)\right)$$
$$E_{1424} := \left(d_1(4)\right)\cdot\left(d_2(4)\right)$$
$$E_{1428} := \left(d_1(4)\right)\cdot\left(d_2(8)\right)$$
$$E_{14212} := \left(d_1(4)\right)\cdot\left(d_2(12)\right)$$

$$E_{A4B0} := \text{if}\left(E_{1420} < 0, 0, E_{1420}\right)$$
$$E_{A4B4} := \text{if}\left(E_{1424} < 0, 0, E_{1424}\right)$$
$$E_{A4B8} := \text{if}\left(E_{1428} < 0, 0, E_{1428}\right)$$
$$E_{A4B12} := \text{if}\left(E_{10212} < 0, 0, E_{14212}\right)$$

$$E_{1820} := \left(d_1(8)\right)\cdot\left(d_2(0)\right)$$
$$E_{1824} := \left(d_1(8)\right)\cdot\left(d_2(4)\right)$$
$$E_{1828} := \left(d_1(8)\right)\cdot\left(d_2(8)\right)$$
$$E_{18212} := \left(d_1(8)\right)\cdot\left(d_2(12)\right)$$

$$E_{A8B0} := \text{if}\left(E_{1820} < 0, 0, E_{1820}\right)$$
$$E_{A8B4} := \text{if}\left(E_{1824} < 0, 0, E_{1824}\right)$$
$$E_{A8B8} := \text{if}\left(E_{1828} < 0, 0, E_{1828}\right)$$
$$E_{A8B12} := \text{if}\left(E_{18212} < 0, 0, E_{18212}\right)$$

$$E_{11220} := \left(d_1(12)\right)\cdot\left(d_2(0)\right)$$
$$E_{11224} := \left(d_1(12)\right)\cdot\left(d_2(4)\right)$$
$$E_{11228} := \left(d_1(12)\right)\cdot\left(d_2(8)\right)$$
$$E_{112212} := \left(d_1(12)\right)\cdot\left(d_2(12)\right)$$

$$E_{A12B12} := \text{if}\left(E_{112212} < 0, 0, E_{112212}\right)$$
$$E_{A12B0} := \text{if}\left(E_{11220} < 0, 0, E_{11220}\right)$$
$$E_{A12B4} := \text{if}\left(E_{11224} < 0, 0, E_{11224}\right)$$
$$E_{A12B8} := \text{if}\left(E_{11228} < 0, 0, E_{1828}\right)$$

$$E_{2010} := \left(d_2(0)\right)\cdot\left(d_1(0)\right)$$
$$E_{2014} := \left(d_2(0)\right)\cdot\left(d_1(4)\right)$$
$$E_{2018} := \left(d_2(0)\right)\cdot\left(d_1(8)\right)$$
$$E_{20112} := \left(d_2(0)\right)\cdot\left(d_1(12)\right)$$

$$E_{B0A12} := \text{if}\left(E_{20112} < 0, 0, E_{20112}\right)$$
$$E_{B0A0} := \text{if}\left(E_{2010} < 0, 0, E_{2010}\right)$$
$$E_{B0A4} := \text{if}\left(E_{2014} < 0, 0, E_{2014}\right)$$
$$E_{B0A8} := \text{if}\left(E_{2018} < 0, 0, E_{2018}\right)$$

$$E_{2410} := \left(d_2(4)\right)\cdot\left(d_1(0)\right)$$
$$E_{2414} := \left(d_2(4)\right)\cdot\left(d_1(4)\right)$$
$$E_{2418} := \left(d_2(4)\right)\cdot\left(d_1(8)\right)$$
$$E_{24112} := \left(d_2(4)\right)\cdot\left(d_1(12)\right)$$

$E_{B4A12} := \text{if}(E_{24112} < 0, 0, E_{24112})$
$E_{B4A0} := \text{if}(E_{2410} < 0, 0, E_{2410})$
$E_{B4A4} := \text{if}(E_{2414} < 0, 0, E_{2414})$
$E_{B4A8} := \text{if}(E_{2418} < 0, 0, E_{2418})$

$E_{2810} := (d_2(8)) \cdot (d_1(0))$
$E_{2814} := (d_2(8)) \cdot (d_1(4))$
$E_{2818} := (d_2(8)) \cdot (d_1(8))$
$E_{28112} := (d_2(8)) \cdot (d_1(12))$

$E_{B8A12} := \text{if}(E_{28112} < 0, 0, E_{28112})$
$E_{B8A0} := \text{if}(E_{2810} < 0, 0, E_{2810})$
$E_{B8A4} := \text{if}(E_{2814} < 0, 0, E_{2814})$
$E_{B8A8} := \text{if}(E_{2818} < 0, 0, E_{2818})$

$E_{21210} := (d_2(12)) \cdot (d_1(0))$
$E_{21214} := (d_2(12)) \cdot (d_1(4))$
$E_{21218} := (d_2(12)) \cdot (d_1(8))$
$E_{212112} := (d_2(12)) \cdot (d_1(12))$

$E_{B12A12} := \text{if}(E_{212112} < 0, 0, E_{212112})$
$E_{B12A0} := \text{if}(E_{21210} < 0, 0, E_{21210})$
$E_{B12A4} := \text{if}(E_{21214} < 0, 0, E_{21214})$
$E_{B12A8} := \text{if}(E_{21218} < 0, 0, E_{21218})$

Summing the leading vector dotted with the other vectors in the other grain
$E_{A0} := E_{A0B0} + E_{A0B4} + E_{A0B8} + E_{A0B12}$
$E_{B0} := E_{B0A0} + E_{B0A4} + E_{B0A8} + E_{B0A12}$

$E_{A4} := E_{A4B0} + E_{A4B4} + E_{A4B8} + E_{A4B12}$
$E_{B4} := E_{B4A0} + E_{B4A4} + E_{B4A8} + E_{B4A12}$

$E_{A8} := E_{A8B0} + E_{A8B4} + E_{A8B8} + E_{A8B12}$
$E_{B8} := E_{B8A0} + E_{B8A4} + E_{B8A8} + E_{B8A12}$

$E_{A12} := E_{A12B0} + E_{A12B4} + E_{A12B8} + E_{A12B12}$
$E_{B12} := E_{B12A0} + E_{B12A4} + E_{B12A8} + E_{B12A12}$

Compute the Factor formulated by Benjamin Simkin

$Ben_{10} := S_{F10} \cdot B_{10} \cdot C_{10}$
$Ben_{14} := S_{F14} \cdot B_{14} \cdot C_{14}$
$Ben_{18} := S_{F18} \cdot B_{18} \cdot C_{18}$
$Ben_{112} := S_{F112} \cdot B_{112} \cdot C_{112}$

$Ben_{20} := S_{F20} \cdot B_{20} \cdot C_{20}$
$Ben_{24} := S_{F24} \cdot B_{24} \cdot C_{24}$
$Ben_{28} := S_{F28} \cdot B_{28} \cdot C_{28}$
$Ben_{212} := S_{F212} \cdot B_{212} \cdot C_{212}$

Compute Steve Factor Z which is a product of SF, B, D E

$F_{A0} := S_{F10} \cdot B_{10} \cdot D_{10} \cdot E_{A0}$
$F_{A4} := S_{F14} \cdot B_{14} \cdot D_{14} \cdot E_{A4}$
$F_{A8} := S_{F18} \cdot B_{18} \cdot D_{18} \cdot E_{A8}$
$F_{A12} := S_{F112} \cdot B_{112} \cdot D_{112} \cdot E_{A12}$
$F_{B0} := S_{F20} \cdot B_{20} \cdot D_{20} \cdot E_{B0}$
$F_{B4} := S_{F24} \cdot B_{24} \cdot D_{24} \cdot E_{B4}$
$F_{B8} := S_{F28} \cdot B_{28} \cdot D_{28} \cdot E_{B8}$
$F_{B12} := S_{F212} \cdot B_{212} \cdot D_{212} \cdot E_{B12}$

$$Z := \begin{pmatrix} S_{F10} & B_{10} & D_{10} & E_{A0} & Ben_{10} & F_{A0} \\ S_{F14} & B_{14} & D_{14} & E_{A4} & Ben_{14} & F_{A4} \\ S_{F18} & B_{18} & D_{18} & E_{A8} & Ben_{18} & F_{A8} \\ S_{F112} & B_{112} & D_{112} & E_{A12} & Ben_{112} & F_{A12} \\ S_{F20} & B_{20} & D_{20} & E_{B0} & Ben_{20} & F_{B0} \\ S_{F24} & B_{24} & D_{24} & E_{B4} & Ben_{24} & F_{B4} \\ S_{F28} & B_{28} & D_{28} & E_{B8} & Ben_{28} & F_{B8} \\ S_{F212} & B_{212} & D_{212} & E_{B12} & Ben_{212} & F_{B12} \end{pmatrix}$$

$$\mathbf{Z} = \begin{pmatrix} -0.16 & 0.48 & 2.71 & 1.15 & -0.30 & -0.24 \\ -0.01 & 0.01 & 1.27 & 1.92 & -0.00 & -0.00 \\ 0.30 & 0.94 & 1.92 & 0.28 & 0.88 & 0.16 \\ -0.16 & 0.47 & 2.72 & 0.80 & -0.30 & -0.17 \\ -0.18 & 0.51 & 2.72 & 1.15 & -0.35 & -0.28 \\ 0.27 & 0.95 & 1.92 & 0.28 & 0.79 & 0.14 \\ -0.05 & 0.05 & 1.27 & 2.56 & -0.01 & -0.01 \\ -0.18 & 0.50 & 2.71 & 1.17 & -0.35 & -0.29 \end{pmatrix}$$

Program #2

```
Stereographic Projection Plot
Run via Mathematica

<<Graphics`ParametricPlot3D`
(*uses normal and tilt axis*)
(* Initial Definitions *)

a=1 ;    b=1;    c=1.;

mag[v_]:=Sqrt[(a v[[1]])^2 +(b v[[2]])^2 +(c v[[3]])^2];

unit[v_]:={a v[[1]],b v[[2]],c v[[3]]}/mag[v];

unit2[v_]:={v[[1]],v[[2]]}/Sqrt[v[[1]]^2+v[[2]]^2];

Proj[n_,v_]:=v-(v.n)n;

(* Input appropriate crystal information *)

(* Define reference planes for projection *)

M={{1,0,0},{0,1,0},{0,0,1},{1,1,0},{1,-1,0},{1,0,1},{-
1,0,1},{0,1,1},{0,
        1,-1}};

m=Map[unit,M];

(* Define surface normal/in-plane orthogonal directions *)

(* Define matrix of all grain sample normals *)

GSN:={{30,42,11},{26,39,17},{3,4,1}};

(* Define matrix of all tensile directions *)

GTA:={{11,-10,8},{-32,27,7},{19,-18,15}};

(* Define matrix of all corresponding rotation axes *)

GRA:={Cross[GTA[[1]],GSN[[1]]],Cross[GTA[[2]],GSN[[2]]],
      Cross[GTA[[3]],GSN[[3]]]};

snxloc={1,0,0}; snyloc={0,1,0}; snloc={0,0,1};

(* Function to rotate a vector v about axis n by an angle theat,
  measured to be postive around n *)

ROTATE[n_,theta_,v_]:=
    v + Sin[theta] Cross[n,v] + (1-Cos[theta]) (n (n.v) - v);

(* Great circle function wrt local coordinate system *)

v[phi_]:={Cos[phi],0,Sin[phi]};
```

```
(* Function to calculate components of v (written with respect to
crystal \
basis) with respect to the local coordinate system *)

CONVERT[v_]:=unit[{snx.v,sny.v,sn.v}];

PROJECT[v_]:=(2/(1-v[[3]])) {v[[1]],v[[2]]};


(* Denote normal/rotation axis for calculation *)

 (* SN = GSN[[3]]; sn = unit[SN]; *)

   SN = {11,3,-12};  sn = unit[SN];

(*  R = GRA[[3]];  snx = unit[R]; *)

R= {6,-10,3};   snx = unit[R];


 SNY=Cross[SN,R];   sny=unit[SNY];


Pcircle =
    ParametricPlot[{2 Cos[t],2 Sin[t]},{t,0,2 Pi},AspectRatio \[Rule]
1,
      DisplayFunction \[Rule] Identity, PlotRange \[Rule] {{-2,2},{-
2,2}},
      PlotStyle \[Rule] {{GrayLevel[0.5], Thickness[0.01]}}];

NewPlot = Pcircle;

Do[

    (* Decision Tree For {100} Family Of Planes *)

      If[i\[LessEqual] 3, hueswitch = 1, hueswitch = 0];

            OldPlot = NewPlot;

      If[hueswitch \[Equal] 1,

                  huesetting = (i-1)/3;

               (*
        Ensure that normal to crystal plane is directed into same \
half   space as sample normal *)

            If[m[[i]].sn >=  0, mnorm=m[[i]], mnorm=-m[[i]]];

              (* Transform crystal plane normal mnorm into planenorm,
       written with respect to the tn (tensile-
             sample normal) coordinate system *)

              planenorm =CONVERT[mnorm];

              (*
```

```
        Check to see if crystal plane is the same as the sample normal
*)

            If[sn.mnorm \[Equal] 1, CurrentPlot = Pcircle ,

                                (*
          Calculate line of intersection between crystal plane and
                        sample surface in t-s local coordinate system *)

                                 axis1 = CONVERT[Cross[sn,mnorm]];

                                (*
          Determine correct angle to rotate snxloc about sn so that
                        it properly aligns with the axis1 *)


        If[axis1.snyloc \[GreaterEqual] 0, delta=ArcCos[axis1.snxloc],

\
                             delta=-ArcCos[axis1.snxloc]];

                                (*
          Calculate acute angle between crystal plane normal and

            sample   normal.
              This is the angle through which circular path,
                    after the first rotation,
          is rotated about axis1 to its final state. *)

                             psi = Pi/2-ArcCos[sn.mnorm];

                            (* Print[ToString[psi]]; *)

                                (*
          Calculate path of intersection of crystal plane with unit
                                 sphere with respect to t-
            s local coordinate system *)


        vt[phi_]:=ROTATE[axis1,psi,ROTATE[snloc,delta,v[phi]]];


                                (*
          Check whether crystal plane is parallel to sample normal.
              If it is,

          then the projection is just the line of intersection between

            the crystal plane and the sample surface.  If it is not,
                        then we simply proceed with the algorithm *)


                                 If[sn.mnorm\[Equal]0,

                                (* Check if axis1[[2]]=0.  If so,
                       then the intersection is vertical.  If not,
            then proceed as usual. *)
```

```
If[axis1[[2]]\[Equal]0,


              CurrentPlot =
                  ParametricPlot[{0,t},{t,-2,2},AspectRatio \[Rule] 1,

                    DisplayFunction \[Rule] Identity,
                    PlotRange \[Rule] {{-2,2},{-2,2}},

                    PlotStyle \[Rule] {{Hue[huesetting],
                          Dashing[{0.02,0.02}]}}];

                                                  ,


              upperlimit = 2/Sqrt[1+(axis1[[2]]/axis1[[1]])^2];

              lowerlimit = -2/Sqrt[1+(axis1[[2]]/axis1[[1]])^2];

              CurrentPlot =
                ParametricPlot[{t,(axis1[[2]]/axis1[[1]])
t},{t,lowerlimit,
                    upperlimit},AspectRatio \[Rule] 1,
                  DisplayFunction \[Rule] Identity,
                  PlotRange \[Rule] {{-2,2},{-2,2}},

                  PlotStyle \[Rule] {{Hue[huesetting],
                        Dashing[{0.05,0.05}]}}];

                                    ];

                          ,


                          (*
            Calculate projection of 3-
              dimensional path into sample surface *)

                          rt[phi_]:=(2/(1-vt[phi][[3]]))
{vt[phi][[1]],vt[phi][[2]]};

                          (* Generate plot of projection *)



          CurrentPlot =
            ParametricPlot[{rt[phi][[1]],rt[phi][[2]]},{phi,Pi, 2 Pi},
              AspectRatio \[Rule] 1, DisplayFunction \[Rule] Identity,
              PlotRange \[Rule] {{-2,2},{-2,2}},
              PlotStyle \[Rule]
{{Hue[huesetting],Dashing[{0.02,0.02}]}}];

                  ];

        ];
```

```
      ,

      (* Remainder Of Procedure Handles Non {100} family planes *)

      huesetting = (i-4)/6;

       (*
        Ensure that normal to crystal plane is directed into same half
space \
as sample normal *)

      If[m[[i]].sn \[GreaterEqual]  0, mnorm=m[[i]], mnorm=-m[[i]]];

      (* Transform crystal plane normal into tn (tensile-
            sample normal) coordinate system *)

      planenorm = unit[{mnorm.snx,mnorm.sny,mnorm.sn}];


      (* Check to see if crystal plane is the same as the sample normal
*)

      If[sn.mnorm \[Equal] 1, CurrentPlot = Pcircle ,

         (*
          Calculate line of intersection between crystal plane and
sample \
surface in t-s local coordinate system *)

        axis1 = unit[Cross[snloc,planenorm]];

        (*
          Determine correct angle to rotate snxloc about snloc so that
it \
properly aligns with the axis1 *)

        If[axis1.snyloc \[GreaterEqual] 0, delta=ArcCos[axis1.snxloc],
          delta=-ArcCos[axis1.snxloc]];

        (*
          Calculate acute angle between crystal plane normal and sample
\
normal.  This is the angle through which circular path,
          after the first rotation,
          is rotated about snloc x planenorm to its final state. *)

        psi = Pi/2-ArcCos[snloc.planenorm];

        (* Print[ToString[psi]]; *)

        (*
          Calculate path of intersection of crystal plane with unit
sphere \
with respect to t-s local coordinate system *)

        vta[phi_]:=ROTATE[snloc,delta,v[phi]];
```

```
        vtb[phi_]:=ROTATE[axis1,psi,vta[phi]];


        (* Check whether crystal plane is parallel to sample normal.
             If it is,
          then the projection is just the line of intersection between
the \
crystal plane and the sample surface.  If it is not,
          then we simply proceed with the algorithm *)


        If[sn.mnorm\[Equal]0,

          (* Check if axis1[[2]]=0.  If so,
            then the intersection is vertical.  If not,
            then proceed as usual. *)

          If[axis1[[2]]\[Equal]0,


              CurrentPlot =
                  ParametricPlot[{0,t},{t,-2,2},AspectRatio \[Rule] 1,
                    DisplayFunction \[Rule] Identity,
                    PlotRange \[Rule] {{-2,2},{-2,2}},
                    PlotStyle\[Rule]{Hue[huesetting]}];

              ,


              upperlimit = 2/Sqrt[1+(axis1[[2]]/axis1[[1]])^2];

              lowerlimit = -2/Sqrt[1+(axis1[[2]]/axis1[[1]])^2];


              CurrentPlot =
                ParametricPlot[{t,(axis1[[2]]/axis1[[1]])
t},{t,lowerlimit,
                    upperlimit},AspectRatio \[Rule] 1,
                  DisplayFunction \[Rule] Identity,
                  PlotRange \[Rule] {{-2,2},{-2,2}},
                  PlotStyle\[Rule]{Hue[huesetting]}];

              ];

          ,


          (*
            Calculate projection of 3-
              dimensional path into sample surface *)

          rt[phi_]:=(2/(1-vtb[phi][[3]]))
{vtb[phi][[1]],vtb[phi][[2]]};

          (* Generate plot of projection *)
```

```
          CurrentPlot =
            ParametricPlot[{rt[phi][[1]],rt[phi][[2]]},{phi,Pi, 2 Pi},
              AspectRatio \[Rule] 1, DisplayFunction \[Rule] Identity,
              PlotRange \[Rule] {{-2,2},{-2,2}},
              PlotStyle\[Rule]{Hue[huesetting]}];

          ];

        ];
      ];
    NewPlot = Show[OldPlot, CurrentPlot];

    ,{i,1,9}];

PROJ = Show[NewPlot, DisplayFunction \[Rule] $DisplayFunction,
    Axes\[Rule] False]

Print["Surface Normal = "<>ToString[SN]];
Print["Rotation Axis = "<>ToString[R]];

(* Color Key: Red (dashed) = (100), Green (dashed) = (010),
  Blue (dashed) = (001), Red = (110), Yellow = (1-10), Green = (101),
  Cyan = (-101), Blue = (011), magenta = (01-1) *)
% Start of Graphics




% End of Graphics
MathPictureEnd
\
\>"]
\[SkeletonIndicator]Graphics\[SkeletonIndicator]
Surface Normal = {11, 3, -12}
Rotation Axis = {6, -10, 3}

vec1:={0,1,0};        vec2:={0,1,1};

angle[a_,b_]:=ArcCos[unit[a].unit[b]];

angle[vec1,vec2]
0.785398
```

Program#3

```
111 trace projection
Run via Mathematica

<<Graphics`ParametricPlot3D`

<<Graphics`Graphics`

(* Initial Definitions *)

a=1 ;    b=1;    c=1.;

mag[v_]:=Sqrt[(a v[[1]])^2 +(b v[[2]])^2 +(c v[[3]])^2];

unit[v_]:={a v[[1]],b v[[2]],c v[[3]]}/mag[v];


(* Define reference planes for projection *)

(*                        ------------------------------------- INPUT
-----------
          PLANES *)

M:={{1,1,1},{-1,1,1},{1,-1,1},{1,1,-1}};

UM:=Map[unit,M];

SIZE = Length[UM];

(* Define Normal/Tensile Directions WRT Crystal Basis *)

(*                        ------------------------------------- INPUT
-----------
            SURFACE NORMALS *)

NORMSET:={{30,42,11},{26,39,17},{3,4,1}};

UN:=Map[unit,NORMSET];

(*                        ------------------------------------- INPUT
-----------
            TENSILE DIRECTIONS *)

TENSSET:={{283,-254,198},{-592,355,91},{19,-18,15}};

UT:=Map[unit,TENSSET];


(* Select Normal Vector / Tensile Direction Pair For Calculation *)

(*                        ------------------------------------- INPUT
-----------
            GRAIN OF INTEREST *)

GN:=1;
```

```
(* Define Tilt Angle *)

(*                        ---------------------------------------- INPUT
-----------
            SAMPLE TILT *)


phi=  0 Degree;


NORM:=UN[[GN]];        TENS:= UT[[GN]]; LROT:=Cross[TENS,NORM];

(* Calculate Direction Vectors For Zero Degree Tilt Plane Traces *)

OLDLINES = {};

Do[

    DIRECTION = Cross[NORM,UM[[i]]];

    LINES = Append[OLDLINES,DIRECTION];

    OLDLINES = LINES;
    ,

    {i,1,SIZE}];


LU:=Map[unit,LINES];


(* Do Routine To Generate Matrix Of Directions Of Trace Lines On
Projected \
Plane *)


PLOTNEW = {};

anglelist = {};

Do[

    PLOTOLD = PLOTNEW;

    (* Calculate Trace Of Each Intersection of a {111} plane w/ surface
*)

    TRACE =
      LU[[i]] - (Cos[phi] Sin[
                phi] (Cross[NORM,ROT].LU[[i]]) NORM) - (Sin[phi])^2
(Cross[NORM,
                  ROT].LU[[i]]) Cross[NORM,ROT];

    TRACENORM = unit[TRACE];

       (* Calculate trace of tensile axis *)
```

```
    TENTRACE =
      TENS - (Cos[phi] Sin[
               phi] (Cross[NORM,ROT].TENS) NORM) - (Sin[phi])^2
(Cross[NORM,
                 ROT].TENS) Cross[NORM,ROT];

    (* Calculate cos^-1 of dot product between positive rotation axis
and \
line direction L[[i]] *)

    theta = ArcCos[ROT.TRACENORM];

    (* Check to see if line direction TRACENORM is in quadrants 1-2 or
\
quadrants 3-4;
      A value > 0 indicates that TRACENORM is in upper two quadrants
**)

    checkvalue = TRACENORM.TENTRACE;

    If[checkvalue \[GreaterEqual] 0,

            direction = {Cos[theta],Sin[theta]};

      ,

               direction = {-Cos[theta],Sin[theta]};

      ];

    slope = direction[[2]]/direction[[1]];

    newangle = ArcTan[direction[[2]]/direction[[1]]]/Degree;

    If[newangle<0, angle = newangle + Pi/Degree, angle = newangle];

    newanglelist = Append[anglelist,angle];

    anglelist = newanglelist;

    P[x_]:=slope x;

    lwrlimit = -1/Sqrt[1+slope^2];

    uprlimit = 1/Sqrt[1+slope^2];

    PLT=Plot[P[x],{x,lwrlimit,uprlimit},DisplayFunction \[Rule]
Identity,
        PlotStyle\[Rule]{GrayLevel[(i-1)/SIZE], Thickness[0.01]}];

    PLOTNEW = Append[PLOTOLD,PLT];

    ,{i,1,SIZE}];

Show[PLOTNEW,DisplayFunction\[Rule]$DisplayFunction,AspectRatio \[Rule]
1,
```

```
    PlotRange\[Rule]{-1,1}];

Print[TableForm[anglelist]];

(* Order of shading is also order of crystallographic planes in the
matrix \
"M" above,
  evolving from darker shading to lighter shading.
      The angles listed below are given in the same order,
  and indicate the angle that the line makes w/ the positive x-axis,
  measured counterclockwise from that axis.  Therefore,
  they are given as numbers between zero and Pi. *)


GraphicsData["PostScript", "\<\



% End of Graphics
MathPictureEnd
\
\>"]
\!\(\*
  InterpretationBox[GridBox[{
        {"136.8674086569651`"},
        {"61.85578208388911`"},
        {"171.8296228125404`"},
        {"107.79361094154851`"}
        },
      RowSpacings->1,
      ColumnSpacings->3,
      RowAlignments->Baseline,
      ColumnAlignments->{Left}],
    TableForm[ {136.8674086569651, 61.85578208388911,
171.82962281254041,
      107.79361094154851}]]\)
```

Appendix 4
Using other variables in the Fracture Propagation Parameter

Fracture Propagation Parameter:

$$F_{A\leftrightarrow B} = m_{Atw}\left|\hat{b}_{Atw}\bullet\hat{t}\right|\left[\sum_{Bord=1}^{2}\left|\hat{b}_{Atw}\bullet\hat{b}_{Bord}\right| + \sum_{Btw=1}^{4}\hat{b}_{Atw}\bullet\hat{b}_{Btw}\Big|_{if>0}\right]$$

1. When the second sum is such that only the absolute values are used:

$$\sum_{Btw=1}^{4}\hat{b}_{Atw}\bullet\hat{b}_{Btw}\Big|$$

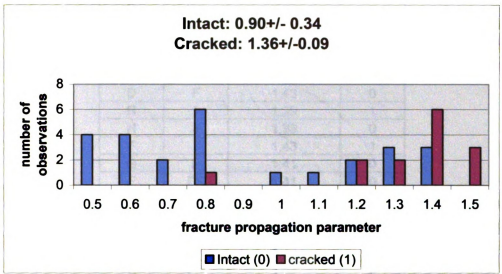

Figure A4-1. Histogram showing intact and cracked boundaries using $F_{A\text{-}B}$ values computed using absolute values for the interaction between two twinning vectors.

Table A4-1: t-test for population means using the absolute values for the interaction between two twinning vectors

t-Test: Two-Sample		
	Intact	Cracked
Mean	0.90	1.36
Standard deviation	0.34	0.09
Variance	0.11	0.01
Observations	25	13
Pooled Variance	0.08	
Hypothesized Mean Difference	0	
df	36	
t Stat	-4.858	
P(T<=t) one-tail	1.18E-05	
t Critical one-tail	2.71	
P(T<=t) two-tail	2.36E-05	
t Critical two-tail	2.99	

Table A4.2: Selected F_{A-B} values
(Using absolute values for the computation between twinning vectors)

Absolute Values		Selected	0=intact
Grain1	Grain2	FA-B value	1=crack
A	BB	0.55	0
B	C	0.84	0
BB	B	0.84	1
BB	BE	0.5	0
BE	E	1.22	0
D	E	0.61	0
C	E	0.61	0
C	D	0.51	0
D	I	1.27	1
D	H	1.278	0
D	F	1.43	0
H	I	1.39	1
H	J	1.33	0
F	I	1.43	1
G	F	1.41	0
F	FK	1.41	0
I	FK	1.47	1
HJ	FK	1.2	1
FK	K	1.24	0
FK	J	1.49	1
H	HJ	1.43	0
K	J	1.35	1
HJ	J	1.31	0
K	LA	0.712	0
J	LA	1.4	1
J	L	1.13	0
K	L	0.77	0
L	LA	1.04	0
ZW	Z	0.51	0
5	Z	0.75	0
5	5A	1.24	1
5	5B	0.75	0
ZW	6	0.47	0
5	1	1.45	1
5A	1	1.37	1
5	2	0.75	0
Z	6	0.6	0
1	2	1.29	1
1	4	1.44	1
2	4	0.81	0
2	6	0.67	0

2. When the second sum is such that only the negatives values were used and the positive values were set to zero:

$$\sum_{Btw=1}^{4} \hat{b}_{Atw} \bullet \hat{b}_{Btw} \Big|_{if<0}$$

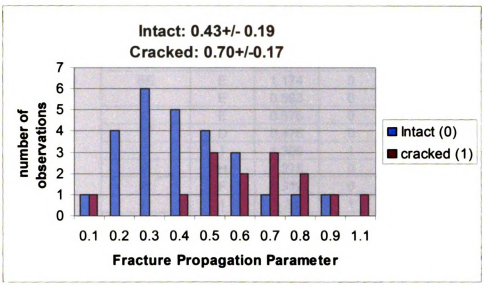

Figure A4-2. Histogram showing intact and cracked boundaries using $F_{A\text{-}B}$ values computed using "positive values set = zero" for the interaction between two twinning vectors.

Table A4-3: t-test for population means using the "positive values set = zero" values for the interaction between two twinning vectors

t-Test: Two-Sample		
	Intact	*Cracked*
Mean	0.43	0.70
Standard deviation	0.19	0.17
Variance	0.035	0.029
Observations	25	12
Pooled Variance	0.03	
Hypothesized Mean Difference	0	
df	35	
t Stat	-4.22	
P(T<=t) one-tail	8.09E-05	
t Critical one-tail	2.72	
P(T<=t) two-tail	0.00016	
t Critical two-tail	2.99	

Table A4:4: Selected F_{A-B} values (where any "positive values were set to zero values" for the computation between twinning vectors)

Positive=Zero Values		Selected	0=intact
Grain1	Grain2	FA-B value	1=crack
A	BB	0.407	0
B	C	0.755	0
BB	B	0.841	1
BB	BE	0.464	0
BE	E	1.174	0
D	E	0.593	0
C	E	0.576	0
C	D	0.476	0
D	I	1.309	1
D	H	1.278	0
D	F	0.312	0
H	I	1.31	1
H	J	1.26	0
F	I	1.43	1
G	F	1.09	0
F	FK	0.983	0
I	FK	1.28	1
HJ	FK	1.399	1
FK	K	0.986	0
FK	J	1.08	1
H	HJ	1.066	0
K	J	1.311	1
HJ	J	1.084	0
K	LA	0.712	0
J	LA	1.153	1
J	L	1.09	0
K	L	0.709	0
L	LA	0.699	0
ZW	Z	0.468	0
5	Z	0.72	0
5	5A	1.19	1
5	5B	0.44	0
ZW	6	0.47	0
5	1	0.87	1
5A	1	1.13	1
5	2	0.54	0
Z	6	0.32	0
1	2	1.491	1
1	4	1.38	1
2	4	1.07	0
2	6	1.45	0